UNIVERSIDADE FEDERAL DE PERNAMBUCO
CENTRO DE CIÊNCIAS EXATAS E DA NATUREZA
PROGRAMA DE PÓS-GRADUAÇÃO EM FÍSICA

ALLISON RODRIGO PESSOA DA SILVA

SPATIAL, SPECTRAL, AND TIME-RESOLVED CHARACTERIZATION OF SINGLE UPCONVERTING PARTICLES FOR MICRO- AND NANOTHERMOMETRY

Recife

2022

ALLISON RODRIGO PESSOA DA SILVA

SPATIAL, SPECTRAL, AND TIME-RESOLVED CHARACTERIZATION OF SINGLE UPCONVERTING PARTICLES FOR MICRO- AND NANOTHERMOMETRY

Dissertação apresentada ao Programa de Pós-Graduação em Física da Universidade Federal de Pernambuco, como requisito parcial para obtenção do título de mestre em Física. Área de concentração: Óptica.

Orientador (a): Anderson Monteiro Amaral

Recife

2022

Catalogação na fonte
Bibliotecária Monick Raquel Silvestre da S. Portes, CRB4-1217

S586s Silva, Allison Rodrigo Pessoa da
Spatial, spectral, and time-resolved characterization of single upconverting particles for micro- and nanothermometry / Allison Rodrigo Pessoa da Silva. – 2022.
97 f.: il., fig., tab.

Orientador: Anderson Monteiro Amaral.
Dissertação (Mestrado) – Universidade Federal de Pernambuco. CCEN, Física, Recife, 2022.

Inclui referências e apêndice.

1. Óptica. 2. Íons lantanídeos. I. Amaral, Anderson Monteiro (orientador). II. Título.

535.2 CDD (23. ed.) UFPE - CCEN 2022-136

ALLISON RODRIGO PESSOA DA SILVA

SPATIAL, SPECTRAL, AND TIME-RESOLVED CHARACTERIZATION OF SINGLE UPCONVERTING PARTICLES FOR MICRO- AND NANOTHERMOMETRY

Dissertação apresentada ao Programa de Pós-Graduação em Física da Universidade Federal de Pernambuco, como requisito parcial para a obtenção do título de Mestre em Física.

Aprovada em: 18/08/2022.

BANCA EXAMINADORA

_____

Prof. Anderson Monteiro Amaral
Orientador
Universidade Federal de Pernambuco

_____

Prof. Michael Cabrera Baez
Examinador Interno
Universidade Federal de Pernambuco

_____

Prof. Marcio André Rodrigues Cavalcanti de Alencar
Examinador Externo
Universidade Federal de Sergipe

AGRADECIMENTOS

Agradeço especialmente a minha mãe, Clécia, que é a pessoa mais guerreira do mundo. Ao meu pai, Edson, que sempre me incentivou a continuar. Também agradeço especialmente a minha esposa, Bianca, por todo apoio, carinho, e paciência. Também aos meus irmãos, que os amo muito.

Gostaria de agradecer enormemente aos meus orientadores, prof. Anderson Amaral e prof. Leonardo de S. Menezes, por todos os ensinamentos durante esses anos. Fiz o que pude para extrair o máximo dos seus estilos magistrais. Dentro do Departamento de Física fiz muitos amigos. Agradeço ao Edwin e ao Igor por terem me acompanhado desde muito cedo no Laboratório, e me ensinado sempre com paciência. Em especial ao Jefferson, com que compartilhei incalculáveis horas de muito trabalho e risadas no Lab. Habakuk, Alex, e Higo: muito obrigado pelas irreverentes discussões sobre Física e pelo companheirismo durante as disciplinas.

Agradecimento especial ao professor Sidney Ribeiro, e seu estudante York Serge-Correales, do Instituto de Química da UNESP Araraquara-SP, pela síntese das amostras usadas neste trabalho e pelas colaborações. Este trabalho não seria possível sem suporte técnico prestado pelo Departamento de Física. Agradeço ao Daniel (Oficina Eletrônica), Virgínia (Laboratório de Química), Elverson e Sérgio (Laboratório de Microscopia), Sr. João e Sr. Valdomiro (Oficina Mecânica). Por fim, à professora Ana Paula Paim, do Departamento de Química Fundamental, e sua orientanda Abinoan Rodrigues, por gentilmente cederem o uso do ultrassonicador de ponteira.

Fora do ambiente da UFPE, alguns também foram essenciais para minha formação, tanto como pesquisador, quanto como pessoa. Allan, meu compadre, que é um verdadeiro Renascentista. André, meu amigão, que também parece uma enciclopédia, principalmente musical. Por fim, registro aqui meus gradecimentos a familiares a amigos que foram essenciais para a conclusão deste trabalho, diretamente ou indiretamente, mas que não estão aqui citados simplesmente por uma questão de convenção.

ABSTRACT

The scientific community is increasingly looking deeper at phenomena in the micro and nanoscale. The miniaturization of electronic circuitry, biological and medical tools, and communication devices demands investigations at this level. Particularly, sensing temperature at submicron scales is crucial to analyzing numerous physical-chemical processes. To this end, lanthanoid ions doped in solid-state matrices are of special interest because of their unique optical properties. However, to indeed achieve high spatial resolutions, the single-particle measurement level must be employed, which brings many physical and instrumental artifacts that can disturb the thermal response of such systems. This work aims to characterize experimentally and theoretically single particles of $NaYF_4$: Yb^{3+}/Er^{3+} as thermometers and also to investigate the role of physical and instrumental parameters affecting the measurement readouts. The experimental investigations involved spectral measurements, Scanning Probe Microscopy characterization, and luminescence time-resolved analysis. In particular, the hyperspectral imaging technique is employed to investigate the thermal response of different groups of ions inside a single particle. Computationally, it is employed algorithms to simulation the electronic population dynamics during light-matter interaction. This allows to test and further predict the behavior of lanthanoid systems to thermometry. The results discussed in this work can help understand more closely the internal and external factors interfering with the reliability of single micro and nanothermometers and establish a new method of surface effects analysis.

Keywords: luminescence thermometry; lanthanoid ions; energy upcoversion; single-particle spectrocopy; hyperspectral imaging.

RESUMO

A comunidade científica observa cada vez mais à fundo fenômenos em micro e nanoescala. A miniaturização de circuitos eletrônicos, equipamentos médicos e biológicos, e dispositivos de comunicação demanda investigações neste nível. Particularmente, medir temperatura em escalas submicrométricas é crucial para analisar inúmeros processos físico-químicos. Para este fim, ions lantanídeos dopados em matrizes de estado-sólido são de especial interesse devido as suas propriedades ópticas singulares. Entretanto, para de fato serem alcançadas altas resoluções espaciais, medidas em nível de partícula individual precisam ser empregadas, o que traz muitos artefatos físicos e instrumentais que podem perturbar a resposta térmica desses sistemas. Este trabalho tem o objetivo de caracterizar experimentalmente e teoricamente partículas individuais de $NaYF_4$: Yb^{3+}/Er^{3+} funcionando como termômetros, e também de investigar o papel de parâmetros físicos e instrumentais que afetam as medidas de temperatura. Os estudos experimentais envolveram medidas espectrais, caracterização por Microscopia por Varredura de Sonda, e análise da luminescência resolvida tempo. Em particular, a técnica de imageamento hiperespectral é usada para investigar a resposta térmica de diferentes grupos de ions dentro de uma partícula individual. Computacionalmente, foram empregados algoritmos para simular a dinâmica de população eletrônica durante a interação da luz com a matéria. Isto permite testar e posteriormente prever o comportamento de sistemas lantanídeos para termometria. Os resultados discutidos neste trabalho podem ajudar a entender mais profundamente os fatores internos e externos que interferem na confiabilidade de micro e nanotermômetros individuais, e a estabelecer um novo método de análise de efeitos superficiais.

Palavras-chaves: termometria por luminescência; íons lantanídeos; conversão ascendente de energia; espectroscopia de partícula individual; imageamento hiperespectral.

CONTENTS

1 INTRODUCTION

Many physical processes are associated with temperature changes. A broad spectrum of scientific research fields and industrial sectors relies on temperature measurements so that thermal sensors make up approximately 80 % of the global sensor market during this decade [1, 2]. Due to the rapid expansion of nanoscale technologies, the employed tools and probes have to follow correspondingly this level of miniaturization. Being temperature a key parameter to control and understanding many phenomena, the need for reliable thermometers at the nanoscale is an urging demand in fields such as microelectronic, microfluidics, nanophotonics, and nanomedicine [3, 4]. Many examples of direct application of nanothermometers can be cited: cancer cells have a higher intracellular temperature due to increased metabolic activity [5, 6]. Measuring intracellular temperatures can help in diagnosis and treatment; microcircuits present hot spots in critical points due to current flow [7, 8], so understanding spatially resolved heat dissipation in such systems can improve their performance and reliability; Microfluidics are intensively used in the development of lab-on-a-chip technologies, for example. Integrated temperature sensors help functionalize these devices [9].

In general, thermometers are composed of two main elements: a sensor and a modifier. The former is responsible for 'sensing' the environment and responds through some physical alteration of its properties. Basically, it converts one form of energy into another. The latter converts the measuring signal into human-readable information [10]. For example, in the mercury-in-glass thermometer, the mercury bulb is the sensor element, while the physical scale is the modifier element. Another important distinction regards primary and secondary thermometers [1]. In the first case, since temperature is an intrinsic parameter related to the entropy and total internal energy of a system, if one knows the equation of state governing an ideal gas, for instance, and the corresponding thermodynamic quantities, they can obtain the absolute temperature without previous calibration. On the other hand, in many systems, a reference thermal probe needs to be used to establish a calibration correspondence. Such thermometers are referred to as secondary.

Regarding the measurement interaction between the system and the probe, the thermometers are classified as contact, semi-invasive and non-contact [1, 10]. In contact thermometers, the thermal probe is in direct physical contact with the system. These are the most known and used in daily applications, which include mercury-in-glass, thermocouples, and thermistors. In

the non-contact approach, the temperature readout is made solely through optical analysis, as in the infrared pyrometers. Finally, in semi-invasive solutions, the probe is in contact with the system, but the temperature is recorded remotely.

Contact thermometers are not often suitable to probe temperature with higher spatial resolution ($< 10\,\mu m$) so the use of non-contact and semi-invasive approaches are mostly employed in thermometry at the micro and nanoscale. In particular, the main actors for semi-invasive methods include semiconductor quantum dots, organic dyes, crystallographic defects in nanocrystals, and lanthanoid-doped nanoparticles [3, 4]. However, to indeed achieve such spatial resolutions, the single-particle sensing level must be employed, and the scientific community is endeavoring to accomplish this challenge with reliability [11]. Particularly, lanthanoid ions in the trivalent state (Ln^{3+})-based thermometers are rapidly gaining attention due to their unique photophysical characteristics. The high photostability is the main point in favor [11]. For example, it is well known that single semiconductor nanocrystals may present a phenomenon called photoblinking, where the luminescence intensity suddenly vanishes, which limits their reliability and application as thermometers [12]. These phenomena are not seen in Ln^{3+}-based thermometry due to their electronic structure and the nature of the luminescence emissions. Another important feature is the efficient frequency upconversion presented in the Ln^{3+} systems. This makes it possible to work with luminescent thermometers in a broad range of the radiation spectrum, from ultraviolet to infrared frequencies. This wavelength tuning is especially important for biological applications to i) avoid tissue damage, ii) ensure a higher tissue penetration depth, and iii) avoid accentuated autoluminescence backgrounds [13]. We may cite other advantages of luminescence thermometry with Ln^{3+}-doped particles as: high emission quantum yield (> 50 %), narrows emission and absorption bands, coverage of temperatures from lower than 100 K up to 1000 K, and possibility of non-toxic and stable solid hosts [1, 14].

Besides direct thermometry applications, the single-particle measurement level allows to study more clearly the photophysical dynamics of such systems. For instance, in measurements employing colloidal suspensions or powdered samples, generally, a great number of particles are being probed simultaneously. This hinders possible interparticle discrepancies [15]. Also, it has been reported pronounced effects in the emitted luminescence due to crystal size [16, 17], surface ligands [18, 19], particle-particle interactions [20], and even proximity to a dielectric surface [21]. Such environmental constraints modify the photophysical dynamics and may change the thermometric response, as shown by Galindo et al. [22, 23]. In this sense, a

thorough understanding of the thermometer-environment interaction under various conditions is necessary to guarantee measurement reliability.

In this dissertation, it was characterized individual lanthanoid-based thermometers of $NaYF_4$: Yb^{3+}/Er^{3+}. The experimental procedures include spectral, time-resolved, and spatial-resolved studies. In particular, we employed a hyperspectral imaging system to separate the luminescence spectra emitted by the core ions from the surface ones. Chapter 2 presents the general theory regarding the spectroscopic properties of lanthanoid ions, including a discussion about the multiphonon emission and absorption phenomena. Chapter 3 discusses the theoretical foundations of temperature measurements on such systems, thermodynamically and quantum-mechanically, and the domain of validity of the assumptions. It also details the photophysical dynamics of Yb^{3+}/Er^{3+}. Chapter 4 encompasses the experimental apparatus used throughout the experimental studies. It details the optical microscopy systems, the scanning probe microscope, the sample preparation procedure, and the software and hardware solutions implemented to overcome the experimental challenges. In chapter 5, the measurement results are presented and discussed. A theoretical model is provided to explain the observed phenomena, and a computational solution is compared to the obtained data. Finally, chapter 6 concludes and presents perspectives for future works.

2 LANTHANOID IONS DOPED IN CRYSTALS

In this chapter, a basic understanding about the spectroscopic properties of the lanthanoid ions doped in crystalline matrices will be provided. We will start by discussing the general properties of free ions, then see how the crystalline matrix environment alters their spectra.

2.1 Brief recall of atomic spectra

The quantum states of atomic or ionic systems are determined by solving Schrödinger's equation[1]. For the hydrogen atom (or hydrogen-like ions), an analytical solution can be obtained and the quantum states are labeled by the quantum numbers n, l, m_l, m_s, standing for the principal, orbital, magnetic, and spin quantum numbers, respectively. In the case of complex atoms, although the solutions can not be derived analytically, we can still label similarly the quantum states due to the symmetry properties. In such cases, we have to employ approximations, usually assisted by computational methods. One of the most used models to describe complex atoms is the Central Field Model because it treats the potential energy seen by the electrons as purely radial. In this treatment, the energy level structure of complex atoms depends primarily on the n and l quantum numbers. Therefore, the orbital configurations are organized in shells ($n = 1, 2, 3, \dots$) and subshells ($l = s, p, d, f, \dots$). Since the ground state has minimal energy, the electron orbitals are filled in order of increasing energy. This is often called the *Aufbau* Principle, from the German *Aufbauprinzip* meaning building-up principle. On the other hand, Pauli's exclusion principle states that electrons should not simultaneously occupy the same quantum state. Accordingly, the electrons fill up the shells and subshells in the following energy order:

$$1s, 2s, 2p, 3s, 3p, 4s, 3d, 4p, 5s, 4d, 5p, 6s, 4f, 5d, 6p, \dots$$

As it can be seen, the $5s$, $5p$, and $6s$ configurations are less energetic than the $4f$, so those are firstly occupied. Despite this, the $4f$ configurations are not the outermost. The mean distance from the electron to the nucleus also depends on the n and l quantum numbers. The radial distribution of the $5s$, $5p$, and $6s$ subshells extend to a higher average radius than the $4f$ [24]. These closed outermost orbitals act by shielding the 4f subshell from external

[1] Depending on the electron configuration, specially in inner electrons in a multielectronic atom, a relativistic description must be included. Luckily, the outer electrons are still well-described by Schrödinger's equation.

perturbations, thus environmental effects on the optically active electrons (the electrons in the $4f$ subshell that will interact with the external electromagnetic field) are diminished.

After obtaining the solutions from the central field approximation, it is possible to include other effects such as electron-electron repulsion (if there is more than one electron in the subshell), spin-orbit coupling, crystal field effects, or any other corrections using perturbation theory. This central-field approximation, along with the perturbative corrections, is a good start to predicting atomic spectra.

2.2 Rare earth and lanthanoids

According to the International Union of Pure and Applied Chemistry (IUPAC) recommendations [25], the *rare-earth elements* comprises 15 metallic elements of the lanthanoid [2] series, from lanthanum ($Z = 57$) to lutetium ($Z = 71$), plus two other elements, scandium ($Z = 21$) and yttrium ($Z = 39$), that are frequently encountered in the same ore deposits, and have similar chemical properties, but distinct optical and magnetic responses [26].

In this work, we will be more concerned about the particular situation in which the atom, or ion, has the $4f$ electronic subshell partially filled (from 1 to 14 electrons) due to its special spectroscopy characteristics and ionic stability. In this sense, we call a $4f^N$-configuration ($N = 1$ to 14). The lanthanoids also tend to form ions with states of ionization 2+, 3+ and 4+, with the 3+ oxidation state (Ln^{3+}) being predominant [27]. When a lanthanoid atom is ionized to the 3+ state, for instance, it firstly loses the two electrons from the $6s$ configuration, then one electron from the $4f^N$ [27]. For example, the atom of erbium (Er) has the configuration [Xe]$4f^{12}6s^2$ ([Xe] stems from the xenon electron configuration), whereas the trivalent erbium ion (Er^{3+}) is [Xe]$4f^{11}$. Table 1 groups the elements that form the $4f^N$ configuration and their di-, tri-, and tetravalent $4f$ ions. Notice that not all rare-earth elements have a $4f$-configuration, thus despite the common denomination as 'rare-earth ions', the usage of the word 'lanthanoids' seems fit better.

Due to the energy-level structure of the lanthanoid ions, most of the light emission in the visible spectra regards electronic transition inside the $4f$ subshell, despite being forbidden by electric dipole interactions. Since the 1930s it is known that the f-f transitions in Ln^{3+} ions have higher intensities than expected by magnetic-dipole, electric-quadrupole, or any higher-order interaction [28]. The theoretical explanation for this observation came in the 60s with

[2] The term 'lanthanoids' is preferred over 'lanthanides' according to the IUPAC recommendations [25].

Table 1 – Atomic numbers and ground-state electron configurations for the considered di-, tri-, and tetravalent 4f ions

Atomic Number (Z)	Symbol	Electron configuration $4f^N$		
		Divalent	Trivalent	Tetravalent
57	La	$4f^1$	-	-
58	Ce	$4f^2$	$4f^1$	-
59	Pr	$4f^3$	$4f^2$	$4f^1$
60	Nd	$4f^4$	$4f^3$	$4f^2$
61	Pm	$4f^5$	$4f^4$	$4f^3$
62	Sm	$4f^6$	$4f^5$	$4f^4$
63	Eu	$4f^7$	$4f^6$	$4f^5$
64	Gd	$4f^8(4f^75d)$	$4f^7$	$4f^6$
65	Tb	$4f^9$	$4f^8$	$4f^7$
66	Dy	$4f^{10}$	$4f^9$	$4f^8(4f^75d)$
67	Ho	$4f^{11}$	$4f^{10}$	$4f^9$
68	Er	$4f^{12}$	$4f^{11}$	$4f^{10}$
69	Tm	$4f^{13}$	$4f^{12}$	$4f^{11}$
70	Yb	$4f^{14}$	$4f^{13}$	$4f^{12}$
71	Lu	-	$4f^{14}$	$4f^{13}$

Source: Adapted from Brik and Ma[27] (2020)

the independent work of Judd [29] and Ofelt [30]. They proposed that the f-f transitions occur through a forced electric dipole mechanism induced by the chemical environment as a perturbation on the free ion. We will be interested in the description of the spectroscopic properties of the f-f transitions as described by the Judd-Ofelt theory. However, because of the crystal field is still being treated as a small perturbation, it is worth studying thoroughly the properties of the free Ln^{3+} ion, which will be presented in the next section.

2.3 Spectroscopic properties of free lanthanoid ions

By applying the Central Field Model, the lanthanoid systems can be treated as if the $4f$ electrons feel an effective potential from the nucleus, diminished due to all the other filled inner electron shells. As the outer $5s$, $5p$ (and possibly $6s$) are also filled (thus spherically symmetric), we can disregard their contribution for the moment. The Hamiltonian of the free

atom (or ion) with N electrons in the unfilled f subshell can be written as [31]

$$H_{\mathsf{FI}} = H_0 + H_{e-e} + H_{\mathsf{SO}} \ , \tag{2.1}$$

where

$$H_0 = -\sum_{i=1}^{N} \left\{ \frac{\hbar^2}{2m}\nabla_i^2 + \frac{1}{4\pi\epsilon_0}\frac{Z^* e^2}{r_i} \right\} \ , \tag{2.2}$$

$$H_{e-e} = \frac{e^2}{4\pi\epsilon_0} \sum_{i<j}^{N} \frac{1}{|r_i - r_j|} \ , \tag{2.3}$$

$$H_{\mathsf{SO}} = \xi\left(r_i\right) \vec{s_i} \cdot \vec{l_i} \ . \tag{2.4}$$

H_0 accounts for the free electron motion under a central potential associated with the nucleus. The inner closed electron shells, considered as spherical, partially shield the nuclear charge, bringing an effective nuclear charge as Z^*. Different subshells (s, p, d, f) have different effective charges thus are influenced differently by the central field because of their different penetration inside the core. This term is the first responsible for splitting the degeneracy of the primary quantum numbers (n) in a multielectronic atom.

Secondly, H_{e-e} accounts for the electron-electron repulsion of the $N > 1$ unpaired electrons. At this point, the set $(n_i, l_i, m_{l_i}, m_{s_i})$, where i runs for each electron, does not form a good set of quantum numbers because the electrostatic repulsion breaks the individual angular momentum conservation. However, the *total* angular orbital angular momentum ($\vec{L} = \sum_i \vec{L}_i$) is still a conserved quantity, the same for the total spin ($\vec{S} = \sum_i \vec{S}_i$). As the energy now depends on the total angular momentum, the degeneracy will be split into $(2L+1)(2S+1)$ terms for different pairs of L and S, which comes from the eigenvalue equation for $\hat{L}^2$ and $\hat{S}^2$ operators [31]. For each defined L and S, we nominate a state with the term notation ^{2S+1}L.

H_{SO} is treated as a second-order perturbation and accounts for the spin-orbit interaction. $\xi(r_i)$ is the spin-orbit coupling function [32]. To diagonalize this perturbation term inside the $4f$ subspace, a change of basis is needed. We introduce the total angular momentum operator $\vec{J} = \vec{L} + \vec{S}$, with the eigenvalues of $\vec{J}^2$ being $\hbar^2 j(j+1)$ in such a way that the set (L, S, J, M_J) forms good quantum numbers. It happens that this set of quantum numbers is also good for diagonalizing H_{e-e} [31]. Therefore, regardless of the relative order between H_{e-e} and H_{SO}, the $\{|LSJM_J\rangle\}$ basis is still adequate. Now, the $(2L+1)(2S+1)$ degenerate states are split due to the spin-orbit coupling. Each of these is labeled by a final *spectroscopic notation* $^{2S+1}L_J$.

There can be employed terms for the many-body interactions as corrections of third order or higher [32]. However, besides the increased difficulty of handling these terms, their effects on the energy levels are much smaller than the previously discussed terms. We can disregard them for the sake of simplicity [27]. A complete treatment up to sixth-order can be found in reference [32]. Finally, despite the shielding of the optically active electrons, the crystal field can still be taken into account as a perturbation after H_{e-e} and H_{SO}. We shall see later that the crystal field is essential to the increased emission intensity of the f-f transitions. Figure 1 shows how each of the previously discussed interactions affect the energy levels and their relative splittings.

Figure 1 – Representation of perturbative effects on the removal of degeneracy of $4f^N$ configurations and the corresponding typical energy shift scales.

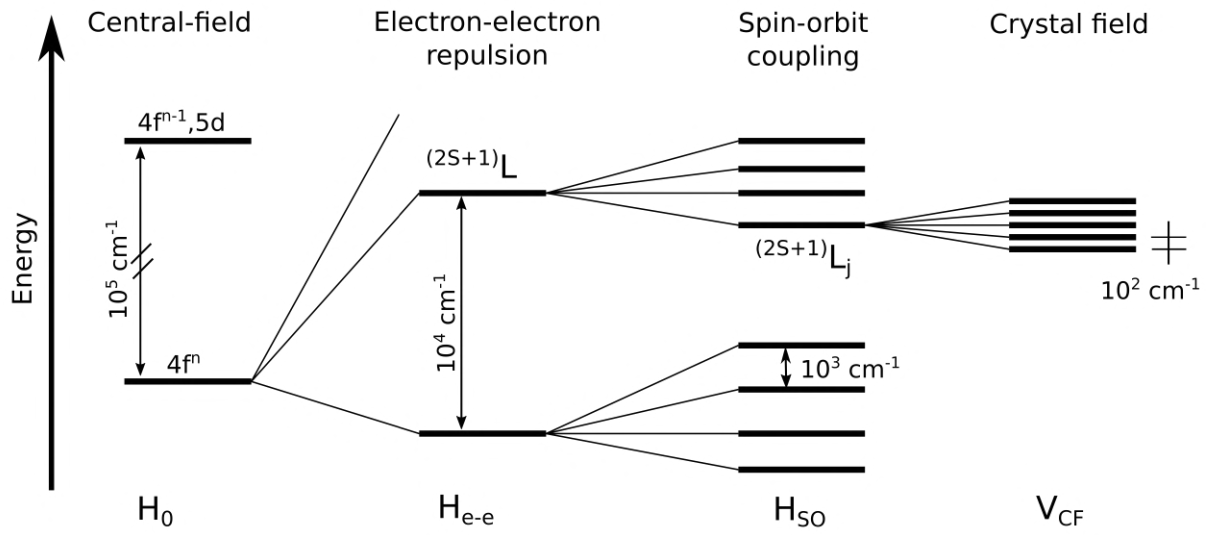

Source: Adapted from Filho, Lima and Serra[33] (2015)

2.4 Spectroscopic properties of lanthanoid ions inside crystal fields

As stated in the previous section, the effect of the crystalline field in the screened $4f$-electrons can be considered small compared to the electron-electron mutual repulsion and the spin-orbit interaction. However, despite promoting relatively small energy splitting, its perturbation introduced in the wavefunctions is the key to describing the high transition intensities inside the f subshell in lanthanoids, which is the scope of the Judd-Ofelt theory [33]. From a more qualitative perspective, the effect of the crystal field on the free ion spectrum can

be assessed with the help of group theory by using the relevant symmetries of the ion within the crystal. By applying group theory to spectroscopy it is possible to i) reveal qualitative information about the levels' degeneracy, ii) predict the levels splitting due to reduction of symmetries (by external agents, for example), iii) and establish the selection rules and the polarization characteristics of the transitions between these split levels [27, 34]. In addition, the unified classification and labeling are of great importance for future quantitative studies. The group theory applied to the study of lanthanoids doped in crystals relies on the fact that when the ion is surrounded by the crystal's atoms, called ligands, the resulting local symmetry is that of the crystal's structure. The eigenfunctions of the perturbed Hamiltonian will obey the symmetry operations that keep the ligand's position invariant. Thus, the previous eigenstates will be mixed up into sets that are invariant to the symmetry operation.

While group theory can provide qualitative information, the Crystal Field Theory (CFT) can be used to predict more quantitative information about the emission center. The Hamiltonian describing the system in which an ion is surrounded by ligands (in a crystalline lattice, for instance) depends, evidently, on the ligands' relative position to the central ion, called *optically active center*. The CFT consists in applying a perturbation theory to the eigenstates $^{2S+1}L_J$ of the free ion in order to split the degeneracies of the spin-orbit levels. This will result in the so-called Stark sublevels [35]. For example, the potential associated with the electrostatic interactions of the ligands with a single electron in the central ion can be written as [27]

$$V_{\mathsf{CF}}(\mathbf{r}) = \sum_i \frac{1}{4\pi\epsilon_0} \frac{Z_i e^2}{|\mathbf{R_i} - \mathbf{r}|} \ , \tag{2.5}$$

where i sums over all ligands in the unit cell. R_i is the position of the i-th ligand whereas r is the electron coordinate. The crystal field will act as a perturbation on the spin-orbit term $^{2S+1}L_J$, such that the wavefunctions will be mixed up inside the degenerated subspace. Computing the matrix elements of the potential (Eq. (2.5)) in the $\{|LSJM_J\rangle\}$ basis is demanding. It is usual to expand V_{CF} in spherical harmonic functions in order to facilitate the calculations. Reference [35] brings a more complete calculation.

2.4.1 Judd-Ofelt Theory

The interaction of the ion with the light can be considered as a perturbation that connects two electronic states. The electromagnetic energy can be absorbed by the ions' optically

active electrons, then it is excited to a higher energy level. Fermi's Golden Rule states that the transition rate ($w_{i\to j}$, transition probability per unit time) from $|i\rangle$ to $|j\rangle$ is proportional to the square modulus of the matrix element of the perturbation potential ($\hat{V}$), namely [36]

$$w_{i\to j} = \frac{2\pi}{\hbar}\left|\left\langle f\middle|\hat{V}\middle|i\right\rangle\right|^2 \rho_f \ , \tag{2.6}$$

where ρ_f is the density of states of $|j\rangle$. Electric-dipole transitions connect the states by the electric dipole approximation, which uses the first term of a multipole expansion of the classical field's Hamiltonian as the potential of interaction. The transition intensity between two states will depend on the matrix elements of the dipole moment ($\hat{P} = -e\sum_i \mathbf{x_i}$) [31]. We can classify the wavefunctions ($\psi(\mathbf{x})$) as having *even parity* if $\psi_e(-\mathbf{x}) = +\psi_e(\mathbf{x})$, or *odd parity* if $\psi_o(-\mathbf{x}) = -\psi_o(\mathbf{x})$. Only the angular part of the wavefunction will suffer changes by a parity operation, and it is possible to calculate the parity of a spectroscopic term by $(-1)^{\sum_i l_i}$, where l_i is the orbital quantum number of each electron, which is related to the angular momenta. It can be shown that $\left\langle \beta\middle|\hat{P}\middle|\alpha\right\rangle = 0$ when $|\alpha\rangle$ and $|\beta\rangle$ have the same parity [3] [36]. As a result, the f-f transitions in lanthanoids ($\Delta l = 0$) are forbidden by electric-dipole approximation. Only higher-order interactions are possible in this context, like quadrupole, octopole, etc. However, the transition intensities predicted by multipoles beyond the electric dipole are much lower than that observed for lanthanoid ions [28, 33].

To understand the puzzling behavior of lanthanoid ion emissions, it should be noticed that the symmetry reduction by the crystal field mixes wavefunctions with different parity states, for example, a $4f^N$ with a $4f^{N-1}5d$. This will happen when the crystal field is noncentrosymmetric, that is, has odd terms in its power-series expansion. These odd factors force a coupling between odd and even quantum states in lanthanoid ions, resulting in mixed paired states, that break Laporte's rule [28]. The transitions between these mixed states are called *forced electric dipole transitions* and successfully explained the oscillators' strengths observed in lanthanoids. Taking the crystal field as a small time-independent perturbation over the initial and final $4f$ states, as $\langle\phi_a|$ and $|\phi_b\rangle$, respectively, the mixed states can be written as

$$\langle\psi_a| = \langle\phi_a| + \sum_\beta \frac{\left\langle \phi_a\middle|\hat{V}_{\mathsf{CF}}\middle|\phi_\beta\right\rangle}{E_a - E_\beta}\langle\phi_\beta| \ , \tag{2.7}$$

$$|\psi_b\rangle = |\phi_b\rangle + \sum_\beta \frac{\left\langle \phi_\beta\middle|\hat{V}_{\mathsf{CF}}\middle|\phi_b\right\rangle}{E_b - E_\beta}|\phi_\beta\rangle \ , \tag{2.8}$$

[3] That is essentially the Laporte's selection rule.

where $|\phi_\beta\rangle$ are states of opposite parity and higher energy. E_a, E_b and E_β are the energies of the corresponding states. By using the dipole operator to calculate matrix elements of the dipole interaction, we get

$$\left\langle \psi_a \middle| \hat{P} \middle| \psi_b \right\rangle = \sum_\beta \frac{\left\langle \phi_a \middle| \hat{V}_{\mathsf{CF}} \middle| \phi_\beta \right\rangle \left\langle \phi_\beta \middle| \hat{P} \middle| \phi_b \right\rangle}{E_a - E_b} + \frac{\left\langle \phi_a \middle| \hat{P} \middle| \phi_\beta \right\rangle \left\langle \phi_\beta \middle| \hat{V}_{\mathsf{CF}} \middle| \phi_b \right\rangle}{E_b - E_\beta} \ . \tag{2.9}$$

Even though $|\phi_a\rangle$ and $|\phi_b\rangle$ are of the same parity, the matrix elements of $\hat{P}$ in the perturbed basis can be nonzero. The next steps towards developing Judd-Ofelt theory regard working on equation (2.9) to obtain the line strength of a forced electric-dipole transition (S_{ED}) in terms of the so-called *Judd-Ofelt paramters* (Ω_λ). In the final form, it can be written as [28]

$$S_{\mathsf{ED}}(J;J') = e^2 \sum_{\lambda=2,4,6} \Omega_\lambda \left\langle \alpha J \middle| \hat{U}^\lambda \middle| \alpha' J' \right\rangle \ , \tag{2.10}$$

where the $\hat{U}^{(\lambda)}$ refer to the irreducible tensor forms of the dipole operator and do not depend on the crystal symmetry, whereas Ω_λ depends on the crystal field, the radial part of the wavefunctions, and their energies [28]. Usually, the crystal-independent matrix elements ($\left\langle \alpha J \middle| \hat{U}^\lambda \middle| \alpha' J' \right\rangle$) are tabulated. The application of Judd-Offelt theory relies on fitting the Ω_λ from absorption spectra, then using it to calculate the probabilities of a given transition, along with its branching ratios and radiative lifetimes. This gives a thorough characterization of light-matter interaction in the $4f^N$ system. Obtaining the transition probabilities is important for modeling the population dynamics of lanthanoid system, as we will see in section 5.2.1.

2.4.2 Multiphonon transitions

In the crystal field theory, the ligands were taken as if they remained at rest, that is, we considered a static lattice. However, each ligand can oscillate around a fixed equilibrium position, therefore the doping ions must be considered as coupled to a vibrating lattice. This vibration promotes changes in the ligands' position, which alters the absorption and emission spectra of the impurity center. To consider it in the atomic description, we begin with the same Hamiltonian as in equation 2.1. The next step is to consider the crystal field as a perturbation over this Hamiltonian, as we have done, but now we call this term to be dependent dynamically on the ligands' position. Additionally, we must also consider the Hamiltonian of the ligands

themselves (H_{L}). It gets [27]

$$H = H_{\mathsf{FI}} + H_{\mathsf{CF}} \underbrace{-\frac{\hbar}{2}\sum_{\alpha}\frac{\nabla_{\alpha}^{2}}{M_{\alpha}} + \frac{1}{4\pi\epsilon_{0}}\sum_{\alpha,\beta}\frac{Z_{\alpha}Z_{\beta}e^{2}}{|R_{\alpha}-R_{\beta}|}}_{H_{\mathsf{L}}} \ . \tag{2.11}$$

In this case, $H_{\mathsf{CF}} = H_{\mathsf{CF}}(\mathbf{r_i}, \mathbf{R_j})$ depends on the coordinates of the valence electrons of the impurity center, $\mathbf{r_i}$, and on the coordinates of the ligands, $\mathbf{R_j}$. Generally, the deviation from the static-lattice spectrum for lanthanoid ions is small due to its shielding property on the optically active electrons. This produces a weak side-band in the spectrum due to the electron-lattice coupling. To solve the Schrödinger equation with the Hamiltonian provided in equation (2.11), we can approximate that the nuclei move very slowly compared to the valence electrons, the so-called *adiabatic approximation* due to Bohr and Oppenheimer in 1927 [34]. It makes the vibrational and electronic wavefunctions separable, being written as

$$\psi(\mathbf{r_i}, \mathbf{R_j}) = f(\mathbf{r_i}, \mathbf{R_j}) \cdot \chi(\mathbf{R_j}) \ . \tag{2.12}$$

$\psi(\mathbf{r_i}, \mathbf{R_j})$ is called a *vibronic state*, and couples the electronic wavefunctions with the vibrational states of the matrix. The matrix can be thought of as a 3D lattice of quantum harmonic oscillators. To obtain the $\chi(\mathbf{R_j})$ wavefunctions, the corresponding Schrödinger equation may be approximated by the Hamiltonian of an harmonic oscillator,

$$\sum_{s=1}^{N}\left(-\frac{\hbar^{2}}{2M}\nabla_{s}^{2} + \frac{1}{2}C(q_{s+1}-q_{s})^{2}\right) , \tag{2.13}$$

where q_s is the displacement of the particle s. A complete quantum solution of the Hamiltonian in equation (2.13) can be found in reference [37]. The boundary conditions of the problem will constraint the solution to possible *quantized* wavenumbers. This defines *vibrational normal modes*, and it can be shown that the problem can be separated in N independent harmonic oscillators. Therefore, each mode will have quantized energy levels. These collective excitations in the crystalline lattice are called the *phonons* of the matrix in analogy with the photons of the electromagnetic field.

The radiative transitions will occur between vibronic states. As the electric dipole operator does not involves the ligands' coordinates, it does not act on $\chi(\mathbf{R_j})$. The transition rate from the state $|i\rangle = |f_i\rangle\,|\chi_i\rangle$ to $|j\rangle = |f_j\rangle\,|\chi_j\rangle$ will follow, according to equation (2.6),

$$w_{i\to j} = \frac{2\pi}{\hbar}\left|\left\langle j\middle|\hat{P}\middle|i\right\rangle\right|^{2}\rho_{j} = \frac{2\pi}{\hbar}\left|\left\langle f_j\middle|\hat{P}\middle|f_i\right\rangle\right|^{2}|\langle\chi_j|\chi_i\rangle|^{2}\rho_{j} \ . \tag{2.14}$$

Therefore, transitions between vibronic states also depend on the relative overlap of the vibrational part of the wavefunctions.

Transitions between vibronic states do not necessarily involve the emission or absorption of light. More explicitly, they may not be described by dipole, or any higher-order multipole interactions. In this case, there is an exchange of energy between the electrons and the ligands through their vibrational energy, that is, there is a creation or annihilation of matrix phonons. These *nonradiative transitions* or *multiphonon transitions* can occur between vibrational states of the same electronic states, or between two different adjacent electronic states. The potential that connects two vibronic states in a nonradiative transition (electron-phonon coupling) is the dynamic crystal field acting on the impurity center. In this sense, H_{CF} in equation (2.11) can be split into a static field, which is represented by equation (2.5), and a dynamic field, which will account for the variation of the crystal potential in time [38]. Since the effect of the crystal lattice on the optically active electrons is weak in lanthanoid systems, the potential of interaction can be expanded in terms of the normal mode coordinates of the host lattice (Q) as

$$H_{\mathsf{CF}} = V_{\mathsf{st}} + \sum_i \frac{\partial V}{\partial Q_i} Q_i + \sum_{ij} \frac{\partial^2 V}{\partial Q_i \partial Q_j} Q_i Q_j + \dots \ . \tag{2.15}$$

The nonradiative transition rates will be calculated by applying perturbation theory using this dynamic potential. One-phonon transitions can take place when the initial and final vibronic states have an energy difference comparable to the energy of that phonon mode. In this case, only the second term on the right-hand side of equation (2.15) may be used in the perturbation. Higher-order processes can also occur, either by the application of higher-order perturbation theory to the first-order term, or by the consideration of higher-order terms in the expansion in equation (2.15). By taking the first approach for a p-order process, it is shown in reference [39] that the rate of nonradiative relaxation (emission of phonons) between two adjacent levels is given by $W_{\mathsf{NR}}^{\mathsf{em}} \propto (1 + n_k)^p$ where n_k is the occupancy number of the phonons with quasi-momentum $\hbar k$. Evidently, p is the number of corresponding phonons necessary to fulfill the levels' energy difference. Similar calculations can be performed for nonradiative absorption rates, giving $W_{\mathsf{NR}}^{\mathsf{abs}} \propto (n_k)^p$. The constant of proportionality depends also on the matrix elements of $\partial V / \partial Q_i$, but given two adjacent levels, it is the same for nonradiative emission and absorption. Moreover, each phonon mode has its energy and occupancy number, but one can consider a single effective phonon mode, with energy $\hbar\omega_{\mathsf{eff}}$, due to the small electron-

phonon coupling for the lanthanoids [40]. By accounting the degeneracies of the levels, the nonradiative transition rates from $|i\rangle \rightarrow |j\rangle$ is written as

$$W_{\mathsf{NR}}^{\mathsf{em}} = \mathrm{g_j} W_{\mathsf{NR}}^{(0)} (1 + \langle n_{\mathsf{eff}} \rangle)^p \ , \tag{2.16}$$

$$W_{\mathsf{NR}}^{\mathsf{abs}} = \mathrm{g_j} W_{\mathsf{NR}}^{(0)} \langle n_{\mathsf{eff}} \rangle^p \ . \tag{2.17}$$

The great number of phonons in the matrix at room temperature can constitute an ensemble following the Bose-Einstein statistic. Thus, it rules the temperature dependence of the nonradiative transition rates. The occupancy number is given by the Planck's formula [40]

$$\langle n_{\mathsf{eff}} \rangle = \left[\exp\left(\frac{\hbar \omega_{\mathsf{eff}}}{k_{\mathsf{B}} T} \right) - 1 \right]^{-1} . \tag{2.18}$$

If $T \rightarrow 0$ in equation (2.16), we get $W_{\mathsf{NR}}^{\mathsf{em}} = \mathrm{g_j} W_{\mathsf{NR}}^{(0)}$. The factor $W_{\mathsf{NR}}^{(0)}$ is regarded as the spontaneous phonon emission rate. Substituting equation (2.18) into equations (2.16) and (2.17), it gives the explicit dependence of the nonradiative transition rates with temperature:

$$W_{\mathsf{NR}}^{\mathsf{em}}(T) = \mathrm{g_j} W_{\mathsf{NR}}^{(0)} \left[1 - \exp\left(\frac{-\hbar \omega_{\mathsf{eff}}}{k_{\mathsf{B}} T} \right) \right]^{-p} , \tag{2.19}$$

$$W_{\mathsf{NR}}^{\mathsf{abs}}(T) = \mathrm{g_j} W_{\mathsf{NR}}^{(0)} \left[\exp\left(\frac{\hbar \omega_{\mathsf{eff}}}{k_{\mathsf{B}} T} \right) - 1 \right]^{-p} . \tag{2.20}$$

Furthermore, the dependence of the nonradiative rates with the energy difference between the levels can be obtained by approximating that a nth-order process follows $W^n \approx A\epsilon^n$, where A is a constant and $\epsilon \ll 1$ is called the *electron-phonon coupling constant*. This will lead to the so-called *energy gap law* [41],

$$W_{\mathsf{NR}}^{(0)} = \beta \exp(\alpha \Delta E) \ , \tag{2.21}$$

where α and β are constants that depend on the crystal system.

3 LUMINESCENCE THERMOMETRY

Given the general discussion presented in the previous chapter regarding the spectroscopic properties of the lanthanoid ions, we are going to narrow our analysis to the luminescence dynamics in a crystalline matrix codoped with two of them, Yb^{3+} and Er^{3+}, which is the main scope of this dissertation.

3.1 Upconversion mechanism

Although a luminescent thermometer is feasible by using a single-doping ion, like Er^{3+}, Nd^{3+}, Ho^{3+}, and Eu^{3+} [42], the codoped systems are fairly used because of their relatively higher quantum yield [43]. This is met when one of the ions act as a sensitizer, absorbing most part of the incoming energy and transferring it efficiently to an activator through a nonradiative process. The activator is responsible for emitting this energy radiatively, and that is the luminescent signal recorded. Two nearby sensitizer ions can absorb the excitation radiation and transfer their energy simultaneously to one activator ion, promoting the electrons to a higher-energy state. These electrons can decay radiatively producing a photon with a frequency higher than that used for excitation of the sample. This is one type of Upconversion (UC) phenomena.

The most used sensitizer in codoped systems is the Yb^{3+}. Ytterbium in the trivalent state forms a $4f^{13}$ configuration, according to the table 1. As the maximum number of electrons in the f subshell is 14, there is only one unpaired electron in the $4f^{13}$ configuration, which makes only two spin-orbit sublevels, $^2F_{7/2}$ and $^2F_{5/2}$, separated approximately by $10^4\,cm^{-1}$ ($\approx 980\,nm$). Therefore, the absorption cross-section of incident radiation with this energy is usually high. On the other hand, Erbium forms a $4f^{11}$ configuration thus having three unfilled electron configuration in the f subshell. This leads to the ground state configuration as a $^4I_{15/2}$ and a dense level structure. Among the possible codoped systems by using Yb^{3+} as the sensitizer (e.g. Yb^{3+}/Ho^{3+}, Yb^{3+}/Tm^{3+}, etc.), Yb^{3+}/Er^{3+} shows greater efficiency due to the good energy matching between their excited states ($^2F_{5/2}$ and $^4I_{11/2}$) [44], which is crucial for energy-transfer efficiency. Besides, the absorption cross-section of the Yb^{3+} ions at 980 nm is at least 10 times greater than that for Er^{3+} [45]. These special characteristics make this system to be the most used and reported in literature nowadays.

Crystalline matrices doped with lanthanoid ions are often used for this purpose due to the increased energy transfer efficiency. Nonetheless, the UC phenomena can occur without the need of a donor. One of the most common is Excited State Absorption (ESA), which is also relatively efficient in the lanthanoids because the intermediate levels have lifetimes of micro- or even milliseconds [43]. In a nonradiative energy-transfer process, the donor-acceptor interaction is governed by van der Waals interactions, with a distance-dependent coupling efficiency [43]. The lowest-order term of interaction is the dipole-dipole. Such mechanism is known as Förster resonant energy transfer. The rate of this process (γ_{ET}) is calculated by considering the matrix elements of the interaction potential over the electronic states of the two different ions. It can be demonstrated that [43]

$$\gamma_{\mathsf{ET}} = \frac{1}{\tau_{\mathsf{S}}} \frac{R_0^6}{\left|\mathbf{r}_{\mathsf{A}} - \mathbf{r}_{\mathsf{D}}\right|^6} \,, \tag{3.1}$$

where R_0 is a constant known by Förster radius, τ_{S} is the total lifetime of the sensitizer's excited state, and $\mathbf{r}_{\mathsf{D}}$ and $\mathbf{r}_{\mathsf{A}}$ are the positions of the donor and acceptor, respectively. Higher-order interactions are also possible, like dipole-quadrupole, and quadrupole-quadrupole, but their distance dependence will be different. The Förster radius depends on the overlap between the emission and absorption spectra of the donor and acceptor, respectively. Despite γ_{ET} rapidly drops to zero upon an energy mismatch, at room temperature the transfer can still happen through a Stokes or anti-Stokes process. In this case, the matrix matches the required energy through the lattice phonons [46]. Interestingly, the energy-transfer rate depends on the energy difference between the levels in the same way that the nonradiative rates (see equation (2.21)) [43]. Besides, as a multiphonon process, its dependency on temperature is similar as in equations (2.19) and (2.20) [47], and some authors use it to perform thermometry [48].

3.1.1 Upconversion power-law dependence

In the seminal work of Pollnau et al.[49], the authors studied theoretically, computationally, and experimentally the power dependence of the UC luminescence of a single ion. They showed that the luminescence intensity of a n-photon process is modeled by different power laws, depending on the competition between linear decay and upconversion processes. Being P the excitation power, they obtained a dependency of P^n in the limit of infinitely small upconversion rates, in contrast with P^1 in the limit of infinitely large upconversion rates, for the upper

state participating in the process. For intermediate states, the exponent can be lower than 1. Additionally, other photophysical effects also change the power-law dependence, such as cross-relaxation, excited-state absorption, photon-avalanche processes, energy transfer to impurities, etc.

To model the upconversion phenomena when there are sensitizer and activator ions, we must include them both in a system of rate equations. Consider the level scheme depicted in Figure 2 and the labeling for the photophysical processes provided therein.

Figure 2 – Scheme representing the population dynamics to model an upconverting system with sensitizer and acceptor ions.

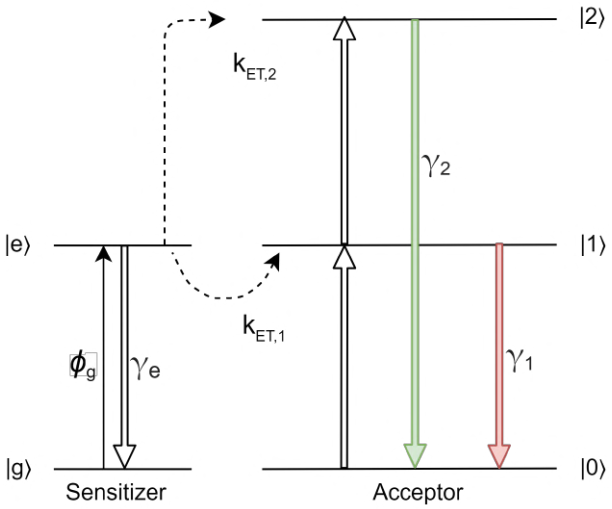

Source: The author (2022).

Here it is considered that the sensitizer ions absorb the continuous excitation radiation with a rate ϕ_g. The electrons in the sensitizer's excited state ($|e\rangle$) can transfer their energy to the activators (through the rates $k_{\mathsf{ET},1}$ and $k_{\mathsf{ET},2}$), or decay radiatively to the ground state (γ_e). Besides, the activator's excited states can also decay radiatively to the ground state (γ_1, γ_2). We can model the population dynamics by writing the time derivatives of the levels' population (n_i, $i = \{g, 1, 2\}$) as

$$\dot{n_g} = -\phi_g n_g + \gamma_e n_e + k_{\mathsf{ET},1} n_e n_0 + k_{\mathsf{ET},2} n_e n_1 \ , \tag{3.2a}$$

$$\dot{n_1} = k_{\mathsf{ET},1} n_e n_0 - k_{\mathsf{ET},2} n_e n_1 - \gamma_1 n_1 \ , \tag{3.2b}$$

$$\dot{n_2} = k_{\mathsf{ET},2} n_e n_1 - \gamma_2 n_2 \ , \tag{3.2c}$$

$$n_g + n_e = N_{\mathsf{S}} \ , \tag{3.2d}$$

$$n_0 + n_1 + n_2 = N_{\mathsf{A}} \ . \tag{3.2e}$$

where N_S and N_A as constants representing the ground-state population in the sensitizer and activator, respectively. ϕ_g is the population transfer rate from $|g\rangle \rightarrow |e\rangle$. It can be written as $\phi_g = \frac{\sigma_{ge}}{\hbar\omega_{ge}}\mathcal{P}$, where σ_{ge} is the absorption cross-section of the transition, $\hbar\omega_{ge}$ is the energy of the absorbed photon, and $\mathcal{P}$ is the irradiance (excitation power per unit area). In steady-state, all time derivatives vanish and we can solve the system (3.2) to obtain the steady-state populations. Usually, the irradiance in continuous excitation is low enough so we can consider the ground-state populations, n_0 and n_g, as constants. With these assumptions, we use equations (3.2b) and (3.2c) to obtain

$$n_2 = \frac{k_{ET,2}k_{ET,1}n_0n_e^2}{\gamma_2\gamma_1 + \gamma_2 k_{ET,2}n_e} \ . \tag{3.3}$$

Also, we can consider that the second-step energy transfer rate ($k_{ET,2}n_en_1$) is small compared to the other terms in equation (3.2a), so that we can extract n_e as

$$n_e = \frac{\sigma_{ge}n_g}{\hbar\omega_{ge}(\gamma_e + k_{ET,1}n_0)}\mathcal{P} = \kappa\mathcal{P} \ . \tag{3.4}$$

Combining equations (3.4) and (3.3), we obtain

$$n_2 = \frac{k_{ET,2}k_{ET,1}n_0\kappa^2}{\gamma_2\gamma_1}\frac{\mathcal{P}^2}{1 + \left(\frac{k_{ET,2}}{\gamma_1}\kappa\right)\mathcal{P}} \ . \tag{3.5}$$

Equation (3.5) shows the dependence of the upconversion process with the excitation irradiance, which is proportional to the total excitation power. The emitted luminescence intensity (I) by state $|2\rangle$ is directly proportional to n_2. For very low irradiances, $\mathcal{P} \ll \mathcal{P}_{sat} = \left(\frac{k_{ET,2}}{\gamma_1}\kappa\right)^{-1} \Rightarrow I \propto \mathcal{P}^2$, but as the excitation power increases, it gets $I \propto \mathcal{P}^1$. This is often regarded as the transition saturation. These results are in concordance with a simplified model presented in reference [50]. Notice that in this model, only upconversion and radiative transitions were included. Evidently, as previously said, if we include other routes of decay and/or absorptions, this picture changes. In section 5.2.2 the saturation effect will be shown experimentally for a single upconverting microparticle of $NaYF_4$: Yb^{3+}/Er^{3+}.

Microscopically, an n-step energy transfer needs n nearby sensitizer ions in the excited state, so they can 'collide' [51]. Energy migration is a type of energy-transfer process that happens between ions of the same kind. Its effect is found to play an important role in UC dynamics (temporal response) and power-dependency. In an Yb^{3+}/Er^{3+} system, for example, a sensitizer ion (Yb^{3+}) can absorb one photon, and this energy can migrate through different Yb^{3+} ions

until it is finally transferred to an Er^{3+} ion. Some authors, like Zuo et al.[51], uses Monte Carlo simulations to study the time-, and spatial-dependent role of actuators and sensitizers in the upconversion phenomenon, including the possibility of studying heterogeneous structures, and surface quenching.

3.2 Luminescence Intensity Ratio Technique

Numerous parameters can be used to infer the temperature from the probe luminescence, including i) the peak wavelength of a specific spectral line, ii) spectral bandwidth, iii) single-band intensity, and iv) life time [2]. Nevertheless, the most used and reported method in literature regards using the relative intensity variation of two spectral bands, which is a technique known as Luminescence Intensity Ratio (LIR). This method relies on recording the luminescence bands from two excited states that are close enough in energy to allow rapid exchange of electronic population through the matrix's phonons. Since the phonon occupancy number depends on the temperature (see equation (2.18)), one can predict the temperature of the host matrix by measuring the luminescence of the two *thermally coupled levels*. We shall see in the next sections the theoretical foundations supporting such temperature readouts.

3.2.1 Macroscopic approach

From a statistical mechanics point of view, we can say that the doping ions immersed in a solid-state matrix constitute a canonical ensemble. This ensemble is characterized by a physical system in thermal equilibrium with a heat reservoir. In our case, the doping ions constitutes the system, while the crystalline matrix represents the heat reservoir. Assuming non-interaction among the ions (separability), each constituent can be described itself as a canonical ensemble immersed in the matrix acting as the thermal bath. The number of ions is fixed, but the total energy can vary. Besides, the joint system (doping ions + reservoir) is said to be closed, constituting a microcanonical ensemble, meaning that it does not exchange heat, or particles, with the environment [40]. The solid-state matrix has a fixed temperature T, so the ions can exchange energy with the matrix in the form of heat to keep the thermal equilibrium.

By assuming thermodynamic equilibrium of the entire system, the fundamental postulate of statistical mechanics states that all permissible microstates are occupied with equal probability.

Within this basis, the probability of the system (single doping ion) being at a given microstate $|j\rangle$ can be calculated. Its derivation can be found in many statistical mechanics textbooks [52], and is given by

$$p_j = \mathrm{g_j} \frac{\exp\left(-\frac{E_j}{k_\mathrm{B}T}\right)}{\sum_i \exp\left(-\frac{E_i}{k_\mathrm{B}T}\right)} \,. \tag{3.6}$$

The sum in the denominator is the canonical partition function and goes through all possible microstates. Obtaining p_j itself depends on knowing the partition function. From a practical point of view, calculating the relative population between two microstates is more feasible. Consider the population of the quantum states $|1\rangle$ and $|2\rangle$ as N_1 and N_2, respectively. Since the population of the level $|j\rangle$ is $N_j = N_\mathrm{Tot} \cdot p_j$, the population ratio between N_2 and N_1 is given by

$$\frac{N_2}{N_1} = \frac{\mathrm{g_2}}{\mathrm{g_1}} \exp\left(-\frac{E_2 - E_1}{k_\mathrm{B}T}\right) , \tag{3.7}$$

which is known as the Boltzmann factor. Equation (3.7) is the basis of luminescence thermometry through the LIR technique. Notice that to achieve (3.7) it is necessary to impose that the doping ions are non-interacting. The only possible interaction is heat exchange with the reservoir (matrix). Practically, this is feasible when the two thermally coupled levels do not suffer significantly from quenching effects, such as cross-relaxation, ESA, or multiphonon depopulation to other levels. Besides, the radiative decay rate has to be much smaller than the nonradiative population exchange rate to ensure the thermal equilibrium. Indeed, as stated previously, the usual lifetime of the levels used to perform thermometry in lanthanoids ranges from microseconds to milliseconds, while the phononic transitions range picoseconds [53]. This approximation is, therefore, valid for most practical situations.

3.2.2 Microscopic approach

The macroscopic development in the previous section employs statistical mechanics arguments to introduce the Boltzmann factor. The matrix is the thermal reservoir, and it can exchange energy in the form of heat with the doping ions. From the microscopic point of view, the interaction of the matrix with the ions is regarded as the emission or absorption of phonons. The doping ion is said to be in a phonon bath (ruled by Bose-Einstein statistics), and the rates of population exchanges between the thermally coupled levels follow the nonradia-

tive interactions developed in section 2.4.2. Indeed, by assuming a two-state system that can only exchange electronic population due to multiphonon transitions, and disregarding radiative decays and all other feeding or quenching, the rate of electronic population in the state $|2\rangle$ is given by

$$\dot{N}_2 = W_{\mathsf{NR}}^{\mathsf{abs}}(T)N_1 - W_{\mathsf{NR}}^{\mathsf{em}}(T)N_2 \,, \tag{3.8}$$

with the restriction $N = N_1 + N_2$, N as a constant. If we substitute equations (2.19) and (2.20) in equation (3.8), and consider the steady-state, that is, $\dot{N}_2 = 0$, the ratio N_2/N_1 gets

$$\frac{N_2}{N_1} = \frac{W_{\mathsf{NR}}^{\mathsf{abs}}(T)}{W_{\mathsf{NR}}^{\mathsf{em}}(T)} = \frac{\mathrm{g}_2}{\mathrm{g}_1}\exp\!\left(-\frac{E_2 - E_1}{k_{\mathsf{B}}T}\right) , \tag{3.9}$$

where $E_2 - E_1 = \Delta E_{21} = p\hbar\omega_{\mathsf{eff}}$, and p is the number of effective phonons necessary to bridge the two levels. The previous equation recovers Boltzmann thermometry under the stated conditions. If we add another channel of depopulation, e.g. radiative decay to the ground-state, it shall perturb Boltzmann thermometry and the population ratio will not follow exactly the equation (3.9). Fortunately, the nonradiative rates in lanthanoids for thermally coupled levels with energy differences in the order of $\sim$1000 cm^{-1} are known to be much greater than the radiative rates. So that the thermal equilibrium between the thermally coupled levels is established much earlier than the times where radiative effects become relevant. For instance, Suta et al.[54] obtained the spontaneous phonon emission rate for the $^4\mathsf{F}_{5/2}$ and $^4\mathsf{F}_{3/2}$ levels in Nd^{3+} as $W_{\mathsf{NR}}^{(0)} = 54.6\,\mathrm{ms}^{-1}$. Hence, $W_{\mathsf{NR}}^{\mathsf{em}} = 219\,\mathrm{ms}^{-1}$ at 298 K for the multiphonon relaxation, while the radiative decay was obtained as $2.25\,\mathrm{ms}^{-1}$ for the lower level. In their case, the energy difference between the levels is in the same order than the matrix phonon effective energy ($\sim$1050 cm^{-1}).

Despite the provided approximations for validating Boltzmann thermometry, effects due to interactions between the activator ions are vastly known in the literature. One of the most established phenomena is Cross Relaxation (CR), which is sometimes referred to as *self-quenching*. In this process, an ion that is in an excited state partially transfer its energy to another nearby similar ion in the ground state, so they both go to excited intermediate states (not necessarily the same). Since CR is a type of energy-transfer process (mediated firstly by electric dipole interactions), the average distance between the ions controls its intensity. Therefore, lower activator ions' concentration can keep CR rates low. For this reason, it is also common in literature for the effect to be called *concentration quenching*. Exemplifying how

elevated CR rates can be harmful to luminescent thermometry in some cases, Suta et al.[54] showed that by increasing the concentration of Nd^{3+} ions in a crystalline matrix of $LaPO_4$, the Boltzmann equilibrium cannot be sustained at sufficiently low temperatures. The higher the concentration, the higher the temperature necessary for the system to follow the Boltzmann prediction. From their work, it is clear that the presence of additional feeding or quenching on the thermally coupled levels can interfere with the thermometric response. Therefore, modeling the upconversion process of these systems requires accurate knowledge of some microscopic parameters. In section 5.2.1 a model will be provided and solved for the photophysics of the Yb^{3+}/Er^{3+} system.

3.2.3 Temperature sensing with Yb^{3+}/Er^{3+} systems

In the case of luminescent thermometry with Yb^{3+}/Er^{3+}, the thermally coupled levels are the $^4S_{3/2}$ and $^2H_{11/2}$ from Er^{3+}, which have an energy difference of $\sim$700 cm^{-1}. The energy difference of these excited states to the ground state is in the order of 20×10^3 cm^{-1}, so the emitted radiation belongs to the green range of the visible spectrum. Figure 3 depicts the energy level structure of the Er^{3+} and Yb^{3+} ions in a matrix of $NaYF_4$, along with some possible transitions when excited with radiation at 977 nm. The energy data were collected from the diffuse reflectance spectra presented in reference [55], which is in excellent agreement with the theoretical calculations provided by García-Flores et al.[56]. In this latter reference, the authors calculate the crystal field splitting of the Er^{3+} energy levels in the $NaYF_4$ matrix. The energy splitting are not significant to be separated in Figure 3. The maximum energy difference of the Stark sublevels in the ground state ($^4I_{15/2}$) is 151 cm^{-1}, while for $^2H_{11/2}$ is 35 cm^{-1} and for $^4S_{3/2}$ is 54 cm^{-1} [56]. Such small energy differences make the Stark sublevels almost equally populated.

As discussed in section 3.1, the Yb^{3+} ions act absorbing most of the incoming radiation. A nearby Yb^{3+} ion can transfer its energy nonradiatively to an Er^{3+} ion, promoting electronic population to the metastable level $^4I_{11/2}$, which is resonant with the excited state of Yb^{3+}. A second energy-transfer process can take place and promote the electrons to the $^4F_{7/2}$ multiplet. This process is, again, resonant, so that the probability is relatively high. The population in $^4F_{7/2}$ rapidly decays nonradiatively to the $^2H_{11/2}$ and $^4S_{3/2}$, that are the levels commonly used to perform thermometry. Their radiative decay to the ground state produce spectral bands in the range 515 nm-535 nm and 535 nm-560 nm, respectively. As previously said, the $^2H_{11/2}$ and

Figure 3 – Energy diagram of Yb^{3+} and Er^{3+} ions in $NaYF_4$ matrix along with the energy-transfer processes between them. It is also shown two- and three-photon processes that provides spectral bands in the blue, green and red regions. Thin upwards arrows: Direct absorption by the ions; Thick upwards arrows: Energy-transfer upconversion from Yb^{3+} to Er^{3+} ions; Curly arrows: Nonradiative transitions; Thick downwards arrows: Luminescence emission; Dotted downwards thick arrows: Back Energy Transfer from Er^{3+} to Yb^{3+} ions. Energy-levels in scale.

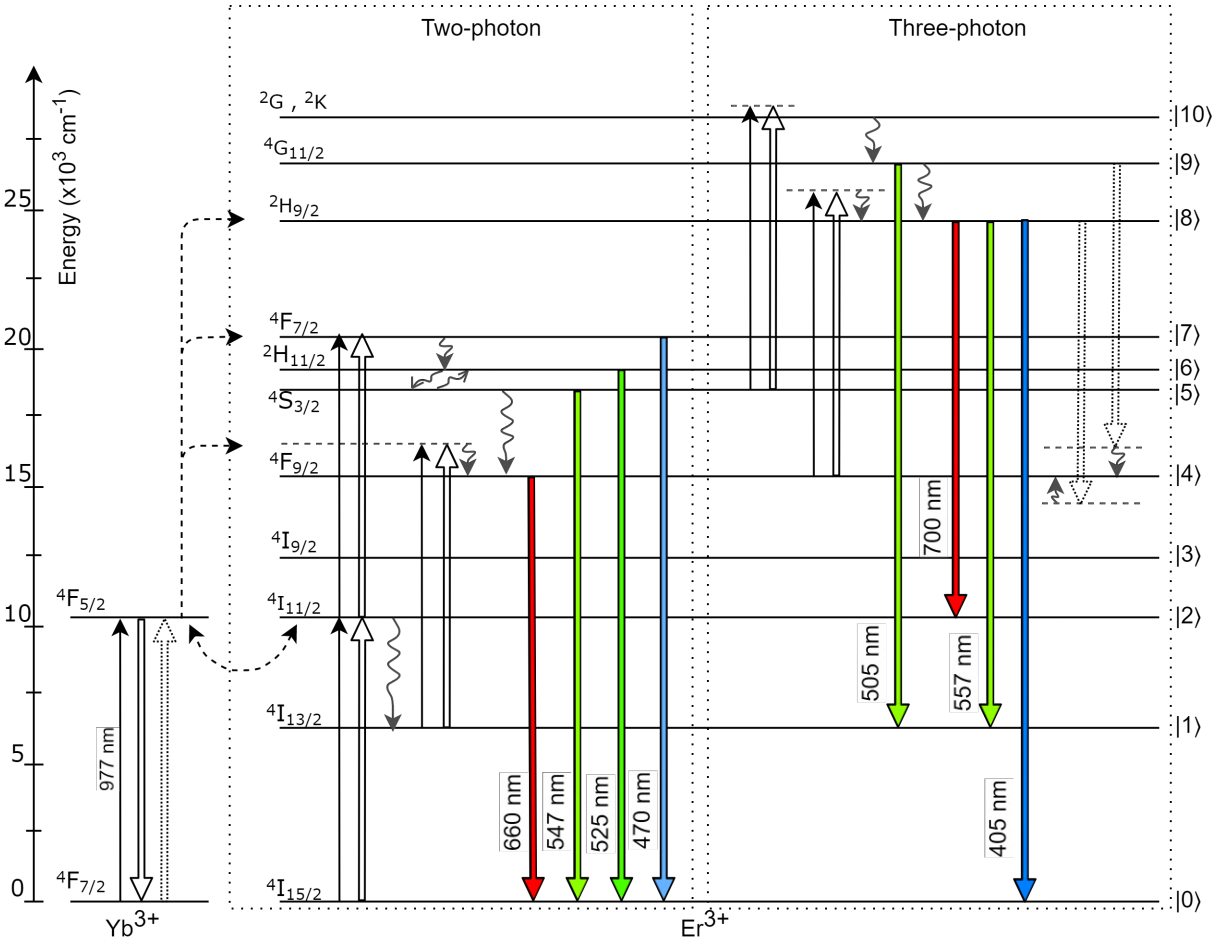

Source: The author (2022).

$^4S_{3/2}$ multiplets exchange population through nonradiative transitions mediated by the matrix's phonons. Depending on the doping concentration and the temperature, the thermodynamic approach developed in 3.2.1 can be applied for these two levels.

The Yb^{3+}/Er^{3+} system is also known to have a accentuated red emission band. Its origin derives from the radiative decay from the $^4F_{9/2}$ level to the ground state. To populate this level, there are some routes involving two-, and three-photon processes, this latter only takes place when the excitation power is relatively high [57]. For two-photon processes, a possibility is direct nonradiative decay from the $^4S_{3/2}$. Although the energy difference is high, thus requiring a third-order multiphonon process for the $NaYF_4$ matrix for example, there are experimental evidences corroborating with this assertion [15]. Another route comprises direct energy transfer

(or ESA) from the $^4I_{13/2}$ energy level, which is mainly fed by nonradiative decay from the $^4I_{11/2}$. There has been also reported the cross-relaxation route $^4F_{7/2} \rightarrow {}^4F_{9/2}$; $^4I_{11/2} \rightarrow {}^4F_{9/2}$ among the Er^{3+} ions (not shown in Figure 3) [58]. This latter can predominate when the doping concentration is high.

Higher-order energy-transfer processes are also possible, depending on the excitation power. For instance, some authors have found that three-photon routes can populate the red-emitting level [57, 59]. Under relatively high excitation power, there is a three-photon absorption from the $^4S_{3/2}$ to higher lying ^2G and ^2K states, which rapidly relaxates to $^4G_{11/2}$. Then, the electrons can suffer a phenomenon called Back Energy Transfer (BET), where energy is transferred back from Er^{3+} to Yb^{3+} ions: while the grounded Yb^{3+} ions go to the excited state, the Er^{3+} ones make $^4G_{11/2} \rightarrow {}^4F_{9/2}$. Another possibility relies on multiphonon decay from $^4G_{11/2}$ to $^2H_{9/2}$, followed by BET also to the $^4F_{9/2}$, as shown in Figure 3. In some systems, the red band is reported to have a higher intensity than the green one, especially depending on the concentration of Er^{3+} ions [60, 59], excitation power density [59], and surrounding medium [16]. This is attributed to the predominance of cross-relaxation and the BET pathways populating the red-emitting level. Other important three-photon process is the radiative decay from $^2H_{9/2}$ to $^4I_{13/2}$, originating a band at 557 nm. This transition has practical importance when performing thermometry because it overlaps with the $^4S_{3/2}$ band emission, as we shall see in section 5.2.2.

4 EXPERIMENTAL SETUP FOR SINGLE PARTICLE STUDIES

Now that we have discussed the general physics behind the spectroscopic properties of the lanthanoid ions, and how it is applied to temperature sensing, we are going to present the experimental techniques used in this work to study individual lanthanoid-doped particles as nano- and micro-thermometers. Our studies involved spectral, spatial, and time-resolved characterization, and each employed technique is discussed in detail.

4.1 Optical Microscopy

Although today's visualization of a microscope retraces to complex and powerful equipment, a single-lens magnifying glass is already characterized as an optical microscope. This configuration is called a *simple microscope*. Of course, the magnification power is very limited in such systems. On the other hand, the simplest *compound microscope* employs two convex lenses: an objective and an eyepiece. The former is placed closer to the object, and the latter is responsible to direct the light rays to the detector (which could be our eyes) [61]. Nowadays, the microscope systems are quite complex, involving numerous optical elements to avoid aberrations and improve performance. Moreover, the word 'microscope' is not only restricted to the realm of optical microscopes but can also refer to other types of microscopes that do not necessarily use light, like electronic microscopes or scanning probe microscopes.

The optical microscope is a device for enlarging the object's image, but there is a fundamental limit for distinguishing two nearby point objects in such systems, which is called the *resolution limit*. Consider an ideal point source irradiating at the optical axis in the object plane of a microscope system (the focal plane of the objective lens). The point source will radiate in all directions, but the objective lens will collect only a portion of the irradiated light. That is, it will only collect light within a range of wavevectors. Strictly speaking, there is a maximum angle at which a ray emanating from a point source can be collected by the objective lens. This angle is defined by the lens assembly itself, and a standard quantity used to compare different lenses is the *Numerical Aperture* (NA). The NA is defined by [62]

$$\mathrm{NA} = n \sin(\theta_{\mathrm{max}}) \ , \tag{4.1}$$

where n is the refractive index of the medium, and θ_{max} is the maximum angle that the

wavevector can make with the lens so the light could be collected. A schematic is presented in Figure 4. Therefore, the collected and emitted light will not share the same components in the spatial frequency domain because of this 'spatial filtering' by the lens [1]. The image of the object will suffer some spatial distortion, appearing with a finite size in the image plane. The narrower the spatial distribution, the better the resolving power of the microscope. The resolving power refers to the capacity of differentiating two nearby point sources. We shall exemplify it better in what follows.

An important concept, that is related to the NA, and that characterizes the microscope systems regarding its resolving power is the Point Spread Function (PSF), which is the system's response to a point source. In other words, the PSF of a microscope system is the intensity spatial distribution of the point source at the image plane. For example, consider the situation depicted in Figure 4: a perfect dipole oriented along the x-axis and the optical axis of the microscope along the z-axis. It is possible to calculate the field intensity generated by the point source in the image plane because we know the electric field generated by the dipole. In the paraxial approximation, the PSF in the focal plane for perfect free-of-aberration lenses will be written as [62]

$$I(x, y, z = 0) = I_0 \left[2 \frac{J_1(2\pi\tilde{\rho})}{(2\pi\tilde{\rho})} \right]^2, \quad \tilde{\rho} = \frac{\mathrm{NA}\rho}{M\lambda} , \tag{4.2}$$

which is known as the Airy function. In equation (4.2), J_1 is the Bessel function of the first kind, ρ is the radial coordinate defined according to Figure 4, and λ is the wavelength of the radiation emitted by the dipole. $M = (nf')/(n'f)$ is the magnification of the microscope setup, where f' refers to the focal distance of the objective lens, and n' to the refractive index of the object's immersion medium. The quantities f and n refer to the respective quantities for the image plane. Figure 4 shows the schematics of a compound microscope, along with the light ray tracing of a perfect point source (emitting in all directions) and its output at the image plane.

If now there are two point sources emitting light simultaneously so close that their Airy disk pattern overlap, their images at the image plane will not be distinguishable. This sets a *resolution limit* of the system, which is intrinsically connected to the PSF. Resolving two-point sources requires the sources to be separated by some minimum distance, and several resolution criteria have been proposed. For example, Rayleigh's resolution criterion finds that the mini-

[1] Also, in the far-field, the components associated with the evanescent waves are lost. Please refer to Novotny and Hecht[62], chapter 4, for more detailed information.

Figure 4 – Representation of a compound microscope and its response to a point-source at the object plane. ρ is the radial coordinate $(x^2 + y^2)^{1/2}$. $\Delta\rho = 1.21\lambda/(NA)$ is the distance between the two zeros of the Airy disk.

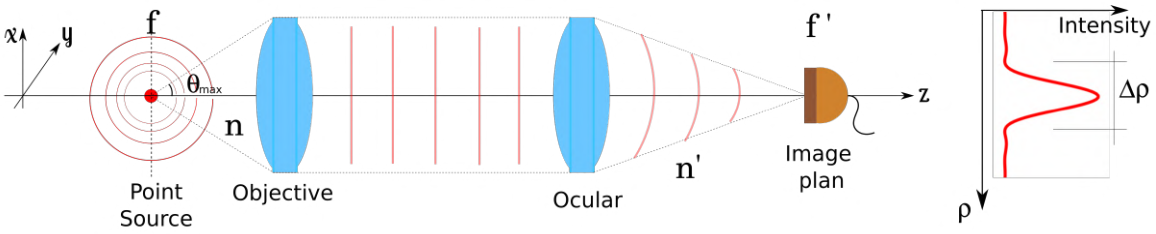

Source: The author (2022).

mum transverse separation between two points to be distinguished is $\Delta r_{\text{min}} = 0.6098\lambda/\text{NA}$, which corresponds to the distance between the central maximum and the first zero in the Airy disk (equation (4.2)) [61]. The resolution limit is important specially in our case because when working with nanostructures, we must be able to differentiate single-particles from aggregates.

As previously discussed, for thermometry applications by using the codoped Yb^{3+}/Er^{3+} system, we will be interested in probing the transitions of the thermally coupled levels to the ground state, which is in the green region of the spectrum. Considering the wavelength of detection as 550 nm, and a lens with a numerical aperture of $\text{NA} = 1.25$, we obtain $\Delta r_{\text{min}} =$ 268 nm. Similarly, the axial distribution of a point source is given by a sinc function [62]. The same Rayleigh criterion can be applied: the minimum axial distance between two point sources so they could be separately identified is when the first minimum of a point-source distribution meets the maximum of the other one. It gives the lateral resolution as [62] $\Delta z_{\text{min}} = 2\lambda/\text{NA}^2$. Calculating it by using our parameters results in $\Delta z_{\text{min}} \sim$ 704 nm.

After discussing some concepts in imaging using optical microscopes, it is important to give a brief overview on the sample illumination. One of the most common configuration for microscopy is wide-field illumination. In this case, a large area of the sample is illuminated by the light source simultaneously. Such configuration can be implemented in an inverted optical microscope setup (see Figure 5a), in which the objective lens is placed below the sample. The incident beam is focused at the objective back focal plane and collimated at the sample plane, illuminating a wide region. In Figure 5a) the incident radiation (red), often incoherent, interacts almost homogeneously with the sample. The interaction between light and matter produces luminescence and/or scattered radiation (green) which is collected by the objective lens and directed towards the detector. The resolution criteria as discussed above readily applies.

Also, other applications require local sample illumination to probe spatially-limited points

in the sample. Such configurations are called 'local-field' illumination. Figure 5b) shows this configuration in an inverted optical microscope. The excitation light reaches the objective lens as a plane wave and is tightly focused on the sample. This allows illuminating a single structure at a time. Since a spatially incoherent light source cannot be efficiently focused tightly, laser light is preferred in this situation. The separation of the excitation and fluorescence light is done by a beamsplitter or dichroic mirror, along with band-pass filters. Associated with this configuration there are several important techniques, such as confocal, and multiphoton microscopy. It happens that in these kinds of microscope configurations, the PSF have to take into account the spatial finiteness of the excitation source. This is because the radiating point source will interact differently depending on its relative position to the excitation beam. In general, the total PSF will be a convolution between the excitation PSF and the detection PSF.

Figure 5 – Two examples of inverted optical microscope configurations. a) wide-field illumination setup. b) Local-field setup.

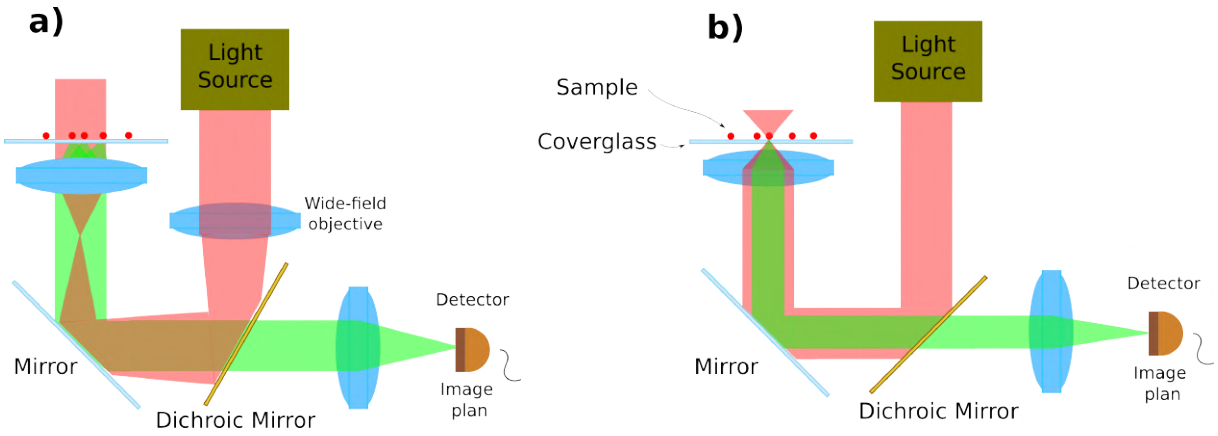

Source: The author (2022).

The dependence of the PSF with the excitation beam comes from the light-matter interaction. For example, in the linear regime, the single radiating dipole moment can be written as

$$\vec{p}(\omega;\vec{r}_s,\vec{r}_n) = \alpha(\omega)\vec{E}_{\text{exc}}(\omega,\vec{r}_s-\vec{r}_n)\ , \tag{4.3}$$

where $\vec{r}_s$ is the excitation beam coordinate, whereas $\vec{r}_n$ is the dipole coordinate, both relative to the same coordinate system. α is the polarizability tensor for first-order interactions. Notice that the dipole response depends on $\vec{r}_n$. To further obtain the spatial distribution of the dipole in the

image plane, we have to propagate the emitted radiation and consider the reflection/refraction on the lenses. Novotny and Hecht[62] expresses the electrical field at the image plane as

$$\vec{E}(\vec{r},\vec{r}_s,\vec{r}_n;\omega) = \frac{(\omega)^2}{\epsilon_0 c^2} \overleftrightarrow{G}_{\mathsf{PSF}}(\vec{r},\vec{r}_n;\omega)\cdot\vec{p}(\omega,\vec{r}_s,\vec{r}_n)\ , \tag{4.4}$$

where the tensor $\overleftrightarrow{G}_{\mathsf{PSF}}(\vec{r},\vec{r}_n;\omega)$ is the dyadic point-spread function, which is the Green function due to a point source [62]. Finally, the detected signal by a sensor positioned at the image plane is proportional to the intensity, that is, to $\left|\vec{E}(\vec{r},\vec{r}_s,\vec{r}_n;\omega)\right|^2$.

As shown, knowing the electric field $\vec{E}_{\mathsf{exc}}(\omega,\vec{r}_s-\vec{r}_n)$ is necessary to calculate the final PSF in local-field illumination. Since the excitation beam is focused by the objective lens, it will dictate the field distribution at the sample plane, depending of course on the input beam shape. The objective lens can be considered as a spatial filter to the input wave so that we can treat the problem as a similar diffraction problem. The lenses' usual aperture diameter and working distance (the distance from the lens front-end to the focal plane) are much greater compared to the wavelength of incident radiation, so we can treat the problem in the far-field region. This allows to consider light diffraction in the Fraunhofer regime [61]. The objective lens will project the input wave into a focal point. Due to the diffraction limit, at the focal plane the beam will have a minimum beam width, which is known as the beam waist. If the input beam is a plane wave, the focal field intensity is also described by an Airy disk [62]. Imagine now that the input beam has a Gaussian shape. The relative size between the input beam width at the objective entrance, and the lens aperture is critical to determining the beam waist. The larger the beam input width, the tighter the beam output spot on the focus. Figure 6 shows two different cases. The minimum spot is achieved by completely 'filling' the objective lens, that is, when the input wavefronts resemble a plane wave. When this condition is met, the Full Width at Half Maximum (FWHM) of the output beam is [62]

$$\mathsf{FWHM} = 0.51\frac{\lambda}{\mathsf{NA}}\ . \tag{4.5}$$

By using excitation at 977 nm and $\mathsf{NA} = 1.25$, one obtains a theoretical FWHM for a diffraction-limited excitation spot of ∼400 nm. This is important to calculate the irradiance of the incident beam on the sample, which is defined as the incident power per unit area being illuminated. Considering the area as a disk with a diameter of 400 nm, an excitation laser beam delivering 1 µW (usual values in our experiments) result in an excitation irradiance of $\sim$800 W cm^{-2}.

Figure 6 – Effect of the filling factor on the output beam waist when Gaussian wavefronts focus through objective lenses.

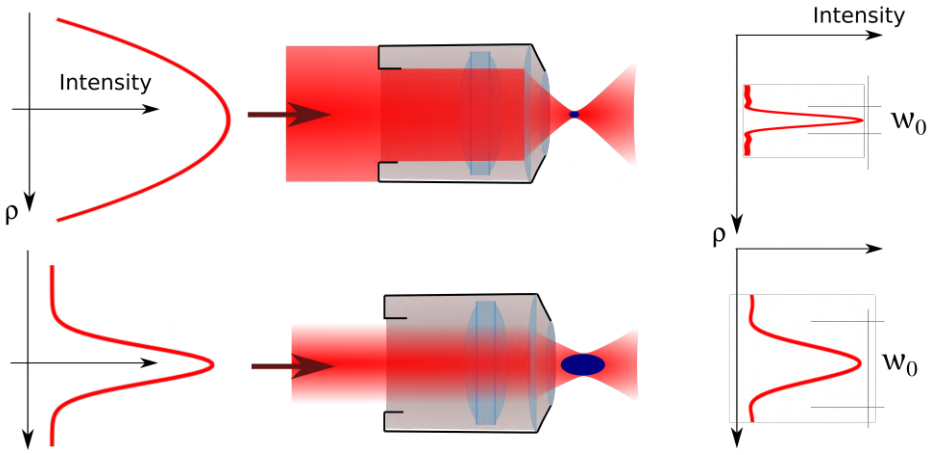

Source: The author (2022).

In our experimental apparatus, we employed either wide-field illumination - to have a broad image of the sample, or local-field illumination - to study individual particles. In this latter case, to probe the sample under different positions, we coupled it to a displacement stage, so we could perform a scan and consequently obtain an image. This configuration is often called *sample-scanning optical microscopy*. Studying individual nano- and microparticles is feasible by using a high-NA objective lens, so the light is tightly focused on the sample, with the beam diameter spanning hundreds of nanometers at the focal point. If the sample is properly prepared, that is, the crystals lay off individually on the coverslip, the microscope system can illuminate a single structure at a time, which is our main purpose. Thus, the sample preparation is critical for studying single particles and will be detailed in section 4.3.

4.1.1 Hyperspectral Imaging

As we have seen, in wide-field fluorescence microscopy a large area of the sample is illuminated simultaneously. For this configuration it is common to measure the sample luminescence using a CCD camera. But in sample-scanning optical microscopy, a computer-controllable translator performs a raster scan displacing the sample while the static laser beam is highly focused at the sample's plane. We then collect the luminous signal for each image pixel. This situation is suitable, for example, in our case, to study individual particles; or to study the optical nonlinear response of a sample, since the beam intensity is much higher at the focus. Depending on the target application, the luminescence intensity emitted by the sample is very

low, especially at the single-particle level. Hence, more sensitive photodetectors, at the single-photon level, must be employed, like Avalanche Photodiodes (APDs) and Photomultiplier Tubes (PMT).

Very often, the sample contains various different spatially-distributed specimens and/or inhomogeneities that have singular spectral signatures. In such cases, a spatially-resolved spectral characterization may be used to quantify these inhomogeneities, which is the aim of Hyperspectral Imaging (HSI). For example, in agriculture, the spectral response of a specific invasive weed may be monitored to avoid crop contamination [63]. Or in food analysis, where harmful composites need to be tracked [64]. Indeed, this technique serves as a tool to i) detect objects, ii) identify materials, and iii) study dynamic processes [65]. These features are possible because during hyperspectral measurements it is recorded a 'complete'[2] spectrum for each image pixel, obtaining a local spectral response of the sample. This compression is called a *datacube*. The high amount of collected data in a single image is advantageous to apply artificial intelligence algorithms. HSI along with machine learning-based methods are increasingly being used in fields such as agriculture, food processing, and mineralogy [65].

There are several approaches to performing HSI, the basic idea is to collect the light from a region of the sample, separate it using dispersive optical elements, and then send it to a detector array, which can be line arrays or 2D arrays [66]. Line arrays, as usual in most commercially available spectrometers, are used for point-scan detection, while 2D arrays can be used to line scan or even single shot detection. The main advantage of point scans is the high spectral and spatial resolution, whereas snapshot and line scans have the advantage of low acquisition times [66]. Other implementations include performing a wavelength scan instead of a spatial scan. In this case, the sample's image is collected, then the light is filtered by tunable band-pass filters before being detected in a 2D array.

Regarding nanoscience applications, HSI is increasingly gaining attention due to the constant miniaturization of the technologies [67]. Allied to the sample-scanning microscope, for example, HSI serve as a great tool to spatially characterize the light-matter interaction in micro and nanoscopic samples. For instance, there can be local lines shifts/broadening due to strain or temperature, or dynamic effects due to chemical reactions, in such a way that only by using the overall luminescence intensity (detected from single APDs or PMTs), this information is unavailable. In our experimental apparatus, we built a hyperspectral camera by acquiring the spectrum during a raster point scan. We synchronized the sample's spatial positioning with the

[2] Spectral acquisition features, like wavelength range and resolution are instrument-specific.

spectral measurements in order to attribute to each pixel a spectrum. In general, the spectral integration time is the main limiting factor to the overall scan time. Lower integration times decrease the total hyperspectral image acquisition times, but the collected spectrum tends to have poor signal-to-noise ratios.

Figure 7 – Experimental apparatus for spectroscopic studies of single particles. Legend: M - Mirror, L - Lens, FM - Flip Mirror, FL - Flip Lens, BP - Band-Pass filters, BS - Beam Splitter, ND - Neutral Density Filters.

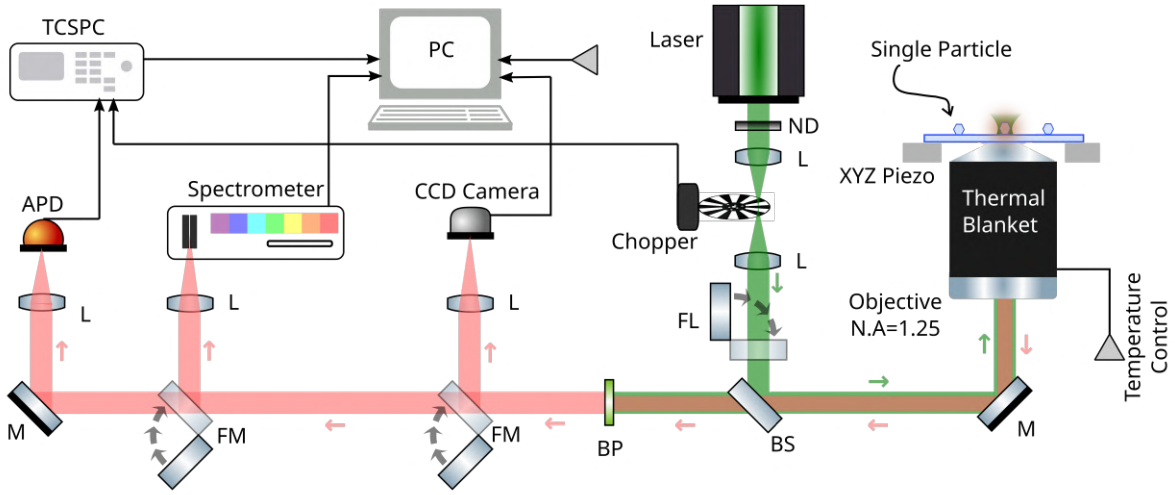

Source: The author (2022).

Our general experimental apparatus to detect and study spectroscopically single particles is shown in Figure 7. It possesses basically three measurement channels: i) Digital RGB camera - used jointly with the wide-field configuration to have an overall view of the sample. Notice in Figure 7 the presence of a flip lens before the beamsplitter responsible for wide-field imaging; ii) Photon-counter (APD) - for sample-scan luminescence imaging and time-resolved measurements; and iii) Spectrometer - for spectral studies of single particles and to perform hyperspectral point scans. All these equipment are connected to the PC for measurement and control. Since we are mainly interested in studying the physical response of luminescent thermometers, we developed an indirect heating system to control the sample's temperature. This is done by a computer-controllable thermal blanket that embraces the objective lens (oil immersion). The heat is transferred by convection and conduction to the immersion oil, passing through the coverslip and finally reaching the particle. After the sample temperature is changed in the heating system, it is needed to wait at least 20 minutes for overall thermalization. Moreover, the coverslip's temperature is constantly monitored by a thermal camera adjusted for glassy material's reflectivity and emissivity, serving as a calibration protocol for

the temperature sensors. This protocol is detailed in a previous dissertation from our research group [68].

4.1.2 Scan Software Design: NanoScanner

As we have seen, during scan our experimental setup makes it possible to sense the emitted light during an optical scanning either by the APD or by the spectrometer. In each case, it is needed to synchronize the data acquisition with the piezo's displacement. A Graphical User Interface (GUI) software was designed to control the measurement parameters, synchronize the numerous instruments, and manage the data collection either in a photon-counter scan, or in a hyperspectral scan. This platform was designated as NanoScanner. It was fully developed by the author in Python programming language, following the Model-View-Controller (MVC) architectural pattern. This project pattern is well-known in software architecture literature and is responsible for separating the data structure and management (Model), from the user interface (View), whereas the Controller performs the communication between both layers. Dividing the project into MVC components is ideal for software maintainability and further improvement.

Figure 8 shows an image of the initial screen of the program. At the top-right, we can choose the peripheral instrument to collect the data during the scan. The software backend was designed in such a way that the configuration of each instrument is independent of all the other components of the program so that a maintainer can easily add new equipment, routines, or modify the existing ones. This brings versatility to building images from numerous physical parameters. Our software also processes the scanned data to retrieve relevant information. For example, in a photon-counter scan, we plot the measured counts integrated over a specific period of time for each pixel, building an intensity map that does not distinguish the emitted wavelength (unless we use band-pass filters before the APD). On the other hand, in a hyperspectral scan, we can construct an image of a specific spectral band by integrating the spectrum over the specific wavelength limits. This flexibility allows further data processing features, such as background corrections, peak findings, fittings, etc. NanoScanner can be employed to perform these routines in real-time.

Figure 8 – NanoScanner designed software frontpage.

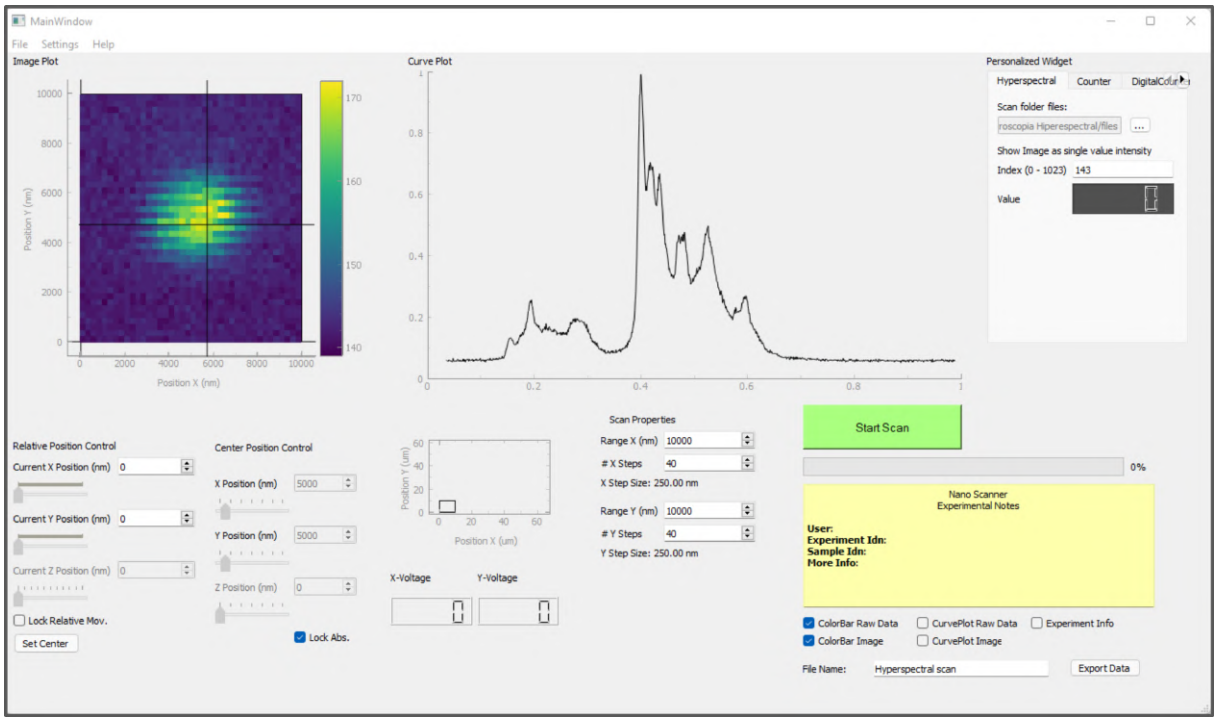

Source: The author (2022).

4.2 Time-correlated single photon counter design

Time-resolved spectroscopy is essential to understanding the dynamic process involved in the luminescence phenomena. The multiple feeding and decay pathways modify the temporal response during the excitation or relaxation of an electronic level. Such measurements are employed, for example, in fluorescent lifetime imaging, where each pixel contains time-resolved data and is further processed to obtain physical information [69]. Usually, a single-band intensity is monitored with a photodetector so we can study the photophysical dynamics of a separated emitting level. When performing measurements in colloidal suspensions or powders, where we can excite a large number of particles, the collected light intensity may be sufficiently high to use detectors such as simple photodiodes. Their electrical DC response may be sent to an oscilloscope where the rise and decay time after pulsed laser excitation is observed. However, in the single-particle regime, the level of the collected signal is very low, so photodetectors the single photon-counting level is often required, like APDs or PMTs. The output signal of single photodetectors is usually voltage or current pulses. In APDs, for each incoming photon, the semiconductor material creates an electron-hole pair that is accelerated by a large applied electric field. The charge carriers accelerated by the electric field then collide

with semiconductor defects, exciting more charge carriers and increasing the overall current by the so called avalanche process [70]. It is still necessary to implement a signal conditioning circuit to generate a voltage pulse with well-defined amplitude and width. In PMTs, the output current is enhanced by collisions albeit with a completely different construction. There are a series of dynodes (a metal plate made of a low workfunction material) under a high potential gradient, into a highly evacuated chamber [70]. When the photon hits the first metal plate (called photocathode), it generates electrons due to the photoelectric effect. These particles are accelerated to the following dynode and produce more electrons when they hit the next dynodes. At the end, there is a macroscopic current pulse, which also has to be conditioned by an electronic circuit.

Time-resolved measurements can reveal important characteristics in Ln^{3+} systems and their interactions with the environment. For example, it is well-known that increasing the doping concentration of Yb^{3+} ions in Yb^{3+}/Er^{3+} systems leads to a decrease in the total lifetime of the thermally coupled levels due to the back-energy transfer mechanism [71]. Also, the reported lifetimes of core-shell nanoparticles can be one order of magnitude higher than core-only particles due to the mitigation of surface quenching [72]. At the single-particle level, we observed that the effect of the laser excitation power can change the luminescence dynamics in Ln^{3+} systems, as will be discussed in section 5.3. Measuring the time dependency of such low-emitting processes requires i) an instrument for pulse-counting, ii) the separation of the counting in very well-defined time intervals refereed to a trigger event, and iii) A cumulative routine so that we could obtain measurable signals. These are characteristics of a Time-Correlated Single Photon Counter (TCSPC). In this work, we built a homemade TCSPC by using and Arduino DUE board for lifetime measurements and characterization of single-particle thermometers. The interested reader can refer to reference [73] regarding deeper theoretical aspects of TCSPC.

The Arduino is an open-source hardware and software platform, made to be user-friendly and help non-specialists to design embedded systems applications. Its huge community, which is one of the greatest advantages, includes teachers, hobbyists, and professionals. At the heart of an Arduino board, there is a microcontroller that is responsible for computing, data storage, and communication with peripherals. The Arduino uses the C/C++ programming language, along with a high-level framework that wraps most of the low-level instructions, to make the user experience and programming easier. The particular choice of an Arduino DUE was because of its microprocessor's clock speed of 84 MHz, which is the higher among the available boards.

This is essential to obtain good temporal resolutions. Also, since most APDs can generate up to 20 Mega Pulses per second and the arduino's internal counter hardware can count up to 42 mega pulses per second, this clock frequency is sufficiently high to neglect the possibility to miss photon counts.

The design of the TCSPC required hardware and software implementation. The hardware project includes the signal conditioning circuit responsible to adequate the pulse shape (amplitude and temporal width) before being directed to the Arduino board. The software project included the microcontroller's counting routines and data processing, and also a Graphical User Interface (GUI) to i) control the acquisition parameters more easily from the computer, and ii) analyze and process the output data. The former was programmed in C/C++ language, and the latter in Python. The data exchange between hardware and software is through the PC's USB port. Figure 9a) shows a photography of the hardware implementation. Figure 9b) shows the GUI. Our equipment is able to count up to 40 million pulses per second in-phase with multiple external signals above 100 kHz, and also emit triggering signals up to 42 MHz. Its minimum achieved integration time interval (time bin) was about 500 ns. Furthermore, it can be employed real-time digital signal processing.

Figure 9 – Home-built time-correlated single photon counter (TCSPC). a) Hardware implementation. b) Schematics of the acquisition routine in the boxcar averager mode. c) Software implementation.

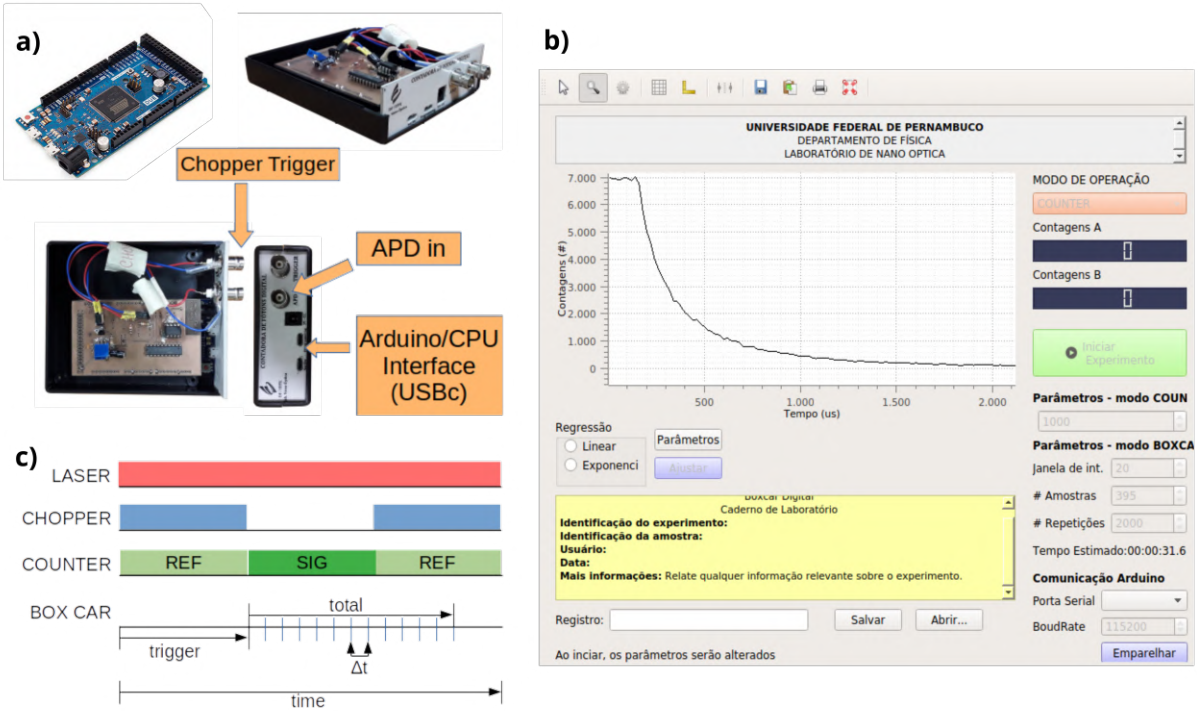

Source: The author (2022).

To obtain the luminescence decay curves we designed the TCSPC to work as a Digital Gated Integrator (also known as Boxcar Averager). In this mode, the equipment counts (integrate) the input signal separating the results into multiple time intervals, with predefined width. The beginning of the measurements is triggered by an external sync signal, defining whether the beam is exciting the sample, or not (in our case, this is controlled by an optical chopper). From this starting trigger, the user can still set a delay before the measurement start. Figure 9c) depicts the boxcar counting routine. It is worth mentioning that there are available commercial instruments to perform the task. Generally, these commercial counters have a very high temporal resolution, achieving picoseconds, while in our approach with Arduino we achieved hundreds of nanoseconds. However, the high cost of commercial solutions is the main limiting factor to it's widespread application in luminescence measurements. Besides, since the lifetime of Ln^{3+} ions doped in crystalline matrices ranges from hundreds of microseconds to milliseconds, our temporal resolution is already suitable. This equipment was also employed in another project from our research group: magnetometry measurements using single nitrogen-vacancy centers in nanodiamonds. The detailed implementation of this work is beyond the scope of this dissertation and can be found in our previous publication [74].

4.3 Sample preparation protocol

The sample used in the experimental studies of this dissertation was provided by the group of professor Sidney J. L. Ribeiro (UNESP, Araraquara-SP). The microcrystals of sodium yttrium fluoride ($NaYF_4$) codoped with Yb^{3+} and Er^{3+} were obtained by a thermal decomposition method known as hot injection. This method allows precise control of the size distribution and has been vastly used to synthesize upconverting nanoparticles in the past years [75]. In short, the synthesis involves heating a solution with oleic acid to approximately 330 °C, and then dropwise injecting another solution containing the oxide precursors (Y_2O_3, Yb_2O_3, Er_2O_3). The mixture is kept for 60 min at 330 °C under vigorous stirring and nitrogen flow. After it cools down to room temperature, the solid microcrystals with controlled size precipitate. Then, the crystals are washed multiple times to remove most of the oleic acid on the particle's surface. The crystalline phase of the synthesized microcrystals was analyzed by X-ray powder diffraction measurements, shown in Figure 10a). When comparing the X-ray diffraction pattern to the standard data for hexagonal β-$NaYF_4$ (PDF 00-064-0156) [76], it revealed that the synthesis procedure allows obtaining $NaYF_4$: Yb^{3+} (20%)/Er^{3+} (2%) in the hexagonal (β)

phase.

The crystal structure of the β phase is shown in Figure 10b). In Figure 10c) it is shown the room-temperature Raman spectrum of β-$NaYF_4$ micropowders in backscattering configuration. It is possible to see that the most intense phonon band has an energy of 161 cm^{-1} [77]. This relatively low phonon energy is important to the high efficiency of $NaYF_4$: Yb^{3+}/Er^{3+} systems because it suppresses nonradiative quenching [68]. In opposite to the cubic (α) phase, the β-$NaYF_4$: Yb^{3+}/Er^{3+} microcrystals are thermodynamically more stable and present higher UC luminescence intensity [13, 78]. One of the reasons for this higher efficiency is the strong cation disorder in the β phase (see Figure 10b), which enhances the resonance conditions for energy-transfers processes [77]. For a deeper discussion, refer to Renero-Lecuna et al.[77]. The hexagonal phase is a uniaxial material, so there is a well-defined optic axis in which the light propagating in this direction probes a different index of refraction than the light propagating transversally. This crystal anisotropy affects the luminescence of Ln^{3+}-doped ions due to the selection rules defined by the local site symmetry [79, 80].

Figure 10 – a) Powder X-ray diffractogram of the sample used in the experimental studies, along with the standard data of hexagonal β-$NaYF_4$ (PDF 00-064-0156). b) Crystal structure of the β-$NaYF_4$. c) Room-temperature Raman spectrum of the sample. The black line represents the measured curve, the green lines are Lorentzian peak fittings, the red dashed line is the sum of the green lines [77].

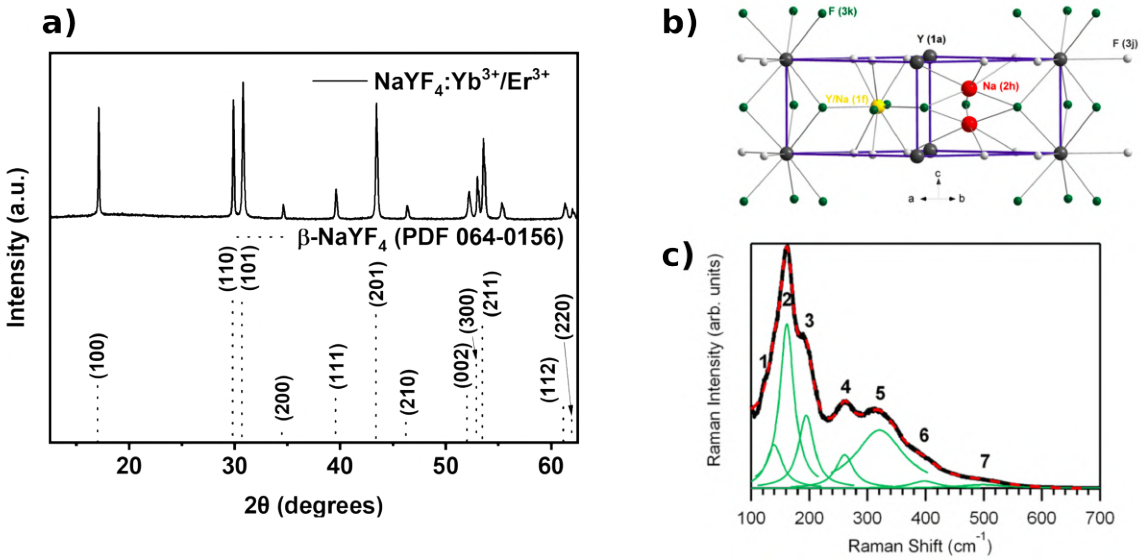

Source: a) Pessoa et al.[81] (2022); b) and c) Adapted from Renero-Lecuna et al.[77] (2011).

To perform the single-particle studies using a sample scanning microscope, the particles must lay individually onto the glass coverslip in such a way that the optical microscope can illuminate only one particle at a time. Therefore, the sample must be properly prepared. The

preparation procedure followed the protocol defined in a previous dissertation from our group [68]. Firstly, it is necessary to clean the coverglass. For most applications, cleaning with a detergent solution in an ultrasonic bath for 40 minutes is sufficient. After the chemical attack by the detergent, the coverglasses have to be rinsed with water, then it is submerged in a volatile solvent, as ethanol, isopropanol, etc. This latter step is necessary to accelerate their drying process, in which we use a blow of pure nitrogen gas to avoid contamination.

After obtaining the batch of microcrystals, they are suspended in pure toluene ($6.5\,\mathrm{mg\,mL^{-1}}$), for example, but they can easily form aggregates of particles because of the electrostatic attraction during drying. The solution containing these aggregates has to be strongly ultrasonicated in order to disaggregate. Usually, only the ultrasonic bath does not suffice, but a tip-assisted ultrasonication process has to be employed (typically for 5 to 10 minutes) to increase the local separating power. Finally, the solution is ready to the spin-coating process by dripping a small quantity of the suspension ($10\,\mu\mathrm{L}$) with the individual particles on a rotating glass coverslip. When the liquid reaches the surface, it exerts a centrifugal 'pseudo'-force which throws the particles away from the rotation axis (5000 rpm for 20 seconds). The solvent must be volatile because, during the rotation, the liquid is required to rapidly evaporate, so the particles remain separated.

The particles must be separated by a distance greater than the microscope's resolution, but not too far apart because this could make it difficult to find suitable particles for study. By carefully controlling the suspension concentration and solvent, the spin-coating parameters (rotation frequency and time duration), and the aliquot for dripping, it is possible to obtain a coverslip sample mostly consisting of individual particles (values detailed above). An Scanning Electron Microscopy (SEM) image of the sample can be seen in Figure 11a).

Although the preparation procedure protocol allows obtaining mostly single particles, some aggregates still can be found (see Figure 11a)). Depending on the resolving power of the microscope system and on the relative size of the particles, it will not be possible to optically distinguish single from few (2-3) particles at the focal spot. For example, in section 4.1 we calculated the minimum distance between two point sources to be resolved in our microscope system as $\sim$268 nm. It limits our analysis to particles of at least this size. For the sample used in this work, the particles have a micrometric size (average diameter of $1.4\,\mu\mathrm{m}$, see Figure 11a), so it is always possible to differentiate aggregates from single particles. However, this is not the case for studies involving particles with $\sim$100 nm by the same optical microscope apparatus. A possibility to overcome this pitfall is to analyze the total detected luminescence signal. If

Figure 11 – Scanning Electron Microscopy images of the $NaYF_4$: Yb^{3+}/Er^{3+} sample used in this study. Inset in a) shows the size distribution of 185 particles. The yellow circles are aggregates of two or more particles, which have been avoided for the studies presented in this work. b) Shows detailed the crystal morphology.

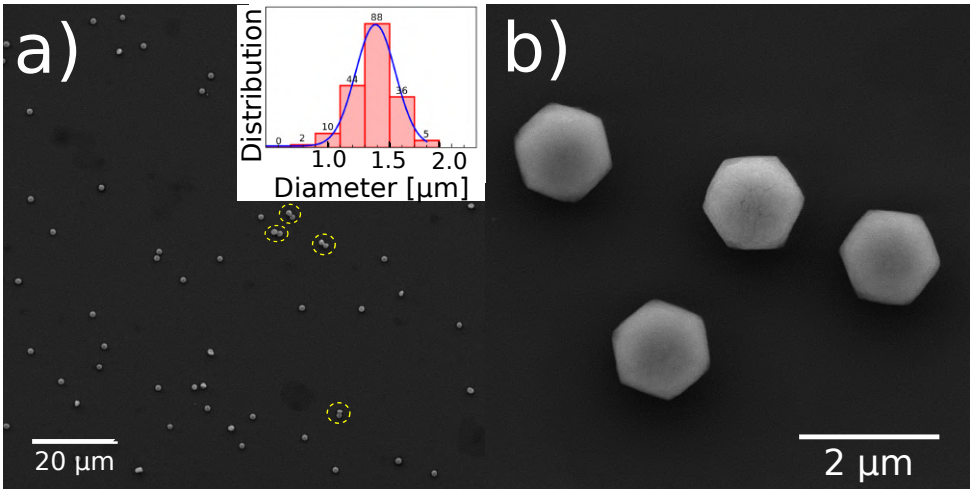

Source: Gonçalves et al.[15] (2021)

the signal doubles, it could indicate an aggregate of two particles. Nevertheless, this procedure relies on the monodispersity of the sample because the luminescence signal is proportional to the number of ions in the crystal, which, in turn, is proportional to the volume. If two crystals have a difference in radius of approximately 25%, the detected intensity will be different by a factor of two. Possible circumvents to this situation involves characterizing spatially the sample *in situ* with higher resolution before performing the optical measurements. That is, by using a technique that bypasses the optical diffraction limit. It includes super-resolution optical microscopy techniques, like stimulated emission depletion microscopy (STED), or Scanning Probe Microscopy (SPM) techniques. This latter was used in our experimental setup to image the topography of the microcrystals, and the implementation details will be given in the next section.

4.4 Scanning-Probe Microscopy

The Scanning Probe Microscopy (SPM) encompasses the set of techniques that use an extremely thin (nanometric) probe to interact with the sample, and thus obtain local information. Among the possible techniques, we can cite Atomic Force Microscopy (AFM), Scanning Tunneling Microscopy (STM), Scanning Near-field Optical Microscopy (SNOM), and others. SNOM in particular is used to collect the near-field radiation (evanescent waves). It uses a

nanometric optical fiber tip to excite and/or collect the optical information from the surface during a raster scan of the sample. The spatial resolution improves dramatically, especially along the distance perpendicular to the sample's surface. Evanescent waves travel through the surface without emitting radiation outward. They are not accessible in the far radiation field detected by typical imaging instruments. The probability of detecting near-field radiation rapidly vanishes within distances from the surface less than one wavelength, so the probe tip has to be sufficiently close the surface to collect these photons. In the SNOM approach, the tip's apex is kept at a constant distance from the surface, usually between 1 nm to 100 nm, a range called *shear-force interaction zone* [62]. This very fine position control is performed by a feedback loop where the tip's distance to the surface is regulated by their interaction strength. For the invention of this feedback loop, used in scanning tunneling microscopes, Gerd Binnig and Heinrich Rohrer were awarded the Nobel Physics Prize in 1986.

Besides regulating the tip-surface distance, the feedback control gives information about the topography of the sample with very high resolution. In this work, we also used the feedback response of a SNOM apparatus to obtain the topography images of the studied samples. The topography images serve as a guide to i) verify whether the particles under investigation are individual when the optical microscope fails to resolve, or ii) detect the sample's orientation, defects, or inhomogeneities. This apparatus is a great tool for the study of single-particle thermometers and their interaction with the surrounding environment. It is worth stressing that the SNOM technique is not restricted to obtaining the topography information, but its main purpose is to study the near-field radiation. This approach was not used in this dissertation and is a perspective for future works.

4.4.1 Probe-sample distance control

The tip has to be sufficiently close to the surface to probe its topography. A piezoelectric translator stage can make displacements in the range of nanometer or less, so it is used for position control. The active feedback control system drives the piezo stage depending on the tip-surface interaction. The nature of this interaction is not completely known. Most authors attribute to van der Walls interactions, but effects such as damping due to a surface humidity layer certainly influence [62, 82]. The overall physical phenomenon is the following: the tip is put to vibrate in a well-defined frequency transversally to the surface. When the tip apex approaches the sample, this latter imposes an additional drag force, in such a way that the

resonance conditions change. This shift is detected by the feedback control, which commands the piezoelectric stage to move proportionally in order to stabilize the probe-sample distance. Quantities that can be monitored during the loop include oscillation intensity, phase, and resonance frequency.

In our setup, the tip's vibration is driven by a tuning fork to which the tip is attached. This joint must be strong so that the tip's interaction with the surface can change the tuning fork oscillation conditions. An instant adhesive is used for this purpose. First, the optical fiber is aligned on the top of a tuning fork's prong with the protruding tip (see Figure 12a), then a small amount of instant adhesive is dropped in the lateral region near the prong's electrical contacts. The liquid rapidly spreads through the prong and after a few seconds it dries. The quality of this bonding is fundamental to the oscillation conditions. If the amount of adhesive is too small so the bonding is not strong enough, the tip-surface interaction will not change the tuning fork oscillation conditions sufficiently, resulting in poor sensitivities. Conversely, if it is too high, the system will hardly oscillate due to the strong resistance imposed by the adhesive. Figure 12a) shows the schematics of the tip-tuning fork assembly. Figure 12b) is a photography of an assembly manufactured in our laboratories. The optical fiber tip manufacturing itself requires careful handling and will be detailed in the next section.

Figure 12 – a) Optical fiber with nanometric tip coupled to a tuning fork and its main vibration mode. b) Image of the assembly manufactured in our laboratories.

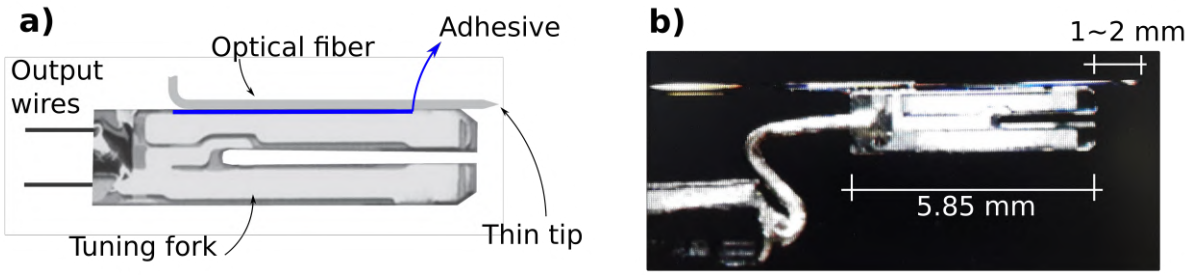

Source: a) Adapted from Novotny and Hecht[62] (2006). b) The author (2022).

The assembly works as a forced damped oscillator and can be modeled by the Butterworth–Van Dyke equivalent RLC circuit represented in Figure 13a). Its admittance is given by [62]

$$Y(\omega) = \frac{1}{R + (i\omega C)^{-1} + i\omega L} + i\omega C_0 \quad . \tag{4.6}$$

The amplitude of this function has a resonance peak centered at $f_0 = 1/(2\pi\sqrt{LC})$. As

previously said, controlling the apex height during a scan requires monitoring its resonance properties. In our case, admittance is the quantity monitored during the tip approximation to the surface. Before properly using the tip to perform topography images, one must verify if the adhesion is appropriate. To do so, we measure the resonance quality factor, Q. It is a quantity to evaluate the effect of damping in oscillators, being calculated as $Q = \Omega/\Delta\Omega$, where Ω is the resonance frequency and $\Delta\Omega$ is the FWHM of the resonance curve, also called resonance width.

A tunable function generator is responsible to drive the oscillator with a sine wave performing a frequency sweep with precision of 0.1 Hz around a fixed central frequency. The response of the oscillator to the driven function (admittance) is measured and amplified by an external electronic circuit and sent to an ultra-low noise preamplifier stage. Simultaneously, the generator also sends a sync signal to a lock-in amplifier, which filters the preamplifier's output and generates a cleaner DC response, which can be seen in an oscilloscope. In short, the lock-in amplifier basically multiplies the input signal by the sync signal, then integrates the result through a time period much larger than the input's period, resulting in a DC output signal. It is known that the signal can be decomposed into Fourier components (sines and cosines). If a particular signal component has a phase mismatch with the sync signal, the integration will attenuate the response due to the orthogonality of the sine/cosine functions. Only the in-phase component of the input signal will contribute significantly to the response. If this component has a low amplitude due to out-of-resonance oscillations, the lock-in output is diminished. On the other hand, if the oscillator is being forced near the resonance frequency, this component will override the signal, so the lock-in response will strongly increase. Figure 13a) shows a block diagram of the resonance profile measuring process, and 13b) shows a typical resonance curve of a tip assembly manufactured in our lab.

Higher Q represents low damping oscillators. The tuning fork itself has $Q \sim 7000$, whereas it reduces to $800 \sim 1600$ when the tip is attached. This serves as a parameter to certify that the assembly is well suited to be used in SNOM experiments. $Q > 2000$ represents poor tip-tuning fork bondings, while $Q < 800$ represents excess of adhesive during the manufacturing procedure. Besides, the response time of the system also depends on Q. The higher the Q-factor, the higher the sensitivity, but at the expense of a slower response, so a counterbalance is necessary [62]. The resonance frequency also depends on the tip's length outward the prong's end. Larger protrusions tend to have higher resonance frequencies.

After obtaining a suitable assembly, it can be used to approximate the surface. The tip-

Figure 13 – a) Block diagram showing the equipment used to obtain the resonance profile. b) Lock-in output to oscilloscope showing the resonance curve. The resonance frequency is $\omega_0 = 77.268$ kHz, and $\Delta\omega = 48$ Hz. Giving a Q-factor of 1609.

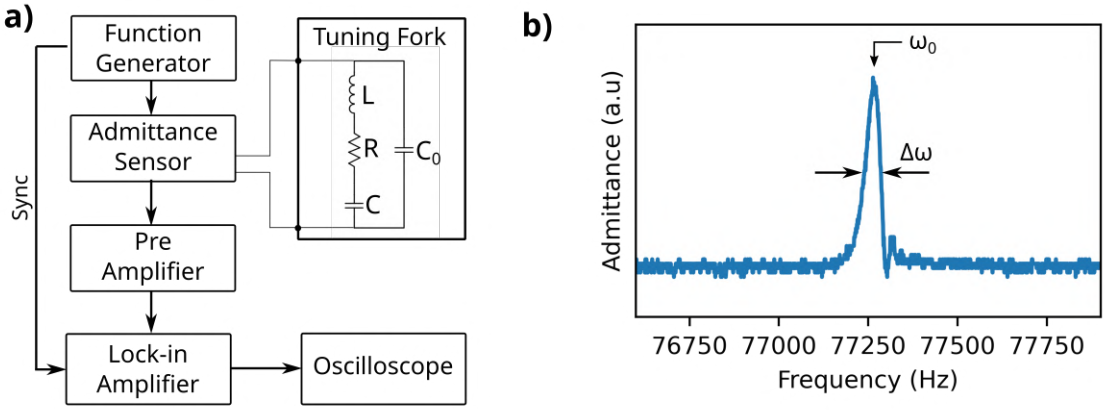

Source: The author (2022).

surface distance is regulated by an active feedback through a PI (Proportional-Integral) control that uses the Lock-in response as input. A PI controller receives a signal from an actuator and drives it to hold this signal at a constant setpoint. It continuously calculates the difference between the signal and the setpoint and applies Proportional and Integral corrections. Interested readers can refer to reference [83] for a thorough theory on PID controllers ('D' stems from Derivative, which is not used in our feedback loop). The output signal is further directed to another low-noise amplifier which drives the piezo system.

We fix the driving frequency below the resonance frequency so that the lock-in output be 90% of the resonance amplitude. This is approximately the point of maximum derivative in the resonance curve and is necessary to achieve higher sensitivities. This value also controls the probe-sample distance because it defines the range of interaction forces that will be necessary to be noticed by the feedback system. When the apex is in the range of shear-force interactions, the resonance frequency will increase and the quality factor will decrease [62]. As our input driving frequency is at 90% of the resonance frequency, we observe a decrease in lock-in response. Naturally, the noise of this response increases due to the feedback control of the distance around a fixed position. We measured oscillations of around 20 nm peak-to-peak during shear-force interactions. This value suffices to probe our sample of microcrystals, but for smaller particles this noise must be reduced. The tip oscillations can be reduced by using electronic circuits, or by changing the PI parameters. Of course, such tuning changes other characteristics such as the system's response time and it must be chosen adequately depending

on the target application.

The general block diagram representing the main agents in the SNOM technique is shown in Figure 14. The laser light coupled to the optical fiber is necessary as a guide to the eyes during tip approximation in our case but can be used to perform optical measurements in future works. The high voltage amplifiers are responsible for filtering most of the noise. Additionally, since the Z-direction is critical to longitudinal resolution, an additional RC filter can be coupled before the piezo's input. All communication with the computer is done through a Digital Acquisition (DAQ) system, which has several Analog-to-Digital Converter (ADC) and Digital-to-Analog Converter (DAC) channels. The former works as voltage inputs, and the latter as voltage outputs. The data acquisition and signal analysis is also performed by the NanoScanner software, presented in section 4.1.2.

Figure 14 – Block diagram showing the main components in our Scanning Near-Field Optical Microscopy implementation.

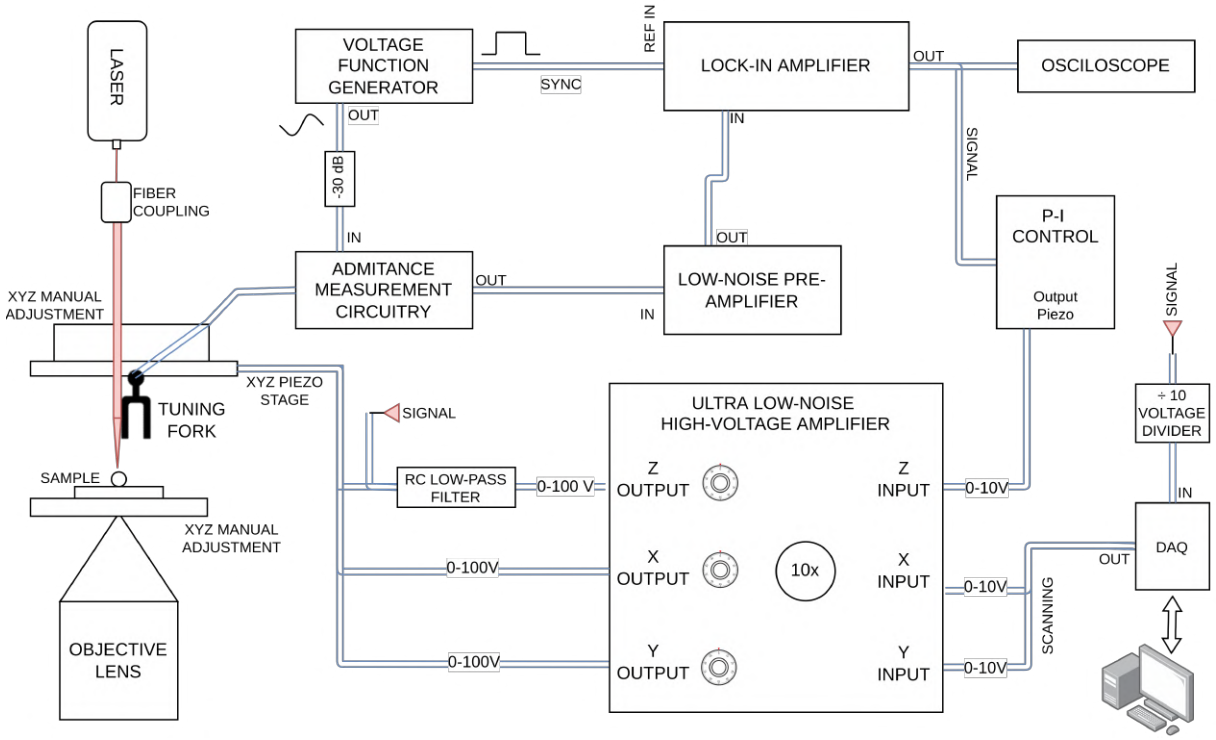

Source: The author (2022).

To form topography images, we measured directly the voltage signal being sent to the piezo z-axis. The raster scan records the piezo's voltage for each pixel. Post-processing the data allows to convert the voltage values to tip displacements. This is done by calibrating the piezo using a sample with previously known dimensions. In our case, we used two calibration probes: i) an AFM silicon grid with a constant height of (107 ± 2) nm, showed in Figure 15a).

And ii) a sample of highly uniform polystyrene latex beads with 100 nm diameter, shown in figures 15c) and 15d). Figures 15b) and e) show the recorded topography images for these calibrating probes. Post-processing resulted in different calibration values. The AFM resulted in 138 nm V^{-1} whereas the calibration using beads resulted in 303 nm V^{-1}. We attribute this difference either to the surface material, which can interact differently with the SNOM tip. However, more investigations are necessary to certify this assertion.

Figure 15 – Calibration of the SNOM apparatus. a) Scanning Electron Microscopy (SEM) image of the silicon grating used to perform calibration. b) Topography of the grating presented in a) measured by our Scanning Probe Microscope. The colorbar was built by using the output voltage/displacement conversion for this grating. The height *vs.* plot shows a topographic cross-section across the red dashed line. c) SEM images of the beads used as a second calibration control. d) Luminescence image collected by our inverted microscope of a region with 3 individual beads nanoparticles. The colorbar represents the number of emitted photons reaching the photodetector in kcounts per second e) Topography image of the corresponding region showing the very same particles. Colorbar was built so that the particle at the left superior has 100 nm height.

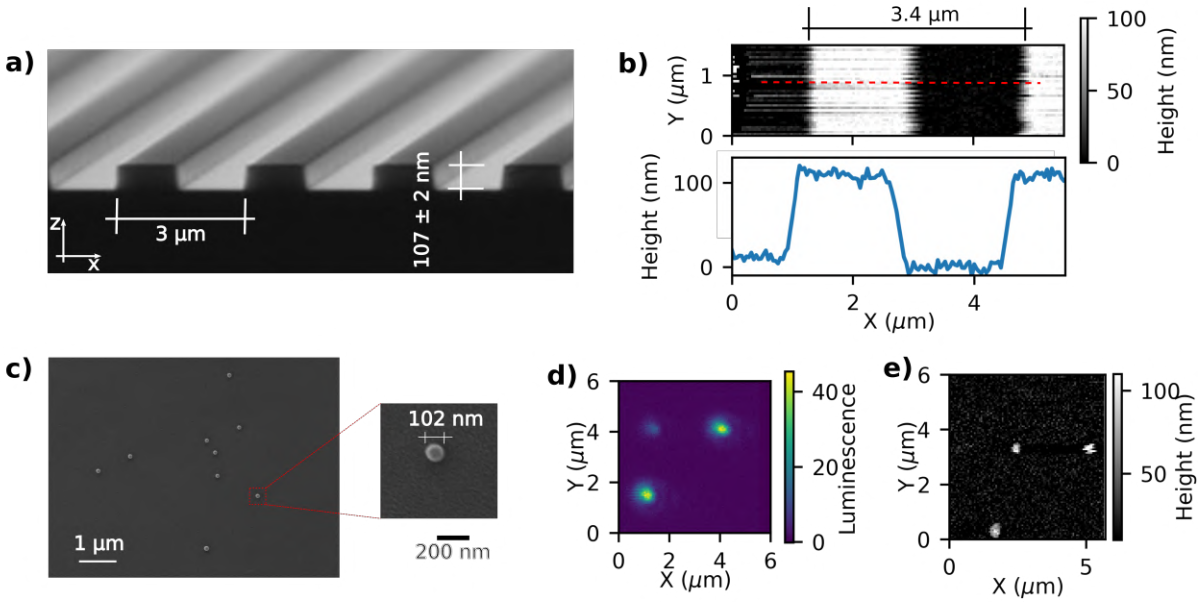

Source: a) TipsNano[84] (2022). b)-e): The author (2022).

Furthermore, the lateral resolution depends strongly on the tip's shape, including its size and eventual defects. With our fabrication procedure, detailed right below, good tips often have an apex length of around 70 nm. This makes the beads in Figure 15e) appear laterally with 240 nm to 360 nm, instead of 100 nm. Also, the period of the AFM grating in the SPM image is computed as 3.4 µm instead of the real 3.0 µm. Finer tips tend to result in improved lateral resolution, but the handling becomes cumbersome and the possibility of tip breaking during the scan is higher.

4.4.2 Tip fabrication

The tip's quality is crucial to obtaining good topography images. The finite size of its apex is the principal limiting factor to the image's resolution [85]. Consider an SPM tip probing a surface with a single-step barrier. Before the tip reaches the step, the feedback control will keep the height (tip-surface distance) constant. When the tip approaches laterally the barrier at a certain distance, it will interact and the feedback control may respond. Therefore, there is a distortion on the surface image due to lateral interactions. The sharpened wall will present a smooth uphill in SNOM topography. It is said that the obtained image is a *convolution* between the real sample's topography and the tip's shape. Once we know the latter, there can be used deconvolution methods to recover a more reliable topography image [86]. Conversely, the tip's shape can be recovered if one images a structure with known topography (which can be measured by other techniques, such as Scanning Electron Microscopy, for example).

Numerous sophisticated tip shapes are being proposed to improve resolution in SNOM [87], but the most used and reported are conical tapered optical fibers. There are two well-established methods to fabricate these tips from glass fiber. One of them is glass chemical etching, where a solution containing Hydrofluoric acid (HF) is used to dissolve the glass. In general, the uncoated bare fiber (remaining only the core) is submersed under the solution and the reaction occurs inwards. By controlling parameters such as the reaction time interval and the concentration, it can be obtained sharp tips. The advantage is that the tips can be mass-produced and the tapering can achieve very small sizes. However, depending on the specific technique, the geometry is not always conical and the surface can turn rough [88]. The other tip producing technique refers to the so-called 'heating and pulling' method. In this case, the uncoated optical fiber is pulled along its longitudinal direction while a CO_2 laser heats a very small volume of the fiber. The glass' local viscosity decreases and it can be modeled during the pull, resulting in two tapered tips. Naturally, the apex size depends on several parameters, such as pull strength (P), heating (H), velocity (V), delay (D), among others. But the main advantage of this technique is the smoothness of the conical shapes and geometry reproducibility. Moreover, other approaches are also used, like thin film deposition [87], or focused ion beam techniques [89].

To fabricate the tips for our experiments, we employed the 'heating and pulling' technique. We used a micropipette puller (Sutter Instruments CO. Model P-2000) to produce the tapered fibers by varying the above-mentioned P/H/V/D parameters. First, we get approximately 1 m

of optical fiber and remove its cladding ($\sim$1 cm) of the middle region. Then we couple it to the micropipette puller, adjust the parameters and start the pulling. A first certification test can be performed by coupling light to the non-pulled end of the fiber and observing the pattern it produces at the other extremity. For well-conical probes, the transmission pattern shows circular concentric rings. If the tip is damaged or non-concentric, we can see distortions in this pattern. For better characterization of the tip, and obtainment of its shape for deconvolution procedures, we can perform SEM images. Figure 16a) shows an schematic of the 'heating and pulling' method, while Figure 16b) shows a SEM image of a pulled tip with (H,V,D,P) parameters as (330 °C, 20 m/s, 124 ms, 150 N), assembled in our laboratories. The same parameters were used to produce the tips used to obtain the topography images presented in this work.

Figure 16 – Heating and pulling technique to fabricate tapered optical fibers for SNOM. a) Diagram showing the working principle. b) and c) are SEM images showing a conical pulled tip.

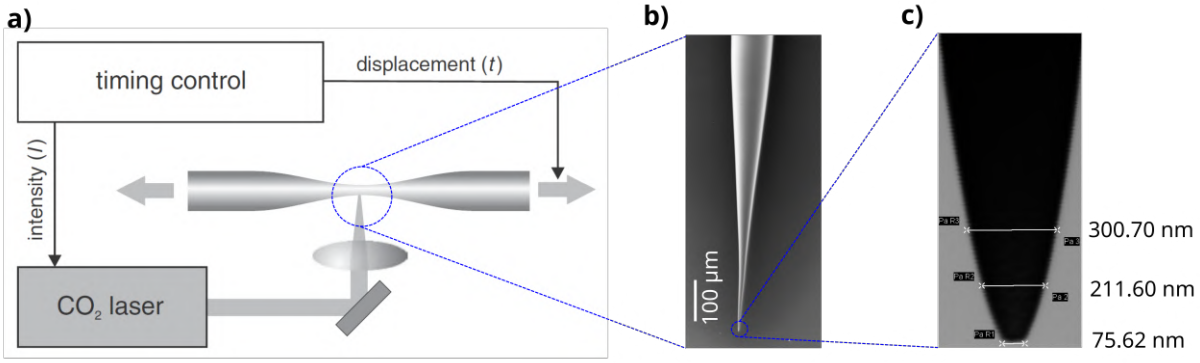

Source: a) Adapted from Novotny and Hecht[62] (2006); b) and c) The author (2022).

As we have stressed, topography images through AFM techniques depend substantially on the tip's shape. A very common artifact in SPM techniques is tip breaking during the scan. The tip's shape will be seen in the sample image and can override some important spatial information. To avoid tip breaking, it is necessary careful handling of the equipment. If the PI parameters are not well-tuned, there is a risk of the tip touching the surface during the longitudinal oscillations, resulting in deformation. Also, if the system is not sensitive enough, the tip can crash at the sample itself. Besides, other factors also influence the measurements. Temperature and humidity are one of the main sources of artifacts during the scan [90]. It is known that these parameters can modify the resonance conditions of the tuning fork [62]. Besides, the temperature can cause thermal expansions on the mechanical parts of the apparatus, including the sample. This can originate an artifact called scan drift. Since the

scan time duration usually takes from ten minutes, the on-off cycle of the air-conditioning control system systematically blurs the topography images. Further corrections are necessary, like dynamic background removal, where not only one background baseline is sufficient to correct the images. We can cite other numerous common sources of artifacts in SPM imaging, like i) probe-sample angle, ii) piezo stages non-linear response and hysteresis, iii) different piezo calibration for different axis, iv) background tilt, etc. [90] Since these artifacts are well known by the scientific community, there are plenty of algorithms and software available for image processing in SPM experiments. An interested reader can refer to the reference [91] for a more detailed discussion.

5 SINGLE-PARTICLE THERMOMETERS CHARACTERIZATION: EXPERIMENTS AND THEORY

Now that we have detailed the experimental techniques used to probe our sample of $NaYF_4$: Yb^{3+}/Er^{3+} single particles, in his chapter it is presented the experimental and theoretical studies employing these particles as temperature sensors.

5.1 Morphological characterization

The particles' morphology is particularly important for applications truly in the micro- and nanoscale. One of the standard methods to obtain the sample's morphological characterization is Electron Microscopy, but such technique cannot occur simultaneously with the luminescence measurements. To obtain topographic images on-site, we use the SNOM apparatus detailed in section 4.4. This raises information about the relative position of the particle on the coverslip and also serves as a complementary tool to define whether it is a single structure (especially important in particles smaller than the microscope's resolution). Besides, we can measure the particle's height and find possible structural defects. Another important feature that on-site topography images can provide is the visualization of possible other structures that may interact with the thermometer. For example, Schietinger et al.[92] showed that by coupling a gold nanostructure to an upconverting particle of $NaYF_4$: Yb^{3+}/Er^{3+}, it is possible to enhance the upconversion emission due to the plasmon resonance of the nanostructure [92]. Such a situation could be probed and controlled with the SNOM apparatus.

Figure 17a) shows the topography images of an individual particle probed with our SNOM apparatus. The conversion parameter used to obtain the particle's height was $303\,\mathrm{nm\,V^{-1}}$, resulting from the beads nanoparticles calibration (see section 4.4). Notice the hexagonal shape of the single crystals indicating the crystalline β phase, as discussed in section 4.3. We also observe in 17b) that the top basis is not completely flat, but presents a concavity. This shows that the particles are hexagonal rods, not prisms (which have a flat top surface). Both are possible morphologies reported in the literature for the β-phase in $NaYF_4$ matrices [93, 94]. From the SPM images, we obtain its FWHM as 1.8 µm, and the maximum height is 1.2 µm.

For comparison, it was shown in Figure 11 the Scanning Electron Microscopy (SEM) of other particles from the same batch. In Figure 11a), the particles show an average basis length of 1.4 µm, different from that measured employing SNOM. This difference is attributed to the

Figure 17 – *In situ* Scanning Probe Microscopy of a single particle. a) Topography image. The red dashed line represents the cross-section position ($Y = 1.25\,\mu$m) showed in b), in which the vertical dashed line marks the FWHM, obtained as 1.85μm.

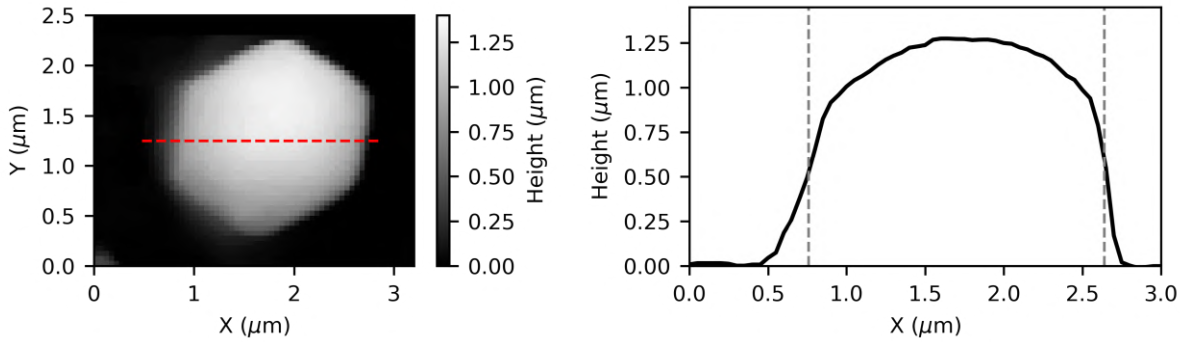

Source: The author (2022)

tip-dependent lateral resolution in SPM techniques, as detailed in section 4.4.2. Furthermore, the SPM and SEM images show that the microcrystals have an aspect ratio (ratio between the height and the basis average length) smaller than 1. This is important because it regulates how the particles are disposed of in the coverglass after spin-coating. In Figure 11a), we observe particles mostly with the hexagonal basis upwards, that is, with its symmetry axis perpendicular to the surface. For each article under study, this can be confirmed with the SNOM apparatus.

5.2 Thermometer characterization

To employ the single $NaYF_4$: Yb^{3+}/Er^{3+} particles as thermometers through the ratiometric technique, we need to calibrate them beforehand. First, a thermal reservoir with a controlled temperature is set, then the thermometer is put in thermal contact with it until thermalization. In our setup, the thermal reservoir is the computer-controllable thermal blanket (see Figure 7). After that, we obtain the thermometric parameter for that specific temperature. As previously discussed in section 3.2, our thermometric parameter is the Luminescence Intensity Ratio (LIR) measured from two thermally coupled levels. To obtain the LIR we need to record a spectrum in the region of interest, which is 515 nm to 570 nm in Yb^{3+}/Er^{3+} systems. Repeating the thermalization and measurement procedure for various temperatures allows us to construct a calibration curve.

The spectra are recorded by the spectrometer (monochromator Princeton Instruments Acton SP2500i + CCD camera Ardor Tech. iDus DU401A-BV). This equipment disperses the incoming light and directs each element of wavelength to a pixel in an array of CCD

photodetectors. Despite the number of pixels (wavelength elements) being discrete, we can treat the obtained spectrum as continuum because the usual wavelength step interval is much smaller than the band wavelength interval. Each CCD pixel measures the incident photon flux (ϕ, in photons s^{-1}). Therefore, the spectral response of the incoming light is the so-called *spectral photon flux* ($\mathrm{d}\phi(\lambda)/\mathrm{d}\lambda$, in photons $\mathrm{s}^{-1}\,\mathrm{nm}^{-1}$) [40]. The spectral resolution is determined basically by the grating elements used to diffract the light. Moreover, the CCD sensor and the dispersive elements can behave differently for different incident wavelengths thus we have to apply a correction factor regarding the wavelength-dependent detection efficiency, $\eta(\lambda)$. To calculate the total photon flux (average count rate) of a specific transition ($i \to j$) reaching the CCD (ϕ_{ij}^{CCD}), one must integrate the obtained spectrum curve over two given wavelength limits, which can be written as [40]

$$\phi_{ij}^{\mathrm{CCD}} = \int_{\lambda_a}^{\lambda_b} \mathrm{d}\lambda \eta(\lambda) \frac{\mathrm{d}\phi(\lambda)}{\mathrm{d}\lambda} \,. \tag{5.1}$$

λ_a and λ_b stand for the initial and final wavelength comprising the corresponding luminescence emission band, respectively. Even though spectrometers do have a detection efficiency curve, we considered $\eta(\lambda)$ as a constant in the measured wavelength range because the separation in energy between the thermally coupled is relatively small. Since the thermometric parameter is ratiometric, we should not expect $\eta(\lambda)$ to influence our measurements.

The probability of the ion emitting a photon in the transition $i \to j$ is $k_{i,r}\beta_{ij}n_i$, where $k_{i,r}$ is the total radiative decay rate (including all lower-lying levels), β_{ij} is called the branching ratio ($0 < \beta_{ij} < 1$, $\sum_j \beta_{ij} = 1$), and n_i is the electronic population of the emitting level. Very often, we call the radiative transition rate to the ground state as γ_i, so $\gamma_i = k_{i,r}\beta_{i0}$. This is just to simplify the notation. Let us call the two thermally coupled states as $|1\rangle$ and $|2\rangle$, the latter with higher energy, and the ground state as $|0\rangle$. In Yb^{3+}/Er^{3+} systems, the branching ratios to the ground-state (β_{20} and β_{10}) are generally much greater than the others [55] therefore we often look to this transition (in the green region). The LIR (R) will equal the ratio of the photon flux emitted by the transitions of the thermally coupled levels to the ground state. Since the spectrometer detects the photon flux per unit wavelength, which is proportional to the probability of the luminescent emission, we obtain the correspondence

$$R = \frac{\gamma_2 n_2}{\gamma_1 n_1} = \frac{\phi_{20}^{\mathrm{CCD}}}{\phi_{10}^{\mathrm{CCD}}} \,. \tag{5.2}$$

In Yb^{3+}/Er^{3+} systems, ϕ_{20}^{CCD} is proportional to the intensity of the emission $^2H_{11/2} \to {}^4I_{15/2}$,

and ϕ_{10}^{CCD} of ${}^4\mathrm{S}_{3/2} \rightarrow {}^4\mathrm{I}_{15/2}$. Now, we can use equation 3.7 for the population ratio, introducing the temperature dependence of the LIR, resulting

$$R(T) = \underbrace{\frac{\gamma_2 g_2}{\gamma_1 g_1}}_{C} \cdot \exp\left(-\frac{\Delta E}{k_B T}\right) . \tag{5.3}$$

As Suta and Meijerink[40] pointed out, when detecting light with photodetectors that measure photon flux, the C coefficient preceding the exponential factor in equation (5.3) does not depend on the photon energy. Figure 18a) shows the single-particle spectra obtained at two different temperatures, and Figure 18b) shows the LIR parameter for several temperatures, calculated as defined in equation 5.2 with the integration limits represented in 18a) (515 nm to 535 nm for $|2\rangle \rightarrow |0\rangle$, and 535 nm to 555 nm for $|1\rangle \rightarrow |0\rangle$). The dashed line in Figure 18b) is the fitting of the experimental data with equation (5.3). Observe that our thermometer works qualitatively as predicted in section 3.2: when the temperature is increased, the population of the ${}^2\mathrm{H}_{11/2}$ level increases while that from ${}^4\mathrm{S}_{3/2}$ decreases.

Figure 18 – a) Spectra of a single $NaYF_4$:Yb^{3+}/Er^{3+} particle at two different temperatures. The dashed vertical lines represent the limits of integration for the two thermally coupled bands. b) The calculated LIR for five different temperatures. The dashed line represents the Boltzmann fitting of the data. The excitation power is 25.86 kW cm^{-2} for all temperatures.

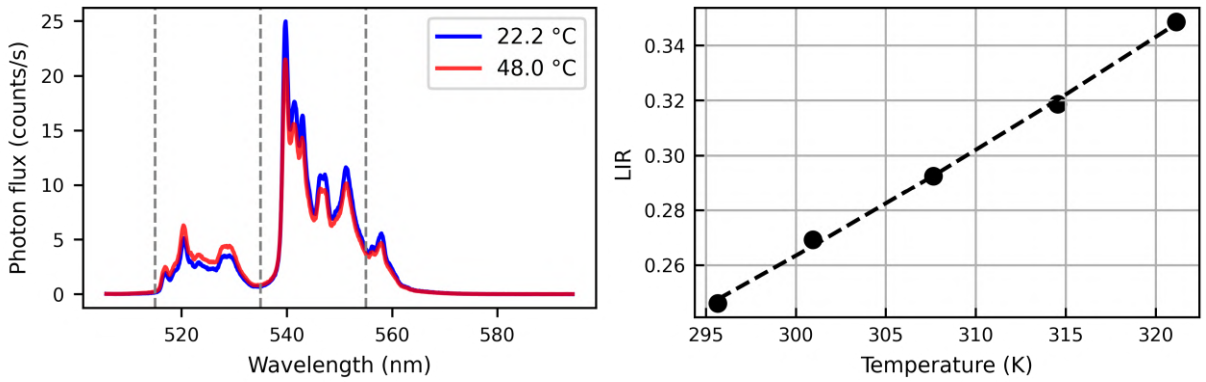

Source: The author (2022)

It is possible, therefore, to obtain the C and ΔE constants from the fitting. These are the thermometer calibration parameters. The obtained values for the studied particle are $C = 18 \pm 3$, and $\Delta E = (880 \pm 37)\,\mathrm{cm}^{-1}$. These values agree with those presented by Gonçalves et al. [15]. The slight difference is due to the improved alignment in the system for the measurements presented in this dissertation. In the mentioned work [15], we showed that the obtained values of ΔE through the LIR *vs.* T fitting do not agree with other direct

measurements, like diffuse reflectance spectra. The calibration parameters have to be treated, therefore, as *effective parameters* (ΔE_{eff} and C_{eff}). Direct diffuse reflectance measurements revealed $\Delta E_{\text{DF}} = 692\,\text{cm}^{-1}$, against our value of $\Delta E_{\text{eff}} = (880 \pm 37)\,\text{cm}^{-1}$. This is because we treated until now the thermally coupled level as non-interacting and isolated. But, this is hardly achieved in Ln^{3+} systems due to the dense energy-level structure. A more general approach can be given by including other excitation and relaxation pathways when modeling the photophysical dynamics, which is done in the next section.

An important parameter to characterize the thermometer performance is the relative sensitivity (S_r). It indicates the relative change of the thermal response per degree of temperature change [1]. Since the S_r is a relative quantity, it is well-suited to compare different thermometric techniques. The general definition is

$$S_r(T) = \frac{1}{R(T)} \frac{\partial R(T)}{\partial T} \, . \tag{5.4}$$

If the thermometric parameter follows exactly the Boltzmann prediction (Eq. (5.3)), S_r becomes

$$S_r(T) = \frac{\Delta E}{k_{\text{B}} T^2} \, . \tag{5.5}$$

The result of S_r for the thermometer calibration presented in Figure 18b) is $S_r = (1.44 \pm 0.06)\,\%\,\text{K}^{-1}$ at 297 K. This was calculated by employing equation (5.5) using the obtained ΔE_{eff} fitted.

While the relative sensitivity indicates the relative change of the thermometric parameter per unit change in temperature, the temperature uncertainty, or thermal resolution σ_T, is the smallest temperature change that can be detected by the thermometer [1]. According to equation (5.3), obtaining the temperature through the LIR analysis depends on the previous knowledge of the calibration parameters. Given that, their measurement uncertainties must be taken into account in the thermal uncertainty. In a previous work from our group, Galindo *et al.* [22, 23] showed that C_{eff} and ΔE_{eff} are correlated. The physical insight behind this result is because, as we have detailed, both constants depend simultaneously on the microparameters involved in the photophysics. Thus, they are expected to be correlated. The uncertainty propagation must be treated accordingly. It can be written as

$$\sigma_T^2 \approx \left| \frac{\partial T}{\partial (\Delta E)} \right|^2 \sigma_{\Delta E}^2 + \left| \frac{\partial T}{\partial C} \right|^2 \sigma_C^2 + 2 \cdot \frac{\partial T}{\partial (\Delta E)} \frac{\partial T}{\partial C} \sigma_{C \Delta E} + \left| \frac{\partial T}{\partial R} \right|^2 \sigma_R^2 \, , \tag{5.6}$$

where $\sigma_{\Delta E}$ and σ_C are the measurement uncertainties of the respective calibration parameters, and $\sigma_{C\Delta E}$ is the covariance of the two variables. These values are usually obtained from the calibration fitting algorithm. If $\sigma_{\Delta E}$ and σ_C are not considered, the thermal uncertainty becomes

$$\sigma_T \approx \frac{\partial T}{\partial R}\sigma_R = \frac{1}{S_R}\frac{\sigma_R}{R} \quad , \tag{5.7}$$

which is the expression usually considered in the literature [1]. σ_R is usually obtained by analyzing the histogram of numerous LIR values for a constant temperature. These measurements will be presented in section 5.4.1.

Despite the general treatment we have given until now, we can observe from our previous work [15] that the temperature calibration procedure could result in different calibration parameters for each single-particle thermometer. This is because each particle have inhomogeneities regarding its size, dopant concentration, surface defects, surface ligands, etc. Therefore, each particle has to be treated as an independent thermometer, and using the calibration from ensemble measurements can introduce systematic errors to the temperature readouts.

5.2.1 Modeling the photophysical dynamics

The simplest rate equations model involves only multiphonon transitions as the process responsible for thermalization (exchange of electronic population between the thermally coupled levels through the matrix phonons), which was calculated in equation (3.8). This made it possible to recover the Boltzmann factor for the population ratio as predicted by mechanical statistical considerations. However, in Figure 3 it is presented the energy levels diagram for the Yb^{3+}/Er^{3+} systems. It is possible to observe that there are some depopulation pathways involving the $^4S_{3/2}$ and $^2H_{11/2}$ states besides thermalization. To account for how these effects change the thermal response, we have to include such terms in the model. The main drawback is that by increasing the number of interactions in the model, we need to increase the number of coupling constants, which are hardly found in literature from direct experimental measurements. This is due first because each system (or even each individual particle) has its particularities, and second because it is experimentally hard to separate and measure only one interaction effect at a time. With this in mind, it is better to start with a simpler model before incrementing it.

In section 3.1.1, it was presented a system of rate equations to obtain the power dependence of the upconversion process. Therein, we considered the $^4\mathrm{F}_{7/2}$, $^2\mathrm{H}_{11/2}$, and $^4\mathrm{S}_{3/2}$ as a single energy level because we were interested in the overall luminescence. This is possible due to the ultrafast characteristic of the nonradiative transitions. Now, we can extend this model to separate the thermally coupled levels. Let us call them $|2a\rangle$ and $|2b\rangle$, which will represent $^4\mathrm{S}_{3/2}$ and $^2\mathrm{H}_{11/2}$, respectively. They will exchange population through multiphonon transitions, given by the rates presented in equations (2.19) and (2.20). The simplest starting point is to consider only the radiative and nonradiative relaxation/absorption. Following the same nomenclature given in the system of equations (3.2), we can write the time derivatives of the levels' population (n_i, $i = 0, 1, 2$) as

$$\dot{n_g} = -\phi_g n_g + \gamma_e n_e + k_{\mathsf{ET},1} n_e n_0 + k_{\mathsf{ET},2} n_e n_1 \ , \tag{5.8a}$$

$$\dot{n_1} = k_{\mathsf{ET},1} n_e n_0 - k_{\mathsf{ET},2} n_e n_1 - \gamma_1 n_1 \ , \tag{5.8b}$$

$$\dot{n_{2a}} = W_{\mathsf{NR}}^{\mathsf{em}}(T) n_{2b} - W_{\mathsf{NR}}^{\mathsf{abs}}(T) n_{2a} - \gamma_{2a} n_{2a} \ , \tag{5.8c}$$

$$\dot{n_{2b}} = k_{\mathsf{ET},2} n_e n_1 + W_{\mathsf{NR}}^{\mathsf{abs}}(T) n_{2a} - W_{\mathsf{NR}}^{\mathsf{em}}(T) n_{2b} - \gamma_{2b} n_{2b} \ , \tag{5.8d}$$

$$n_g + n_e = N_{\mathsf{S}} \ , \tag{5.8e}$$

$$n_0 + n_1 + n_{2a} + n_{2b} = N_{\mathsf{A}} \ . \tag{5.8f}$$

Notice that we have considered again a rapid relaxation from $^4\mathrm{F}_{7/2}$, feeding directly the $^2\mathrm{H}_{11/2}$. We can use equation (5.8c) to obtain the population ratio in steady-state ($\dot{n_{2a}} = 0$)

$$\frac{n_{2b}}{n_{2a}} = \left(\frac{W_{\mathsf{NR}}^{\mathsf{abs}}(T) + \gamma_{2a}}{W_{\mathsf{NR}}^{\mathsf{em}}(T)} \right) , \tag{5.9}$$

and the LIR will be given by

$$R(T) = \frac{\gamma_{2b} n_{2b}}{\gamma_{2a} n_{2a}} = \frac{\gamma_{2b}}{\gamma_{2a}} \left(\frac{W_{\mathsf{NR}}^{\mathsf{abs}}(T) + \gamma_{2a}}{W_{\mathsf{NR}}^{\mathsf{em}}(T)} \right) = \frac{\gamma_{2b}}{\gamma_{2a}} \left(\frac{W_{\mathsf{NR}}^{\mathsf{abs}}(T)}{W_{\mathsf{NR}}^{\mathsf{em}}(T)} + \frac{\gamma_{2a}}{W_{\mathsf{NR}}^{\mathsf{em}}(T)} \right) . \tag{5.10}$$

The first term of the right-hand side of equation (5.10) returns the Boltzmann factor (as shown in section 3.2.2). However, we have an additional term with different temperature dependence. Since $W_{\mathsf{NR}}^{\mathsf{em}}(T) \gg \gamma_{2a}$ due to the small energy difference between the thermally coupled levels, the second term is much smaller than 1. We, therefore, find the Boltzmann thermometry characteristics well suitable for such situations. However, we can proceed with

calculating the relative sensitivity in this context to gain more intuition. The relative sensitivity of the thermometric parameter obtained in equation (5.10) is calculated as

$$S_r(T) = S_r^{\mathsf{B}} + \frac{1}{R}\frac{\gamma_{2b}}{\gamma_{2a}}\frac{\partial}{\partial T}\left(\frac{\gamma_{2a}}{W_{\mathsf{NR}}^{\mathsf{em}}(T)}\right) . \tag{5.11}$$

S_r^{B} is the relative sensitivity predicted for a Boltzmann thermometer, as in equation (5.5). Let us substitute $W_{\mathsf{NR}}^{\mathsf{em}}(T)$ in (5.11) by equation (2.19) and proceed with the derivatives. We obtain

$$\begin{aligned} S_r(T) &= S_r^{\mathsf{B}} - \frac{1}{R}\frac{\gamma_{2b}}{\gamma_{2a}}\frac{\gamma_{2a}}{W_{\mathsf{NR}}^{\mathsf{em}}(T)}\left[\frac{\exp\left(\frac{-\hbar\omega_{\mathsf{eff}}}{k_{\mathsf{B}}T}\right)}{1-\exp\left(\frac{-\hbar\omega_{\mathsf{eff}}}{k_{\mathsf{B}}T}\right)}\right]\frac{p\hbar\omega_{\mathsf{eff}}}{k_{\mathsf{B}}T^2} \\ &= S_r^{\mathsf{B}} - \frac{1}{R}\frac{\gamma_{2b}}{\gamma_{2a}}\frac{\gamma_{2a}}{W_{\mathsf{NR}}^{\mathsf{em}}(T)}\left\langle n_{\mathsf{eff}}\right\rangle\frac{\Delta E}{k_{\mathsf{B}}T^2} . \end{aligned} \tag{5.12}$$

Being $\langle n_{\mathsf{eff}}\rangle > 0$, we conclude that the effect of a temperature-independent depopulation rate is to reduce the relative sensitivity. The same analysis would be valid for temperature-independent cross-relaxation phenomena. For instance, consider the cross-relaxation process ${}^4\mathsf{S}_{3/2} \rightarrow {}^4\mathsf{I}_{11/2}$; ${}^4\mathsf{I}_{15/2} \rightarrow {}^4\mathsf{I}_{11/2}$. That is, an electron at the level $|2a\rangle$ transfers its energy to another electron occupying the state $|0\rangle$, so both go to state $|1\rangle$. Also, consider that there is no energy mismatch on the referred transition (therefore does not involve the matrix phonons). The depopulation rate of state $|2a\rangle$ in this process is written as $k_{\mathsf{CR}}n_2n_0$, where k_{CR} is the cross-relaxation rate. Since we have considered the ground-state population as constant, the effect of cross-relaxation in this approximation is, therefore, also to reduce the thermometer's sensitivity. Experimental observations corroborate this assertion. For example, Suta and Meijerink[40] showed that by increasing the cross-relaxation rates, the relative sensitivity diminishes for a fixed temperature.

If we now consider a temperature-dependent depopulation from the lower thermally coupled level, as in a nonradiative decay for ${}^4\mathsf{F}_{9/2}$, the situation dramatically changes. To model this new pathway we have to include another level in the rate equations system (see Figure 19). Equation (5.8c) will therefore have another depopulation term, being written as

$$\dot{n_{2a}} = W_{\mathsf{NR},b\rightarrow a}^{\mathsf{em}}(T)n_{2b} - \left[W_{\mathsf{NR},a\rightarrow b}^{\mathsf{abs}}(T) + W_{\mathsf{NR},a\rightarrow c}^{\mathsf{em}}(T) + \gamma_{2a}\right]n_{2a} \tag{5.13}$$

where we labeled the ${}^4\mathsf{F}_{9/2}$ state as $|2c\rangle$, therefore, $W_{\mathsf{NR},b\rightarrow a}^{\mathsf{em}}(T)$ is the nonradiative decay

$^2\mathrm{H}_{11/2} \rightarrow {}^4\mathrm{S}_{3/2}$, while $W^{\mathrm{em}}_{\mathrm{NR},a\rightarrow c}(T)$ is $^4\mathrm{S}_{3/2} \rightarrow {}^4\mathrm{F}_{9/2}$. S_r now contains three terms.

$$\begin{aligned} S_r(T) &= S_r^{\mathrm{B}} + \frac{1}{R}\frac{\gamma_{2b}}{\gamma_{2a}}\frac{\partial}{\partial T}\left(\frac{\gamma_{2a}}{W^{\mathrm{em}}_{\mathrm{NR},b\rightarrow a}}\right) + \frac{1}{R}\frac{\gamma_{2b}}{\gamma_{2a}}\frac{\partial}{\partial T}\left(\frac{W^{\mathrm{em}}_{\mathrm{NR},a\rightarrow c}}{W^{\mathrm{em}}_{\mathrm{NR},b\rightarrow a}}\right) \\ &= S_r^{\mathrm{B}} - \frac{1}{R}\frac{\gamma_{2b}}{\gamma_{2a}}\frac{\gamma_{2a}}{W^{\mathrm{em}}_{\mathrm{NR}}(T)}\langle n_{\mathrm{eff}}\rangle\frac{\Delta E_{ab}}{k_{\mathrm{B}}T^2} + \frac{1}{R}\frac{\gamma_{2b}}{\gamma_{2a}}\frac{W^{\mathrm{em}}_{\mathrm{NR},a\rightarrow c}(T)}{W^{\mathrm{em}}_{\mathrm{NR},b\rightarrow a}(T)}\langle n_{\mathrm{eff}}\rangle\frac{\Delta E_{ac}-\Delta E_{ab}}{k_{\mathrm{B}}T^2}\,. \end{aligned} \tag{5.14}$$

Figure 19 – Scheme representing the population dynamics to model the luminescence thermometry in Yb^{3+}/Er^{3+} ions.

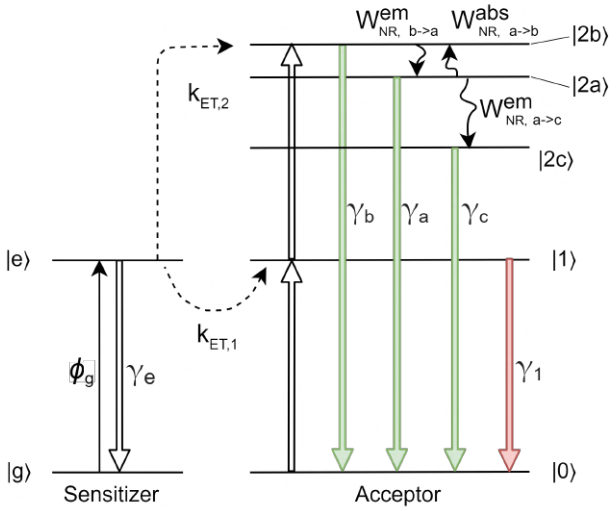

Source: The author (2022)

This result indicates that, since $\Delta E_{ac} > \Delta E_{ab}$ in Er^{3+} ions, the last term leads to an increase in the thermal sensitivity. That is, the multiphonon decay from $^4\mathrm{S}_{3/2}$ to $^4\mathrm{F}_{9/2}$ increases the thermometer's relative sensitivity. This result was obtained in a slightly different manner in our previous work [15]. Intuitively, we could think that part of the electrons in $^2\mathrm{H}_{11/2}$ 'sees' a greater energy difference to the thermally coupled level, therefore increasing the relative sensitivity.

The ratio $W^{\mathrm{em}}_{\mathrm{NR},a\rightarrow c}/W^{\mathrm{em}}_{\mathrm{NR},b\rightarrow a}$ is defined by the Energy Gap Law, given in equation (2.21). It will be written in terms of the α parameter as

$$\frac{W^{\mathrm{em}}_{\mathrm{NR},a\rightarrow c}(T)}{W^{\mathrm{em}}_{\mathrm{NR},b\rightarrow a}(T)} = \frac{g_{2c}}{g_{2a}}\exp(\alpha(\Delta E_{ac}-\Delta E_{ab}))\left[1-\exp\left(\frac{-\hbar\omega_{\mathrm{eff}}}{k_{\mathrm{B}}T}\right)\right]^{-(p_{ac}-p_{ab})}\,. \tag{5.15}$$

where p_{ab} and p_{ac} are the number of phonons involved in the process $|2b\rangle \rightarrow |2a\rangle$ and $|2a\rangle \rightarrow |2c\rangle$, respectively. Combining equations (5.14) and (5.15) we obtain an expression for the relative sensitivity of a luminescent thermometer in which the lower-lying level is

also depopulated through multiphonon processes to an adjacent level. In equation (5.14), the second term on the right-hand side can be neglected because, as we have previously stressed, the rate of nonradiative transitions between $|2a\rangle$ and $|2b\rangle$ is much higher than the radiative transition rates. Now, by knowing the thermally coupled level's 'real' energy difference of $\Delta E_{ab} = 692\,\mathrm{cm}^{-1}$ (measured by diffuse reflectance spectra, see the previous section), we can calculate $S_r^{\mathsf{B}} = 1.13\,\%\,\mathrm{K}^{-1}$ at 297 K. On the other hand, the measured S_r revealed $1.44\,\%\,\mathrm{K}^{-1}$ at the same temperature. If we attribute this difference only to the nonradiative decay of the $^4\mathrm{S}_{3/2}$ (neglecting the radiative decay rate), we write

$$\delta S_r = S_r^{\mathsf{meas}} - S_r^{\mathsf{B}} = \frac{1}{R}\frac{\gamma_{2b}}{\gamma_{2a}}\left\langle n_{\mathsf{eff}}\right\rangle \frac{\Delta E_{ac} - \Delta E_{ab}}{k_{\mathsf{B}}T^2}\frac{W_{\mathsf{NR},a\to c}^{\mathsf{em}}(T)}{W_{\mathsf{NR},b\to a}^{\mathsf{em}}(T)}\,. \tag{5.16}$$

Therefore,

$$\alpha = \frac{1}{(\Delta E_{ac} - \Delta E_{ab})}\ln\left(\delta S_r \frac{\gamma_{2a}}{\gamma_{2b}}\frac{R}{\left\langle n_{\mathsf{eff}}\right\rangle}\frac{k_{\mathsf{B}}T^2}{(\Delta E_{ac} - \Delta E_{ab})}\frac{W_{\mathsf{NR},b\to a}^{\mathsf{em}}(T)}{W_{\mathsf{NR},a\to c}^{\mathsf{em}}(T)}\right)\,. \tag{5.17}$$

Notice that all values on the right-hand side can be directly measurable. Using the matrix's effective phonon energy as $230.67\,\mathrm{cm}^{-1}$ [15, 77] (see the matrix's phonon distribution in 10c), $\gamma_{2a} = 2.399\,\mathrm{ms}^{-1}$ and $\gamma_{2b} = 0.937\,\mathrm{ms}^{-1}$ [55], $\Delta E_{ac} = 3214\,\mathrm{cm}^{-1}$ and $\Delta E_{ab} = 692\,\mathrm{cm}^{-1}$ [15], we obtain α of the energy-gap law for the $NaYF_4$: Yb^{3+}/Er^{3+} system as $\alpha = 1.75 \times 10^{-3}\,\mathrm{cm}$. This value is in agreement with that measured in a previous work of our group [15] through a similar analysis. In that case, the calculated $\ln(\mathsf{LIR})$ through a similar rate equation system was expanded up to the first order in energy and compared to the Boltzmann prediction.

The discussions presented in this section show that the photophysical dynamics influences the thermometric characteristics in Ln^{3+}-based systems. This is also studied in a previous work from our group regarding the influence of the surrounding medium in the thermometric performance of nanothermometers [22, 23]. In the following section, another thermal artifact regarding the measurement data analysis will be detailed.

5.2.2 Influence of the $^2H_{9/2} \to {}^4I_{13/2}$ transition

In Figure 18, the LIR was calculated by considering the integration interval of the lower-lying band as 535 nm to 555 nm. This is because there is an overlapping band centered in 557 nm that is not thermally coupled with $^4\mathrm{S}_{3/2}$ or $^2\mathrm{H}_{11/2}$. This band arises from the transitions $^2\mathrm{H}_{9/2} \to {}^4\mathrm{I}_{13/2}$ (as shown in Figure 3). According to the discussion provided in section

3.2.3, the $^2H_{9/2}$ state is populated by two different three-photon routes under 977 nm laser excitation, whereas the thermally coupled levels require a two-photon process. As a result, the power dependence of the 545 nm and 557 nm bands will be different. Figure 20a) shows the upconversion luminescence spectra for numerous excitation irradiances. It can be clearly seen the different power dependence of the 557 nm band, and that this band overlaps with the 545 nm band transition. This has special importance in practical applications of ratiometric thermometers because the introduction of a temperature-independent band into the integration interval of the thermally coupled level can produce temperature misreadings as we shall see as follows.

Figure 20 – a) Normalized upconversion luminescence spectrum for numerous excitation irradiances. b) Integrated band emission intensity as a function of excitation irradiance. Red squares: $^4S_{3/2} \rightarrow {}^4I_{15/2}$, blue dots: $^2H_{11/2} \rightarrow {}^4I_{15/2}$, green triangles: $^2H_{9/2} \rightarrow {}^4I_{13/2}$. The dashed lines are fittings $I = A \cdot \mathcal{P}^n$, separated at low (below 10^3 W/cm^2) and high power regime.

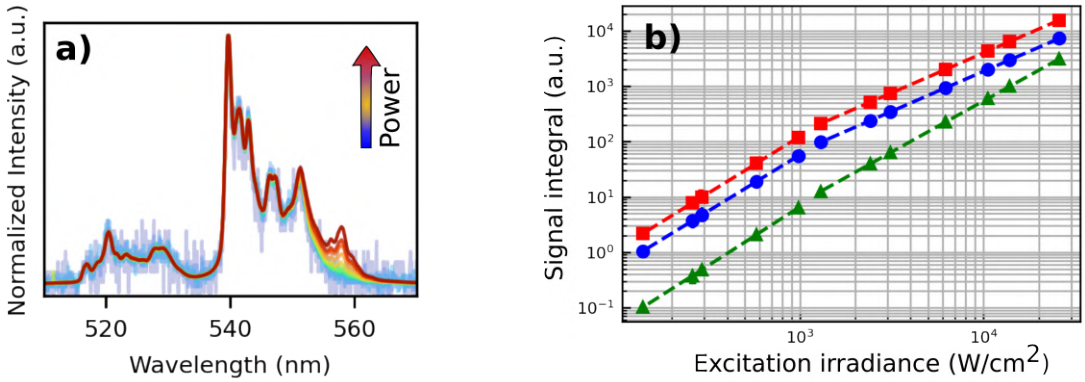

Source: The author (2022)

Figure 20b) shows the integrated intensity of the $^2H_{11/2} \rightarrow {}^4I_{15/2}$ (515 nm to 535 nm), $^4S_{3/2} \rightarrow {}^4I_{15/2}$ (535 nm to 545 nm), and $^2H_{9/2} \rightarrow {}^4I_{13/2}$ (555 nm to 570 nm). It was shown in section 3.1.1 that the power dependence of the luminescence intensity follows a saturation law. If $\mathcal{P} \ll \mathcal{P}_{sat}$, the luminescence intensity of the two-photon bands will follow $I \propto P^2$. It is possible to show, by similar arguments, that a n-photon process follows a $I \propto P^n$. We used this function to fit the data in Figure 20b) in two irradiance regimes, the obtained slopes are shown in Table 2.

Table 2 – Fitting power law slopes

Transition	Low-power regime	High-power regime
$^2H_{11/2} \rightarrow {}^4I_{15/2}$ (515 nm - 535 nm)	2.0 ± 0.1	1.44 ± 0.04
$^4S_{3/2} \rightarrow {}^4I_{15/2}$ (535 nm - 545 nm)	2.0 ± 0.1	1.44 ± 0.04
$^2H_{9/2} \rightarrow {}^4I_{13/2}$ (555 nm - 580 nm)	2.1 ± 0.1	1.84 ± 0.04

In Table 2 we see that in the higher power regime, the slope (n) of the fitted data results in 1.44 ± 0.04 for the two-photon bands, while $n = 1.84 \pm 0.04$ for the three-photon band. This shows that the photophysical dynamics involving both processes are clearly different. It is also observed that, even in the lower power regime, the slope of the three-photon band was not equal to 3. This is because i) even at the lowest excitation irradiance employed, the three-photon transition was already saturated; going below resulted in very poor signal-to-noise ratios, and ii) there is still an overlapping contribution of the two-photon band for wavelengths higher than 555 nm.

To see how this three-photon band can lead to temperature misreadings, we calibrate the thermometer either by integrating ϕ'_{10} from 535 nm to 570 nm (Figure 21), for various excitation powers, and by disregarding totally its influence, integrating ϕ_{10} only from 535 nm to 545 nm (Figure 22).

Figure 21 – a) Temperature dependence of the single particle thermometer for different excitation irradiances (legends represent the excitation irradiances in kW/cm^2) when integrating the luminescence spectrum from 515 to 535 nm for the $^2H_{11/2}$ band, and from 535 to 580 for the $^4S_{3/2}$ band (including the $^2H_{9/2} \rightarrow {}^4I_{13/2}$ transition). b) Dependency of the thermometric parameter (R) with the excitation power for different temperatures.

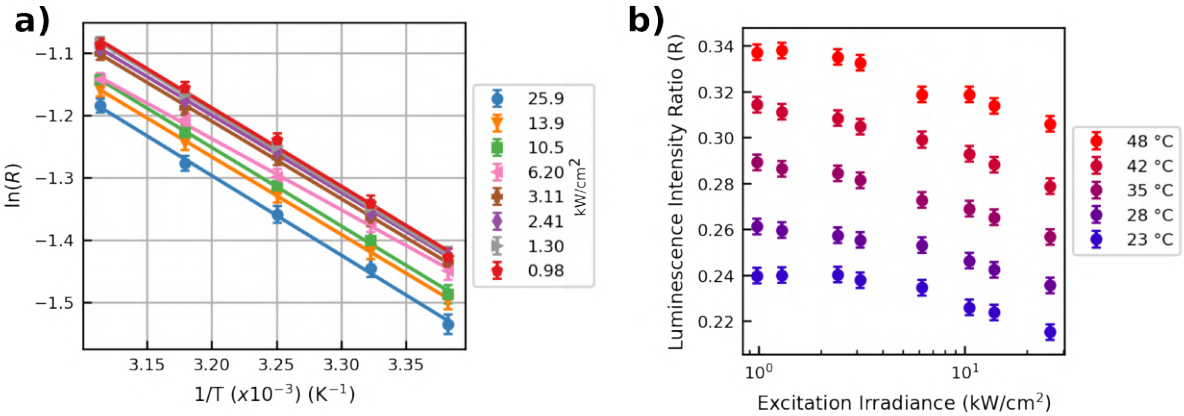

Source: The author (2022)

Indeed, in both situations, the effective prefactor constant C_{eff} in equation (5.3) will deviate from the real value because we are not properly integrating the thermally coupled bands. But

Figure 22 – Temperature dependence of the same single particle thermometer for different excitation irradiances (legends represent the excitation irradiances in kW/cm^2) when integrating the luminescence spectrum from 515 to 535 nm for the $^2H_{11/2}$ band, and from 535 to 545 for the $^4S_{3/2}$ band (excluding the $^2H_{9/2} \rightarrow {}^4I_{13/2}$ transition). b) Dependency of the thermometric parameter (R) with the excitation power for different temperatures.

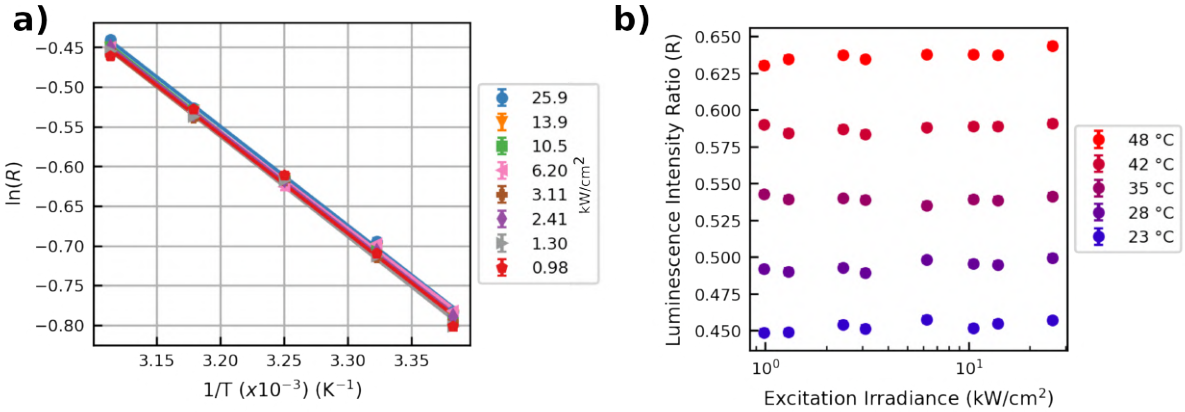

Source: The author (2022)

disregarding the three-photon process, the LIR is not expected to change with power. The detailed results are shown in Table 3 and Table 4. The thermal uncertainties are calculated based on equation (5.7), with σ_T as that obtained in Figure 27. Furthermore, notice that the integration interval defined to calculate the LIR to the analysis performed in the previous section (see Figure 18) does not completely disregard the influence of $^2H_{11/2}$, but was necessary to obtain LIR values near to the 'real' value.

Table 3 – Thermometer characteristics including the $^2H_{9/2} \rightarrow {}^4I_{13/2}$ transition in the integration of the $^4S_{3/2}$ band

	Fitted		Calculated	
Irradiance (kW/cm^2)	ΔE_{eff} ($\times 10^2$ cm^{-1})	$\ln(C_{\text{eff}})$	S_r (%/K) †	σ_T (K)
25.9	8.9 ± 0.4	2.8 ± 0.2	1.46 ± 0.07	1.3
13.9	8.6 ± 0.4	2.7 ± 0.2	1.42 ± 0.07	1.3
10.5	8.8 ± 0.4	2.8 ± 0.2	1.44 ± 0.07	1.3
6.02	7.9 ± 0.4	2.4 ± 0.2	1.31 ± 0.07	1.4
3.11	8.6 ± 0.4	2.8 ± 0.2	1.42 ± 0.06	1.2
2.41	8.6 ± 0.4	2.8 ± 0.2	1.42 ± 0.06	1.2
1.30	8.8 ± 0.4	2.9 ± 0.2	1.45 ± 0.06	1.2
0.98	8.7 ± 0.4	2.8 ± 0.2	1.44 ± 0.06	1.2

† Relative Sensitivity at 295 K.

Table 4 – Thermometer characteristics excluding the $^2H_{9/2} \rightarrow {}^4I_{13/2}$ transition in the integration of the $^4S_{3/2}$ band

	Fitted		Calculated	
Irradiance (kW/cm^2)	ΔE_{eff} ($\times 10^2$ cm^{-1})	$\ln(C_{\text{eff}})$	S_r (%/K) †	σ_T (K)
25.9	8.7 ± 0.1	3.45 ± 0.06	1.43 ± 0.02	0.4
13.9	8.6 ± 0.1	3.42 ± 0.06	1.42 ± 0.02	0.4
10.5	8.8 ± 0.1	3.47 ± 0.06	1.44 ± 0.02	0.4
6.02	8.5 ± 0.1	3.35 ± 0.06	1.40 ± 0.02	0.4
3.11	8.7 ± 0.1	3.45 ± 0.06	1.43 ± 0.02	0.4
2.41	8.7 ± 0.1	3.44 ± 0.06	1.43 ± 0.02	0.4
1.30	8.8 ± 0.1	3.49 ± 0.06	1.45 ± 0.02	0.4
0.98	8.7 ± 0.1	3.43 ± 0.06	1.43 ± 0.02	0.4

† Relative Sensitivity at 295 K.

We observe in Figure 21 that if the three-photon band is included in the integration interval, the LIR decreases with increasing power. This could erroneously be attributed to a lower temperature with increasing power, which seems counter-intuitive [95]. After completely disregarding the influence of the 557 nm band, Figure 22 shows no LIR variation with power, which is usually expected for a ratiometric quantity. However, other effects due to power can still be present. The most discussed example is self-heating. This is related to the actual increase in the sample's temperature due to a large number of phonons created during upconversion, generally due to higher-order absorption processes followed by nonradiative decay. Rühl et al.[95] showed that in $NaYF_4$: Yb^{3+}/Er^{3+} systems, the laser only begins to heat the sample when the excitation irradiances are higher than a threshold value ($> 1 \times 10^5$ W cm^{-2}). Joseph et al.[96] indeed observed such effects for bulk samples, but they show that if the particles are suspended in a liquid, the thermal response remains unchanged in the irradiation range studied because the liquid works as a thermal reservoir. In our measurements, the excitation power was not high enough to produce self-heating effects in individual particles. Besides self-heating, it has been reported spectral change due to the blackbody radiation background, especially in thermometers working with detection in the near-infrared band [54]. But this is most pronounced when the temperatures are much higher than those employed in this work [54].

5.3 Time-resolved measurements

Time-resolved measurements reveal the dynamics of the system. During excitation with a CW laser, for example, before the system reaches the steady-state, it passes through a transient state in which the population changes with time towards a constant value. Similarly, when the excitation ceases, the populations decay to zero within a finite time. Quantifying this 'decay time' is not straightforward. Since the photophysics involves multiple interacting ions, through several population/depopulation routes, the functional form of the decay curve is often complicated. Rigorously, the decay time does not depend only on intrinsic parameters such as radiative and nonradiative decays rate, but also on the energy transfer rates between the doping ions, and their collectiveness [97]. However, when the doping concentration of the sensitizer ions is relatively high, the energy migration is rapid enough so we could treat the system as all the ions participate equally in the dynamics. This raises the possibility of using average rate equations to model the photophysical dynamics [98].

It has been shown in upconverting systems that the decay curves shape changes with the doping concentration [99], size [100, 101], excitation power [102], and whether the particle is protected by a shell [99, 18]. This last one is especially relevant because it shows that surface quenching effects (energy transfer to ligand molecules, for instance) can be diminished with shell passivation thus increasing the upconversion efficiency. The decay curve of a particular energy level depends on the multiple feeding or emissions that can happen to that level. For example, in a very simplified model, Bergstrand et al.[71] have shown that the decay curve of the luminescence in a two-step upconversion scheme is described by a sum of three exponential functions. Each exponential contributes with a decay constant. Naturally, depending on the relative values between these constants, one exponential term can dominate. By considering that the energy transfer step to $^4\mathrm{F}_{7/2}$ rapidly reaches $^4\mathrm{S}_{3/2}$ because they are close in energy, the authors found that the transient regime for the population of the n_{2a} after pulsed excitation is [71]

$$\begin{aligned} n_{2a}(t) = {} & A_1 \exp\Big(-\Big(\gamma_{2a} + W^{\mathsf{em}}_{\mathsf{NR},a\to c}(T)\Big)t\Big) \\ & + A_2 \exp(-(\gamma_e + k_{\mathsf{ET},1} n_0)2t) \\ & + A_3 \exp(-(\gamma_1 + \gamma_e + k_{\mathsf{ET},1} n_0)t) \end{aligned} \tag{5.18}$$

Here the transition rates follow the labeling specified in the system of equations (5.8). A_1, A_2, and A_3 are constants that depend on the rates written in the exponential terms of

equation (5.18), and on the excited state population of the level n_{2a} in steady-state. From equation (5.18), we observe that the decay curve of the $^4S_{3/2} \rightarrow {}^4I_{15/2}$ transition depends on several constants. Obtaining all these parameters with only a decay curve is questionable due to the excessive number of experimental parameters. Also, in this model, cross-relaxation effects are disregarded. If they were to be considered the situation becomes even more intricate [103, 71].

To obtain quantitative information from decay or rising curves without having to fit multiple exponential terms, as in equation (5.18), authors may calculate the effective decay lifetime as the expectation value from the time-resolved data, defined by [98]

$$\tau = \langle t \rangle = \frac{\int_0^\infty t \cdot I(t) dt}{\int_0^\infty I(t) dt} \tag{5.19}$$

where $I(t)$ is the luminescence decay curve, being $t = 0$ the instant when the beam excitation is removed. Naturally, the upper integration limit imposes that the decay curves must be integrated up to a value where the decay curve sufficiently goes to zero. This is not often the case in luminescent time-resolved data because the photodetectors always have a background (due to spurious light, for example) that adds a constant value to the signal. This background must be subtracted first, otherwise, the effective lifetime will depend on the chosen integration limits.

In the previous section, we obtained the α parameter from the energy-gap law by comparing the theoretical predictions for the relative sensitivity with the experimental results for the decay curve of the level $|2a\rangle$. To be able to model with more precision the dynamics in such systems, we still need the energy-gap law parameter β. We could attempt to obtain this specific value from time-resolved measurements, by solving dynamically the system of rate equation and comparing it with the experimental time-resolved data. However, since the lifetime depends also on other microscopic parameters, this method depends on the reliability of these values. Fortunately, many works in the literature attempt to determine the energy-transfer rates, especially in Yb^{3+}/Er^{3+} systems. This facilitates the comparison of the obtained results. For example, Hossan et al.[104] constructed a very robust system of rate equations to model the steady-state population and the transient regime in $NaYF_4$ Yb^{3+}/Er^{3+}. They adjusted the model to fit the decay curves from numerous excited states, then obtained several parameters, such as energy-transfer rates and radiative decay rates. Furthermore, they modified the model to include surface quenching effects, then they could simulate the effect of shell passivation,

and compare it with the experimental results. Also, Fu et al.[105] present an important work regarding the determination of the microparameters in $NaYF_4$ Yb^{3+}/Er^{3+} systems. By carefully selecting the excitation wavelength and modeling the system accordingly, they could extract, level-by-level, the radiative and multiphonon nonradiative relaxation rates.

From Judd-Ofelt's theory (see section 2.4.1), it is possible to obtain the radiative transition rates, so the reminiscent free parameters in equation (5.18) are $k_{\mathsf{ET},1}$ and β ('hidden' in $W_{\mathsf{NR},a\to c}$). In order to obtain these microparameters specifically for our system, we solved the rate equations (5.8) numerically by using the classic Runge-Kutta 4th-order method [106]. This makes it possible to simulate the transient effect and compare it to the data obtained by the time-resolved measurements. The Runge-Kutta algorithm was implemented in Python programming language, and the source code can be found in Appendix A, along with the references for the used constants extracted from other works. The simulation was performed in two steps: we begin our system with population only in the ground-states of the ions. The first round of simulation includes the excitation term ($\phi_g n_g$ in equations (5.8)). We choose the simulation interval so that the system reaches the steady-state regime. Then, we perform the second round of calculations by taking out the excitation term, and by setting the initial populations as the previously obtained steady-state values. The population of the levels will decay to zero with finite time depending on the constants (see equation (5.18)). Superposing the decay experimental data for the luminescent band centered in 545 nm ($^4S_{3/2}$) with the decay curve predicted by the simulation for the level $|2a\rangle$ (Figure 23), the values of best fittings were achieved by setting $\beta = 10^7$ s^{-1}, and $k_{\mathsf{ET},1} = 2695$ s^{-1}.

The obtained values are in good agreement with that determined by other groups [97, 104, 107, 108]. It is worth mentioning that our model is still limited because it does not include effects that are known to be relevant in Yb^{3+}/Er^{3+} systems, such as back energy transfer and energy migration [98]. But it serves as a starting point for further implementations.

From equation (5.18) we still observe that factors such as the excitation power and temperature change the level's decay curve (or the effective lifetime). To show this assertion, we obtained the decay curves of the $^4S_{3/2} \rightarrow {}^4I_{15/2}$ transition for a single microcrystal by varying these parameters. Figure 24a) shows the normalized and background-corrected decay curve at room temperature for various excitation powers, ranging from 1 kW cm^{-2} to 26 kW cm^{-2}. Visually there is no apparent variation, and the curves can be well described by a mono-exponential function (straight line in a mono-log plot). However, if we calculate the effective lifetime as in equation (5.19), we could observe in Figure 24b) that τ slightly decreases with increasing

Figure 23 – a) Decay curve of the $^4S_{3/2}$ emission from a single $NaYF_4$:Yb^{3+}/Er^{3+} particle, along with the time-dependence of the excitation regime. b) The same decay curve in a monolog plot, along with the result of the computational simulations with the best-fitting parameters. The excitation power was the minimum possible ($\sim$1 kW cm^{-2}) in order to avoid higher-order contributions to the dynamics, but also keep a good signal-to-ratio.

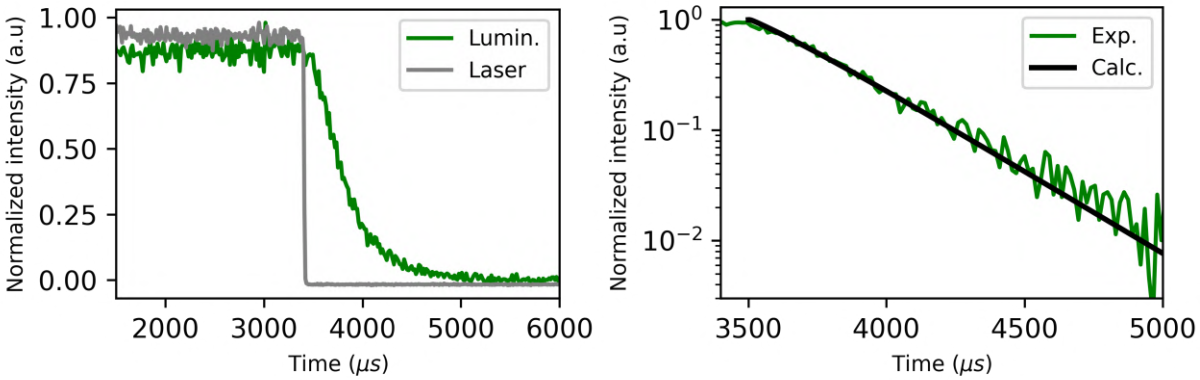

Source: The author (2022)

power. This can be caused by the change in the prefactors of different exponential components that depend on the intermediate populations in equation (5.18). Also, from Figure 24b) we see that the effect of the temperature in the measured range is not enough to produce expressive changes in the effective lifetime higher than the measurement uncertainties. For comparison, we fitted the decay curves with mono-exponential functions ($y = A\exp(-t/\tau_2)$, where A and τ_2 are the fitting parameters) and obtained another 'effective' lifetime (τ_2), shown in Figure 24c). The values obtained by the expectation values are in agreement with the fitted parameter.

Figure 24 – a) Decay curves for constant temperature and 5 different excitation irradiances. b) Effective lifetime calculated by the expectation value of the decay curve for various temperatures and powers. c) Effective lifetime from the same decay curves but now fitting the curves with a mono-exponential function. Notice that the vertical scale changes slightly but the overall trend is similar to that observed in b).

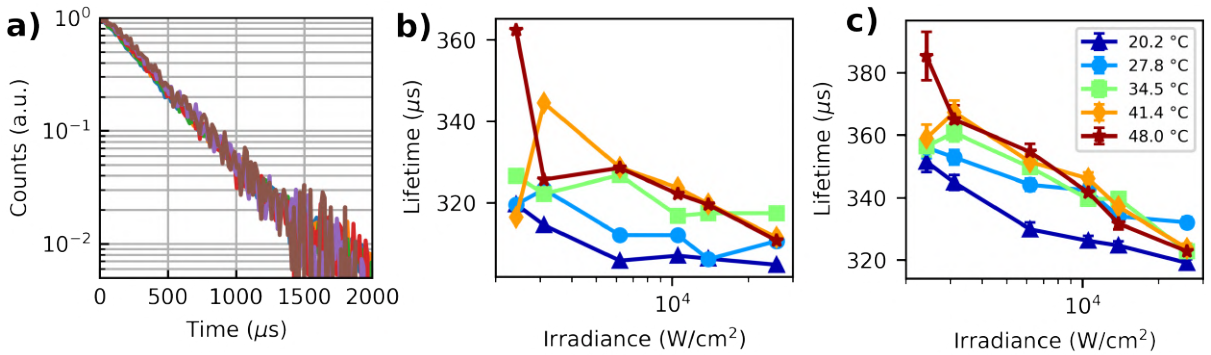

Source: The author (2022)

Therefore, since the lifetime measurements are not 'self-corrected' as the LIR, the internal dynamics seems to have a more pronounced effect. Such drawback is a limiting factor for using the decay lifetime as thermometric parameter. Besides, the recording of the decay curves may take relatively long time intervals. At the minimum excitation power employed in Figure 24, the total measurement time was about 4 minutes.

5.4 Spatial thermometer characterization

Due to the scanning system, the relative position between the sample and the laser beam can change. The single-particle thermometer characterization and time-resolved measurements detailed in the previous sections were performed in a position in which the recorded signal (APD or spectrometer) was maximum. This corresponds approximately to the beam axial direction coinciding with the particles' center. Since the particles' diameter are at least three times larger than the beam waist, at this position the laser is mostly exciting the core ions. The sample can move relatively to the laser beam so it can excite only the ions near the particle's border. This situation can be used to separate the core response from the surface response, so that, surface interactions can be studied systematically. The analysis raised in this and in the following sections make the core of a manuscript recently published by our group [81].

The Hyperspectral Imaging (HSI) technique detailed in section 4.1.1 can be used to obtain the spectra resulting from light-matter interactions at different relative sample positions. However, near the particle's border, due to the small signal-to-noise ratio on partial excitation, there can be artifacts that hinder the analysis. We can cite, for instance, the different presence of the $^2H_{9/2} \rightarrow {}^4I_{13/2}$ luminescent band, as discussed in section 5.2.2. Figure 25a) depicts the situation under total (center) and partial (border) excitation, Figure 25b) shows the obtained spectrum in each situation, and Figure 25c) shows a hyperspectral scan of a single particle where the LIR including the three-band photon (see section 5.2.2) was calculated for each pixel (integration the lower-lying band from 535 nm to 580 nm). To build the image, the pixels with an overall intensity smaller than a predefined cutoff value were set to $R = 0$, which has no temperature interpretation. These pixels are represented by gray color.

The LIR may present higher values at the particle's border if the three-photon band is naively included in the integration interval of the $^4S_{3/2}$ band (a procedure that is very common in the literature). According to the thermometer calibration shown in Figure 21 for the higher power, it seems that the temperatures at the borders of the particle (304 K) are higher than

Figure 25 – a) Schematics showing the relative position between the laser beam and the single crystal for an image's pixel at the center (left), and at the border (right). b) The normalized recorded spectra for a pixel at the center of the microparticle (blue), and at the border (red). c) Scan (5 × 5 µm, 40 × 40 pixels) with false colors representing the Luminescence Intensity Ratio including the three-photon band.

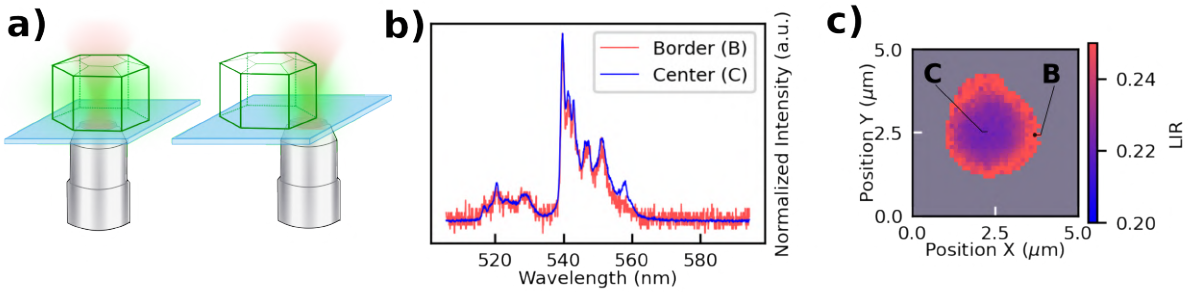

Source: The author (2022)

that closer to the center (295 K). This temperature gradient is not reasonable since the measurements were taken at room temperature after waiting for the system's thermalization. This measurement artifact is caused by the different three-photon band influence in both situations. As discussed in section 3.2.2, an n-step upconversion process depends on the presence of n nearby sensitizer ions in order to transfer their energy to an activator ion. In the full excitation scheme (with sufficient excitation power density), more ions absorb the incoming radiation, so they are more prone to make a three-step upconversion process (emission band centered at 557 nm). On the other hand, in the partial excitation scheme, fewer ions near the border absorb the radiation. They can migrate their energy to other ions throughout the particle so the local availability of ions to make the $^2H_{9/2} \rightarrow {}^4I_{13/2}$ transition decreases. Notice that, according to equation (3.3), the number of Er^{3+} ions in the excited state $^4S_{3/2}$ is proportional to n_e^2, where n_e is the excited-state population of the Yb^{3+} ions. Correspondingly, the population in $^2H_{9/2}$ will be proportional to n_e^3. In the partial excitation scheme, n_e is lower, so the probability of a three-photon process is decreased.

To completely disregard the effect of the overlapping three-photon band, one must either 1) Integrate only up to a wavelength in which the presence of this band is negligible (e.g up to 545 nm), or 2) Remove the three-photon band from the obtained spectra. The former procedure is simpler but increases the LIR uncertainty since the integration interval is lower. The latter, in its turn, requires performing other measurements to isolate the individual contributions in the overlapping region. For example, authors [109, 95] have performed direct excitation in the $^2H_{9/2}$ (with ∼405 nm excitation) and $^4F_{7/2}$ (with ∼470 nm excitation) to compare the green output spectrum in both situations. In the first case, there is the presence of the band

centered in 557 nm, whereas it is not present in the second one. They could subtract the spectra thus isolating the three-photon band contribution. In our case, the first solution (limiting the integration interval) is more easily implemented in our experimental apparatus, so it was the one employed.

5.4.1 Influence of the photodetector dark-current background

We have seen that the LIR, in principle, is a self-referenced method, but effects such as cross-relaxation and nonradiative depopulation pathways can perturb the Boltzmann equilibrium. Besides these physical pitfalls, there are also artifacts regarding the measurement process itself. Of special relevance for the thermometer spatial characterization is the CCD dark-current background.

The dark current background is present in all photodetectors in the photocounting regime (e.g. CCD arrays, APDs, PMTs). This effect is intrinsically due to the statistical nature of the carrier generation process, even if there is no incident radiation [110]. Therefore, it is highly temperature-dependent [70, 110]. Since the hyperspectral measurements have a total scan time of 10 to 20 minutes, the room temperature can vary due to the air conditioning system, so it can disturb the measurements' background during data collection. To see how the CCD background is affected by the temperature variations, we completely closed the spectrometer slit (no incoming light), then monitored the output spectrum, along with the room temperature with a thermistor, for about 1 hour. The result is presented in Figure 26.

It was observed that the room temperature varied by $\sim$0.3 °C, in 20 minutes, due to the air-conditioning on-off control system. The spectrum background followed this oscillation. This disturbance has practical importance in the LIR evaluation: by considering the dark-current background as an additional (temperature-dependent) term to equation (5.1), we write

$$R(T) = \frac{\mathcal{I}_{20}}{\mathcal{I}_{10}} = \frac{\int \mathrm{d}\lambda \left(\frac{\mathrm{d}\phi(\lambda)}{\mathrm{d}\lambda} + \theta_{DK}(T) \right)}{\int \mathrm{d}\lambda \left(\frac{\mathrm{d}\phi(\lambda)}{\mathrm{d}\lambda} + \theta_{DK}(T) \right)} \quad , \tag{5.20}$$

which is not a suitable form to directly evaluate the temperature. In equation (5.20), $\theta_{DK}(T)$ represents the average dark count rate per pixel (wavelength) per second. To avoid the temperature error due to the background during the hyperspectral imaging, we can process the data by locating a wavelength region in which there is no luminescence signal. We then calculate the average count in this region and subtract it from the spectrum. This has to be performed

Figure 26 – CCD dark-counts variation for long-time acquisitions (left axis, blue curve), along with room temperature measurement by a thermistor (right axis, red curve).

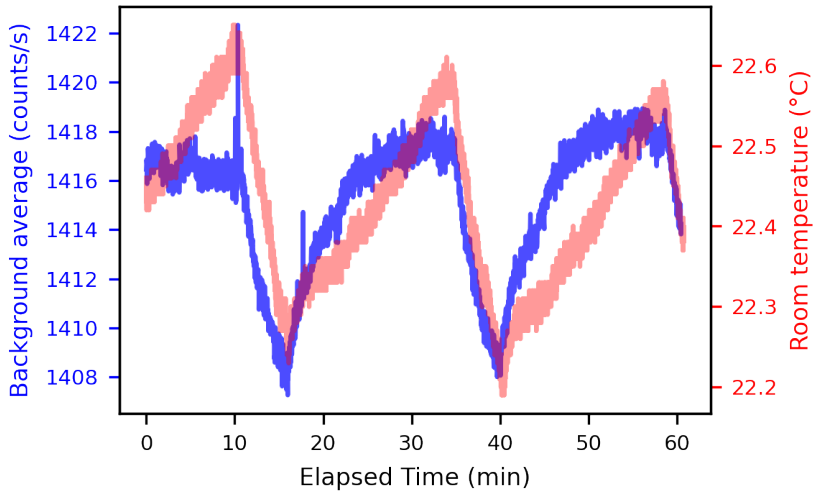

Source: The author (2022)

for each pixel separately in a hyperspectral scan.

Now, by monitoring the luminescence spectrum of a single particle for more than 1 hour, we obtain the LIR over time. Figure 27a) shows the LIR oscillations before the subtraction procedure, Figure 27b) is the histogram of the uncorrected LIR, resulting in a standard deviation of 0.0034. In figures 27c) and 27d), the spectrum background was corrected before calculating the thermometric parameter, resulting in a smaller standard deviation of 0.0022. To define the background, we used 167 points comprising the region of 580 nm to 595 nm (see Figure 18a).

5.4.2 Image Processing

Obtaining a spatially resolved thermal map from a single particle can help look for inhomogeneous interactions between the particle and the surrounding medium. For example, it could be used to observe a thermal gradient inside the particle due to an external structure. In this sense, when working with ratiometric thermometers, the measurement artifacts raised up to this point have to be properly taken into account otherwise the LIR could result in nonphysical values. After obtaining and correcting the data in a hyperspectral image, one has to calculate the LIR for each pixel. It happens that, for those pixels in which the luminescence intensity is very poor, or even non-existing, the ratiometric quantity will diverge. These points are not representative of the thermal map and blur the analysis.

To reconstruct a representative thermal map, we employed another degree of freedom in

Figure 27 – a) Apparent LIR variation (left axis, green line) along with the room temperature measured by a thermistor (right axis, red line). b) Histogram of the full data points of the uncorrected LIR (mean 0.462, standard deviation 0.0034). c) Background-corrected LIR (left axis), along with its temperature output according to a previous calibration (right axis). d) Histogram of the full data points of the LIR after background correction (mean 0.461, standard deviation 0.0022).

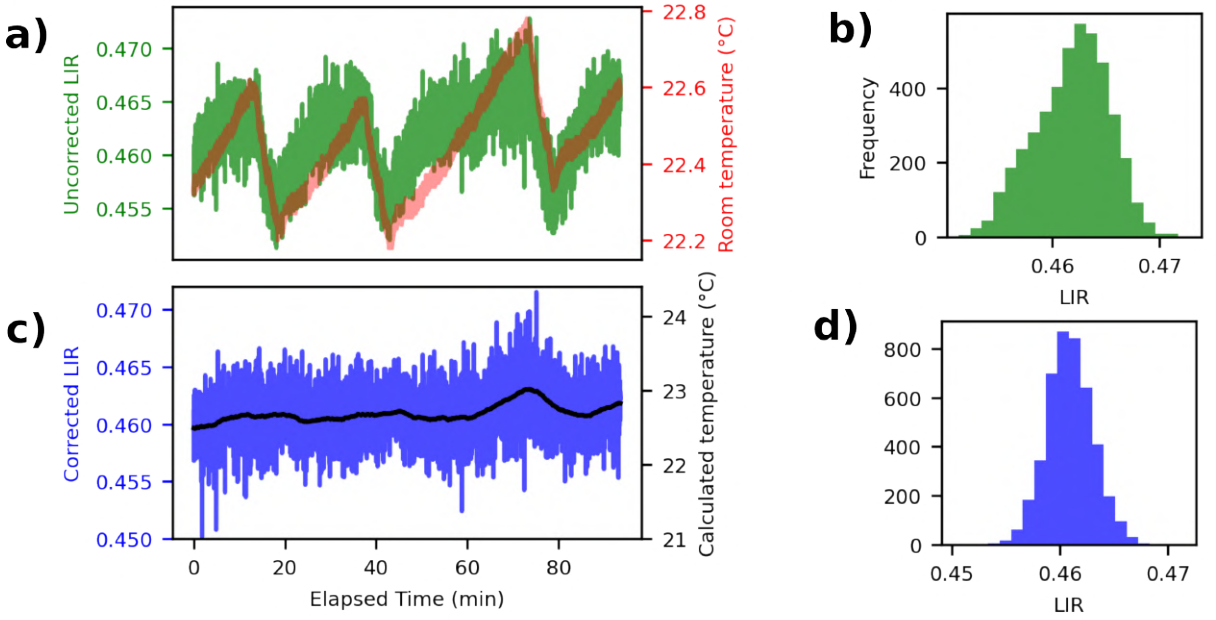

Source: The author (2022)

imaging which is pixel transparency. First, it is calculated the overall intensity for each pixel (by integrating the whole spectra). This overall luminescence image will work as our transparency mask: pixels with higher intensities will be more transparent (thus showing clearer the true pixel color), while pixels with lower intensity will fade, not showing the unrealistic values. This procedure preserves the image edges because the visualization of the noisy pixels with no information will be smoothly faded. Other authors employ more straightforward corrections, as in the recent work of Martínez et al.[111]. They used an integration threshold criterion in which they only compute the LIR for the pixel if the overall intensity is higher than a predefined value. The problem here is that this procedure depends on the chosen threshold value, and sometimes may hinder the information near the particle's border.

After obtaining the LIR for each pixel, one must use the calibration constants (in Table 4 for the corresponding power) to calculate the pixels' temperature by using equation (5.3). Figure 28 shows the step-by-step procedure to obtain a masked thermal map. Figure 28a) is the obtained temperature for all pixels, which includes the non-physical values, Figure 28b) is the overall intensity used as a transparency mask, and Figure 28c) is the output thermal map after the convolution procedure. It is worth noticing that our procedure does not change the

Figure 28 – a) Thermal map of a single microparticle obtained with LIR measurements during hyperspectral scanning and using a single previous calibration to all pixels. Colorbar from 294 to 297 K. b) Map with the overall luminescence intensity obtained integrating all spectral bands in the green region. Amplitude-normalized colorbar. c) Result of the thermal map using b) as the transparency mask. d) Cross-section of the thermal map along the dashed black curve in c). The dashed vertical lines mark the FWHM.

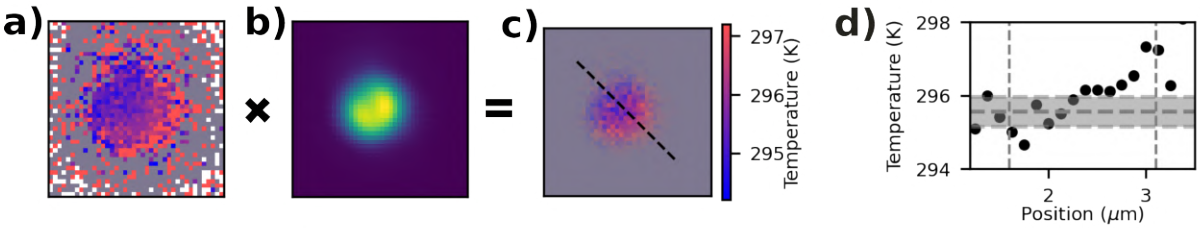

Source: The author (2022)

pixel's LIR value (which is unacceptable since it gives information about the temperature) but uses the pixel's transparency as a filter.

In Figure 28c) we can see that the transparency-mask procedure results in a cleaner thermal map. However, it still can be observed a thermal gradient inside the single-particle thermometer, which is better shown in the cross-section in Figure 28d). This internal temperature variation, again, is not reasonable since the particles are in thermal equilibrium with the environment. This spatial dependence can be caused by crystal inhomogeneities [112], or by some excitation artifacts, like deviations from the Airy disk spatial profile caused by misalignment, beam imperfections, or scattering at the particle's surface [81].

The beam spatial inhomogeneity indeed seems to be present in our experiments. According to section 4.1, the spatial profile of the focused laser beam is represented by an Airy function. This idealized situation relies mainly on the approximation that the laser beam enters the objective lens with planar wavefronts with propagation direction parallel to the optical axis. However, in real-world implementation, effects due to misalignments, beam imperfection, scattering, or optical aberrations can change the output spatial profile. Therefore, the laser can be exciting ions at other spectral positions than that predicted in the ideal situation. For example, Figure 29 shows the overall luminescence intensity obtained through hyperspectral imaging of four different single-particles. They present the same luminescence spatial profile thus indicating that this effect is more related to the excitation inhomogeneity than to the particle's inhomogeneity itself. This artifact limits the reliability of hyperspectral images. However, after the correction of the three-photon band overlapping with the thermally coupled bands, the thermometric parameter (LIR) should not be power dependent (as shown in Figure

Figure 29 – Overall intensity of the green emissions for four different single particles (named PTC01 to PTC04), obtained through hyperspectral scanning (40×40 pixels), in which the spectra are integrated from 515 nm to 580 nm. The axes of the images are given in micrometers. The plots represent a cross-section of the image at the position $y = 2.5\ \mu m$, given in $10^3 \times$ counts s^{-1}

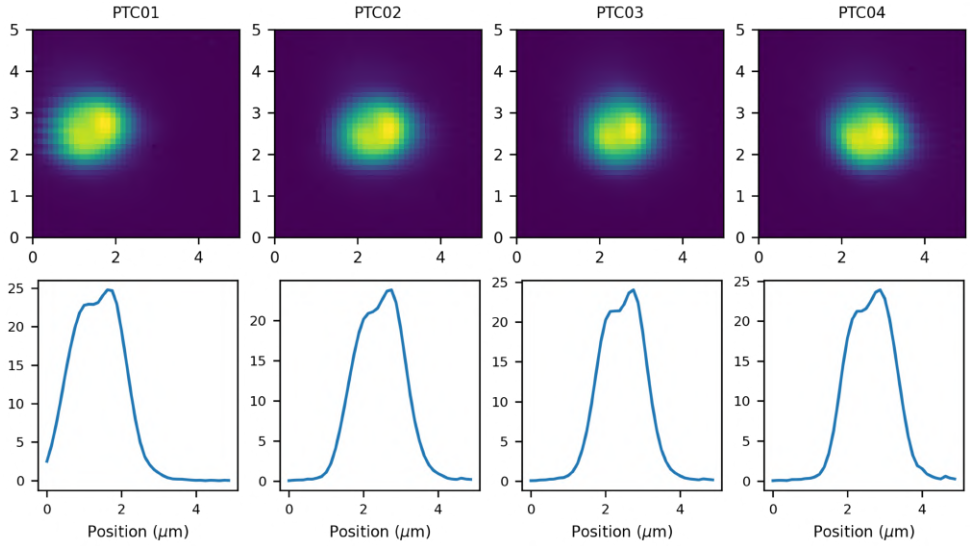

Source: The author (2022)

22). Therefore, the inhomogeneous excitation profile should not be a problem in this sense. We recognize that further investigations must be conducted to understand the origin of this spatial inhomogeneity.

In the case of the thermal map presented in Figure 28c), all the pixels' temperatures were calculated by using a single thermal parameter. However, if different pixels have different thermal responses, it should be attributed to a difference in the thermal parameters. To correct this apparent gradient, we can rely on a hyperspectral thermal calibration for each pixel. First, we obtain the hyperspectral data and calculate the LIR for different temperatures. Then, for a specific pixel position for all temperature scans, we can fit a LIR-*vs.*-Temperature curve with the Boltzmann function (Equation (5.3)). We therefore will obtain the C_{eff} and ΔE_{eff} parameters for each pixel in the image (spatially resolved inside the single particle). The results are shown in Figure 30.

We can now have the thermal map of a particular hyperspectral scan by calculating each pixel's temperature by using the respective calibration parameters. A representation of the hyperspectral calibration procedure is presented in Figure 31a), the corrected thermal map at room temperature in Figure 31b), and a cross-section is shown in Figure 31c). We observe that after the correction procedure, the temperature fits the uncertainty range, and there is no temperature gradient inside the single particle.

Figure 30 – Spatial characterization of a single particle thermometer. a) Image showing the spatial distribution of the fitted ΔE parameter. Horizontal dashed lines represent the cross-section positions showed in b) plot. b) ΔE along two cross-sections, red triangles for the cross-section $y = 3.00\ \mu m$, and blue circles for $y = 2.12\ \mu m$. The dashed vertical lines represent the FWHM of the particle's intensity image. c) Histogram of the spatial α values weighted by the overall intensity. This is necessary to compute only the values where there is sufficient luminescent signal. d) $\ln(C)$ parameter obtained from the same fitting. Horizontal dashed lines represent the cross-section positions showed in e) plot. e) $\ln(C)$ along two cross-sections, navy-blue triangles for the cross-section $y = 3.00\ \mu m$, and green circles for $y = 2.12\ \mu m$. The dashed vertical lines represent the FWHM of the particle's intensity image. f) Histogram of the spatial β values weighted by the overall intensity. g), h) and i) refer to the same spatial analysis for the relative sensitivity at 295 K. The mean value is 1.33 % K^{-1}, with a standard deviation of 0.06 % K^{-1}.

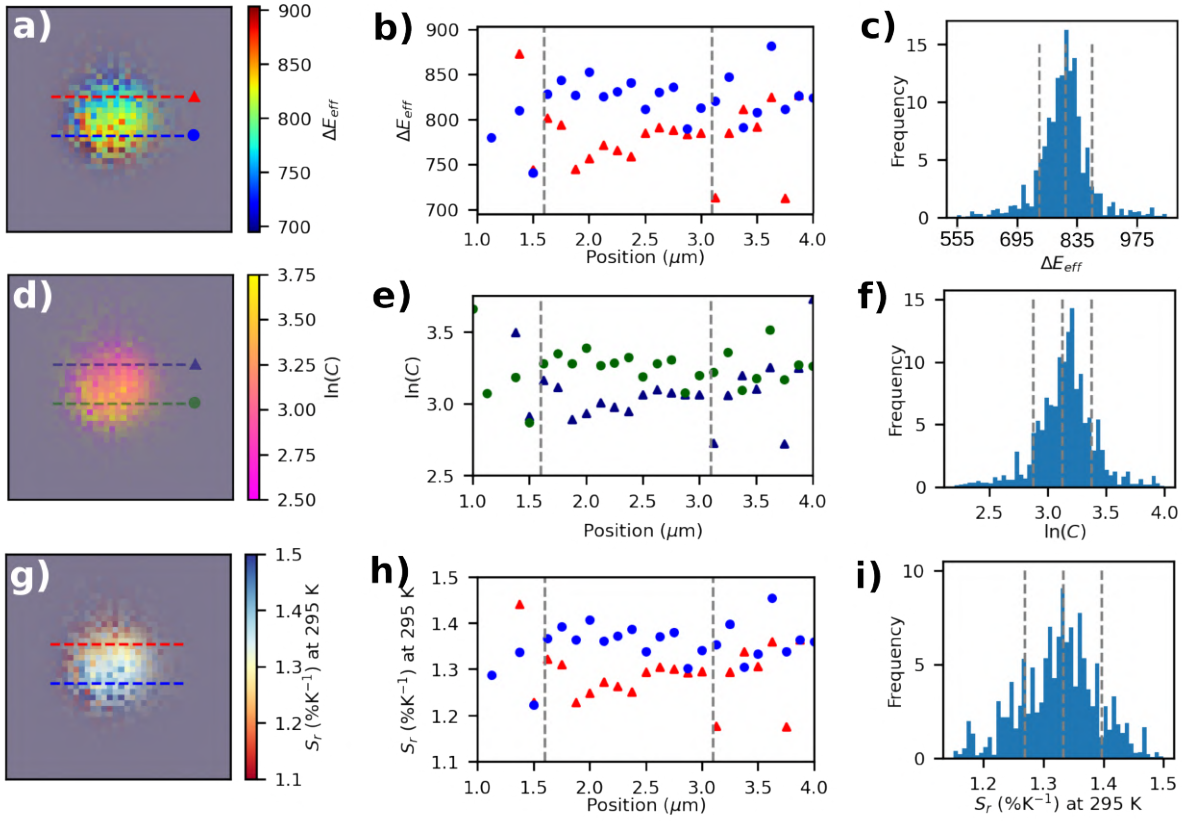

Source: The author (2022)

Figure 31 – a) Representation of multiple LIR maps at different temperatures obtained through hyperspectral scans, ranging from 295 K to 321 K. g) Corrected thermal map when the thermometer's calibration parameters are obtained for each pixel. h) Cross-section of the corrected thermal map in g) (horizontally along the center of the scan).

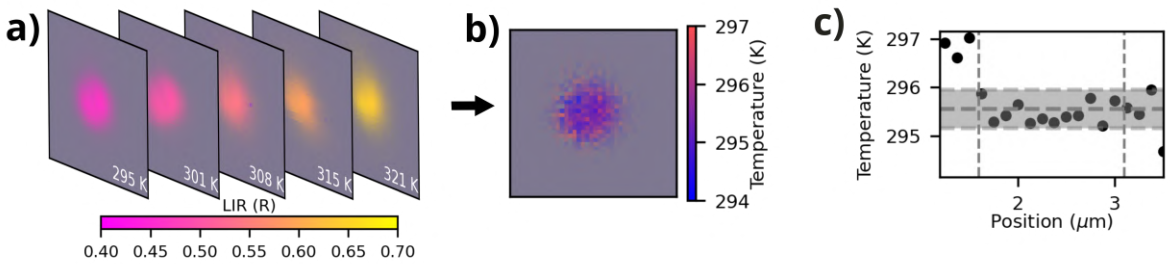

Source: The author (2022)

6 CONCLUSIONS AND PERSPECTIVES

There is an increasing interest in thermometry at the micro and nanoscale from a broad spectrum of research fields. Deeply understanding the internal and external factors affecting the temperature readouts in lanthanoid-doped single-particle thermometers is crucial for sensor reliability. In this work, we first characterized experimentally single particles of $NaYF_4$: Yb^{3+}/Er^{3+} for thermometry applications through an optical microscope system. It was obtained a feasible thermometer in the temperature range of 22 °C to 50 °C working by the frequency upconversion phenomena. The codoped system absorbs the laser radiation at 977 nm and emits the thermally coupled bands centered at 525 nm and 545 nm. By calibrating the thermometer for known temperatures, it was obtained a thermal sensitivity of $S_r = (1.44 \pm 0.06)\,\% \,K^{-1}$ and a resolution of 0.4 K. It was noticed that this thermal sensitivity is higher than that predicted by the energy separation of the thermally coupled levels by diffuse reflectance measurements. Therefore, we set a system of rate equations and studied theoretically possible physical effects that can change the thermal sensitivity. We showed that a temperature-independent depopulation route decreases the relative sensitivity. Conversely, if this process is phonon-assisted, S_r tends to increase, which could be related to our case. From the theoretical analysis, it was possible to predict microscopic parameters related to the system. We obtained the α value of the Energy-gap Law as $\alpha = 1.75 \times 10^{-3}$ cm, which is in excellent agreement with other values reported in the literature. Also, time-resolved measurements allow us to compare the luminescence decay curves with that predicted by solving the dynamical system of rate equations computationally. From this, we could also extract the β value of the Energy-gap Law as $\beta = 10^7$ s^{-1}, which is also in agreement with other works.

Furthermore, to separate the luminescent emissions of the core ions inside a single particle from the surface ones, we propose and built a hyperspectral imaging system. It works jointly with the sample-scanning inverted optical microscope and records a spectrum for each pixel, allowing to resolve spatially the thermal response of the single-particle. However, in this measurement scheme, some experimental artifacts mislead the corrected thermal analysis. The main drawback regards the influence of a temperature-independent three-photon band overlapping with the thermally coupled levels. This band brings a counter-intuitive power dependence to the temperature readouts and is especially relevant in hyperspectral images. The other identified artifact was the photodetector dark-current background that changes with the

room temperature oscillations. This also brings an additional non-physical thermal gradient to the single-particle temperature map. At last, it is possible to observe a spatial variation of the thermometric parameters inside the single particle. Although the origin of this inhomogeneity is not completely clear, we propose a method to process the obtained images and further correct the data by performing a pixel-by-pixel thermal calibration.

It is worth noticing that the presented measurement artifacts are mostly effective in lanthanoid-doped single-particle thermometers, working truly in micro and nano spatial scales. The results presented in this dissertation may enable tailoring the relative sensitivity by engineering the photophysical processes through tuning characteristics such as the multi-doping concentration, core-shell structures, and selected surface ligands. Also, single-particle hyperspectral imaging can help to study more clearly the energy-transfer effects through the particle's surface, or the spatially-dependent emission of hybrid and anisotropic single particles.

REFERENCES

1 BRITES, C.; MILLÁN, A.; CARLOS, L. Chapter 281 - lanthanides in luminescent thermometry. In: BÜNZLI, J.-C.; PECHARSKY, V. K. (Ed.). *Including Actinides*. North Holland: Elsevier, 2016, (Handbook on the Physics and Chemistry of Rare Earths, v. 49). p. 339–427.

2 BRITES, C. D. S.; BALABHADRA, S.; CARLOS, L. D. Lanthanide-based thermometers: At the cutting-edge of luminescence thermometry. *Advanced Optical Materials*, v. 7, n. 5, p. 1801239, 2019.

3 ZHOU, J. et al. Advances and challenges for fluorescence nanothermometry. *Nature Methods*, v. 17, p. 967–980, 2020.

4 BRITES, C. D. S. et al. Thermometry at the nanoscale. *Nanoscale*, v. 4, p. 4799–4829, 2012.

5 GONG, Z. et al. Upconversion nanoparticle decorated spider silks as single-cell thermometers. *Nano Letters*, v. 21, p. 1469–1476, 2021.

6 YOO, T. et al. The real-time monitoring of drug reaction in hela cancer cell using temperature/impedance integrated biosensors. *Sensors and Actuators B: Chemical*, v. 291, p. 17–24, 2019.

7 AIGOUY, L. et al. Scanning thermal imaging of microelectronic circuits with a fluorescent nanoprobe. *Applied Physics Letters*, v. 87, n. 18, p. 184105, 2005.

8 TESSIER, G. et al. High resolution thermal imaging inside integrated circuits. *Sensor Review*, v. 27, p. 291–297, 2007.

9 ROSS, D.; GAITAN, M.; LOCASCIO, L. E. Temperature measurement in microfluidic systems using a temperature-dependent fluorescent dye. *Analytical Chemistry*, v. 73, n. 17, p. 4117–4123, 2001.

10 MICHALSKI, L.; ECKERSDORF K. KUCHARSKI, J.; MCGHEE, J. *Temperature Measurement*. 2. ed. Chinchester: John Wiley & Sons, 2001. ISBN 978-0-470-84613-1.

11 DONG, H.; SUN, L.-D.; YAN, C.-H. Upconversion emission studies of single particles. *Nano Today*, v. 35, p. 100956, 2020.

12 NIRMAL, M. et al. Fluorescence intermittency in single cadmium selenide nanocrystals. *Nature*, v. 383, p. 802–804, 1996.

13 YI, G. et al. Synthesis, characterization, and biological application of size-controlled nanocrystalline $NaYF_4$:Yb,Er infrared-to-visible up-conversion phosphors. *Nano Letters*, v. 4, n. 11, p. 2191–2196, 2004.

14 RUNOWSKI, M. et al. Luminescent nanothermometer operating at very high temperature - sensing up to 1000 k with upconverting nanoparticles (Yb^{3+}/Tm^{3+}). *ACS Applied Materials & Interfaces*, v. 12, n. 39, p. 43933–43941, 2020.

15 GONÇALVES, I. et al. Phonon-assisted NIR-to-visible upconversion in single β-$NaYF_4$ microcrystals codoped with Er^{3+} and Yb^{3+} for microthermometry applications: Experiment and theory. *Journal of Luminescence*, v. 231, p. 117801, 2021.

16 KRAFT, M. et al. Particle-size-dependent upconversion luminescence of $NaYF_4$: Yb, Er nanoparticles in organic solvents and water at different excitation power densities. *Nano Research*, v. 11, p. 6360–6374, 2018.

17 SCHIETINGER, S. et al. Observation of size dependence in multicolor upconversion in single Yb^{3+}, Er^{3+} codoped $NaYF_4$ nanocrystals. *Nano Letters*, v. 9, n. 6, p. 2477–2481, 2009.

18 RABOUW, F. T. et al. Quenching pathways in $NaYF_4$:Er^{3+},Yb^{3+} upconversion nanocrystals. *ACS Nano*, v. 12, n. 5, p. 4812–4823, 2018.

19 LI, R. et al. The effect of surface-capping oleic acid on the optical properties of lanthanide-doped nanocrystals. *Nanoscale*, v. 13, p. 12494–12504, 2021.

20 RODRÍGUEZ-SEVILLA, P. et al. Assessing single upconverting nanoparticle luminescence by optical tweezers. *Nano Letters*, v. 15, n. 8, p. 5068–5074, 2015.

21 ZHOU, X. et al. Interface-dependent radiative lifetimes of yb^{3+}, er^{3+} co-doped single $nayf_4$ upconversion nanowires. *ACS Applied Materials & Interfaces*, v. 11, n. 25, p. 22817–22823, 2019.

22 GALINDO, J. A. O. et al. Influence of the surrounding medium on the luminescence-based thermometric properties of single Yb^{3+}/Er^{3+} codoped yttria nanocrystals. *Nanoscale Advances*, v. 3, p. 6231–6241, 2021.

23 GALINDO, J. A. O. et al. Correction: Influence of the surrounding medium on the luminescence-based thermometric properties of single Yb^{3+}/Er^{3+} codoped yttria nanocrystals. *Nanoscale Advances*, v. 3, p. 7007–7007, 2021.

24 HUANG, C. *Rare Earth Coordination Chemistry: Fundamentals and Applications*. Singapore: John Wiley & Sons, 2010. ISBN 978-0-470-82485-6.

25 CONNELLY, N. G. et al. (Ed.). *Nomenclature of Inorganic Chemistry*: IUPAC recommendations. Norfolk: The Royal Society of Chemistry, 2005. ISBN 978-0-854-04438-2.

26 BEAUDRY, B.; GSCHNEIDNER, K. Chapter 2: Preparation and basic properties of the rare earth metals. In: *Metals*. North Holland: Elsevier, 1978, (Handbook on the Physics and Chemistry of Rare Earths). p. 173–232. ISBN 978-0-128-21113-7.

27 BRIK, M. G.; MA, C. *Theoretical Spectroscopy of Transition Metal and Rare Earth Ions*: From free state to crystal field. Singapore: Jenny Stanford Publishing, 2020. ISBN 978-9-814-80056-3.

28 WALSH, B. M. Judd-ofelt theory: principles and practices. In: BARTOLO, B. D.; FORTE, O. (Ed.). *Advances in Spectroscopy for Lasers and Sensing*. Dordrecht: Springer Netherlands, 2006. p. 403–433. ISBN 978-1-402-04789-3.

29 JUDD, B. R. Optical absorption intensities of rare-earth ions. *Physical Review*, v. 127, p. 750–761, 1962.

30 OFELT, G. S. Intensities of crystal spectra of rare-earth ions. *The Journal of Chemical Physics*, v. 37, n. 3, p. 511–520, 1962.

31 BREHM, J.; MULLIN, W. *Introduction to the Structure of Matter: A Course in Modern Physics*. New York: John Wiley & Sons, 1989. ISBN 978-0-471-61273-5.

32 CASPARY, R. *Applied Rare-Earth Spectroscopy for Fiber Laser Optimization*. (PhD Thesis) — Technischen Universität Braunschweig, Aachen, Germany, 2001.

33 FILHO, P. C. S.; LIMA, J. F.; SERRA, O. From lighting to photoprotection: Fundamentals and applications of rare earth materials. *Journal of the Brazilian Chemical Society*, v. 26, n. 12, p. 2471–2495, 2015.

34 SOLÉ, J. G.; JAQUE, B. D. *Group Theory and Spectroscopy*. New Jersey: John Wiley & Sons, 2005. ISBN 978-0-470-01604-6.

35 WYBOURNE, B. G. *Spectroscopic Properties of Rare Earths*. New York: John Wiley & Sons, 1965. ISBN 978-0-470-96507-8.

36 SAKURAI, J. J.; NAPOLITANO, J. *Modern Quantum Mechanics*. 2. ed. New York: Cambridge University Press, 2019. ISBN 978-0-805-38291-4.

37 KITTEL, C. *Introduction to Solid State Physics*. 8. ed. New York, NY: John Wiley & Sons, 2004. ISBN 978-0-471-41526-8.

38 PUKHOV, K. K.; SAKUN, V. P. Theory of nonradiative multiphonon transitions in impurity centers with extremely weak electron-phonon coupling. *Physica Status Solidi (B)*, v. 95, n. 2, p. 391–402, 1979.

39 LAYNE, C. B.; LOWDERMILK, W. H.; WEBER, M. J. Multiphonon relaxation of rare-earth ions in oxide glasses. *Physical Review B*, v. 16, n. 1, p. 10–20, 1977.

40 SUTA, M.; MEIJERINK, A. A theoretical framework for ratiometric single ion luminescent thermometers—thermodynamic and kinetic guidelines for optimized performance. *Advanced Theory and Simulations*, v. 3, n. 12, p. 2000176, 2020.

41 YU, D.; BALLATO, J.; RIMAN, R. E. Temperature-dependence of multiphonon relaxation of rare-earth ions in solid-state hosts. *The Journal of Physical Chemistry C*, v. 120, n. 18, p. 9958–9964, 2016.

42 MENEZES, L. de S.; ARAÚJO, C. B. de. Optically detected thermal effects in rare-earth doped materials for host characterization, thermometric devices, nanothermometry and biothermometry. *Journal of the Brazilian Chemical Society*, v. 26, n. 12, p. 2405–2417, 2015.

43 AUZEL, F. Upconversion and anti-stokes processes with f and d ions in solids. *Chemical Reviews*, v. 104, n. 1, p. 139–174, 2004.

44 ANSARI, A. A.; MUTHUMAREESWARAN, M.; LV, R. Coordination chemistry of the host matrices with dopant luminescent Ln^{3+} ion and their impact on luminescent properties. *Coordination Chemistry Reviews*, v. 466, p. 214584, 2022.

45 HUANG, F. et al. Origin of near to middle infrared luminescence and energy transfer process of Er^{3+}/Yb^{3+} co-doped fluorotellurite glasses under different excitations. *Scientific Reports*, v. 5, p. 8233, 2015.

46 SONTAKKE, A. D. et al. Efficient non-resonant energy transfer in Nd^{3+}-Yb^{3+} codoped Ba-Al-metaphosphate glasses. *The Journal of the Optical Society of America B*, v. 27, n. 12, p. 2750–2758, 2010.

47 JAQUE, D. et al. $Nd^{3+} \rightarrow Yb^{3+}$ energy transfer in the $YAl_3(BO_3)_4$ nonlinear laser crystal. *Physical Review B*, v. 68, p. 035118, 2003.

48 DING, M.; XU, M.; CHEN, D. A new non-contact self-calibrated optical thermometer based on $Ce^{3+} \rightarrow Tb^{3+} \rightarrow Eu^{3+}$ energy transfer process. *Journal of Alloys and Compounds*, v. 713, p. 236–247, 2017.

49 POLLNAU, M. et al. Power dependence of upconversion luminescence in lanthanide and transition-metal-ion systems. *Physical Review B*, v. 61, p. 3337–3346, 2000.

50 SUYVER, J. F. et al. Anomalous power dependence of sensitized upconversion luminescence. *Physical Review B*, v. 71, p. 125123, 2005.

51 ZUO, J. et al. Precisely tailoring upconversion dynamics via energy migration in core–shell nanostructures. *Angewandte Chemie International Edition*, v. 57, n. 12, p. 3054–3058, 2018.

52 CALLEN, H. *Thermodynamics and an Introduction to Thermostatistics*. 2. ed. New York: John Wiley & Sons, 1985. ISBN 978-0-471-86256-7.

53 PAYNE, S. A.; BIBEAU, C. Picosecond nonradiative processes in neodymium-doped crystals and glasses: Mechanism for the energy gap law. *Journal of Luminescence*, v. 79, n. 3, p. 143–159, 1998.

54 SUTA, M. et al. Making Nd^{3+} a sensitive luminescent thermometer for physiological temperatures - an account of pitfalls in boltzmann thermometry. *Nanomaterials*, v. 10, n. 3, 2020.

55 YAO, G. et al. Calculation of Judd-Ofelt parameters for Er^{3+} in β-$NaYF_4$: Yb^{3+}, Er^{3+} from emission intensity ratios and diffuse reflectance spectra. *Journal of Luminescence*, v. 160, p. 276–281, 2015.

56 GARCÍA-FLORES, A. F. et al. Crystal-field effects in Er^{3+}- and Yb^{3+}-doped hexagonal $NaYF_4$ nanoparticles. *Physical Review B*, v. 96, p. 165430, 2017.

57 CHO, Y. et al. Spectral evidence for multi-pathway contribution to the upconversion pathway in $NaYF_4$:Yb^{3+},Er^{3+} phosphors. *Physical Chemistry Chemical Physics*, v. 19, p. 7326–7332, 2017.

58 BARIDE, A.; MAY, P. S.; BERRY, M. T. Cross-relaxation from $Er^{3+}(^2H_{11/2}, ^4S_{3/2})$ and $Er^{3+}(^2H_{9/2})$ in β-$NaYF_4$:Yb,Er and implications for modeling upconversion dynamics. *The Journal of Physical Chemistry C*, v. 124, n. 3, p. 2193–2201, 2020.

59 BERRY, M. T.; MAY, P. S. Disputed mechanism for NIR-to-red upconversion luminescence in $NaYF_4$:Yb^{3+},Er^{3+}. *The Journal of Physical Chemistry A*, v. 119, n. 38, p. 9805–9811, 2015.

60 ZHANG, J. et al. Observation of efficient population of the red-emitting state from the green state by non-multiphonon relaxation in the Er^{3+}-Yb^{3+} system. *Light: Science & Applications*, v. 4, p. 239, 2015.

61 HECHT, E. *Optics*. 5. ed. Harlow: Pearson Education, 2017. ISBN 978-0-133-97722-6.

62 NOVOTNY, L.; HECHT, B. *Principles of Nano-Optics*. 2. ed. Cambridge: Cambridge University Press, 2012. ISBN 978-1-139-45205-2.

63 HUANG, Y. et al. Hyperspectral imaging for identification of an invasive plant *mikania micrantha* kunth. *Frontiers in Plant Science*, v. 12, 2021.

64 HUANG, H.; LIU, L.; NGADI, M. O. Recent developments in hyperspectral imaging for assessment of food quality and safety. *Sensors*, v. 14, n. 4, p. 7248–7276, 2014.

65 KHAN, M. J. et al. Modern trends in hyperspectral image analysis: A review. *IEEE Access*, v. 6, p. 14118–14129, 2018.

66 WANG, Y. W. et al. Multiplexed optical imaging of tumor-directed nanoparticles: A review of imaging systems and approaches. *Nanotheranostics*, v. 1, p. 369–388, 2017.

67 DONG, X. et al. A review of hyperspectral imaging for nanoscale materials research. *Applied Spectroscopy Reviews*, v. 54, n. 4, p. 285–305, 2019.

68 GONÇALVES, I. M. *Termometria por conversão ascendente de energia em micro-cristais individuais de $NaYF_4$ codopados com Yb^{3+} e Er^{3+}*. (Master's thesis) — Universidade Federal de Pernambuco, Recife, Pernambuco, 2019. In Portuguese.

69 BECKER, W. Fluorescence lifetime imaging by multi-dimensional time correlated single photon counting. *Medical Photonics*, v. 27, p. 41–61, 2015.

70 EISAMAN, M. D. et al. Invited review article: Single-photon sources and detectors. *Rev. Sci. Instrum.*, v. 82, n. 7, p. 071101, 2011.

71 BERGSTRAND, J. et al. On the decay time of upconversion luminescence. *Nanoscale*, The Royal Society of Chemistry, v. 11, p. 4959–4969, 2019.

72 WANG, M.; HU, C.; SU, Q. Luminescent lifetime regulation of lanthanide-doped nanoparticles for biosensing. *Biosensors*, v. 12, n. 2, 2022.

73 BECKER, W. *Advanced Time-Correlated Single Photon Counting Techniques*. 1. ed. Heidelberg: Springer Berlin, 2005. ISBN 978-3-540-26047-9.

74 SÁNCHEZ, E. D. C. et al. Microcontroller-based magnetometer using a single nitrogen-vacancy defect in a nanodiamond. *AIP Advances*, v. 10, n. 2, p. 025323, 2020.

75 KWON, S. G.; HYEON, T. Formation mechanisms of uniform nanocrystals via hot-injection and heat-up methods. *Small*, v. 7, n. 19, p. 2685–2702, 2011.

76 GATES-RECTOR, S.; BLANTON, T. The powder diffraction file: a quality materials characterization database. *Powder Diffraction*, Cambridge University Press, v. 34, n. 4, p. 352–360, 2019.

77 RENERO-LECUNA, C. et al. Origin of the high upconversion green luminescence efficiency in β-$NaYF_4$:2%Er^{3+},20%Yb^{3+}. *Chemistry of Materials*, v. 23, n. 15, p. 3442–3448, 2011.

78 WEI, Y. et al. Synthesis and characterization of efficient near-infrared upconversion Yb and Tm codoped $NaYF_4$ nanocrystal reporter. *Journal of Alloys and Compounds*, v. 427, n. 1, p. 333–340, 2007.

79 PANOV, N. et al. Hyperspectral imaging and optical trapping: Complementary tools for assessing direction-dependent polarized emission from single upconverting $LiYF_4$:Yb^{3+}/Er^{3+} microparticles. *Advanced Optical Materials*, v. 9, n. 12, p. 2100101, 2021.

80 YANG, D. et al. Anisotropic excitation polarization response from a single white light-emitting β-$NaYF_4$:Yb^{3+},Pr^{3+} microcrystal. *Small*, v. 15, n. 43, p. 1904298, 2019.

81 PESSOA, A. R. et al. 2D thermal maps using hyperspectral scanning of single upconverting microcrystals: Experimental artifacts and image processing. DOI: 10.1021/acsami.2c08709. 2022.

82 DURKAN, C.; SHVETS, I. V. Study of shear force as a distance regulation mechanism for scanning near-field optical microscopy. *Journal of Applied Physics*, v. 79, n. 3, p. 1219–1223, 1996.

83 ASTRÖM, K. J.; HÄGGLUNG, T. *PID Controllers: Theroy, Design, and Tuning*. 2. ed. New York: Instrument Society of America, 1995. ISBN 1-55617-516-7.

84 TIPSNANO, C. *TGZ2 - AFM calibration grating*. Accessed in 13 July 2022. Available at: <https://tipsnano.com/catalog/calibration/tgz2/>.

85 KELLER, D. Reconstruction of stm and afm images distorted by finite-size tips. *Surface Science*, v. 253, n. 1, p. 353–364, 1991.

86 UDPA, L. et al. Deconvolution of atomic force microscopy data for cellular and molecular imaging. *IEEE Signal Processing Magazine*, v. 23, n. 3, p. 73–83, 2006.

87 TANIRAH, O. *Fabrication of nanostructures on tips: a proposed design for SNOM/TERS probes*. (PhD Thesis) — Eberhard Karls Universität Tübingen, Tübingen, Germany, 2020.

88 LAMBELET, P. et al. Chemically etched fiber tips for near-field optical microscopy: a process for smoother tips. *Applied Optics*, Optica Publishing Group, v. 37, n. 31, p. 7289–7292, 1998.

89 KOLOMIYTSEV, A. S. et al. Fabrication of probes for scanning near-field optical microscopy using focused ion beam. *IOP Conference Series: Materials Science and Engineering*, v. 443, p. 012015, 2018.

90 CANALE, C. et al. Recognizing and avoiding artifacts in atomic force microscopy imaging. In: _____. *Atomic Force Microscopy in Biomedical Research: Methods and Protocols*. New Jersey: Humana Press, 2011. p. 31–43. ISBN 978-1-617-79105-5.

91 PAN, X. *Processing and Feature Analysis of Atomic Force Microscopy Images*. (Master's thesis) — Missouri University of Science and Technology, Rolla, Missouri, 2014.

92 SCHIETINGER, S. et al. Plasmon-enhanced upconversion in single β-$NaYF_4$:Yb^{3+}/Er^{3+} codoped nanocrystals. *Nano Letters*, v. 10, n. 1, p. 134–138, 2010.

93 NA, H. et al. Rational morphology control of β-$NaYF_4$:Yb,Er/Tm upconversion nanophosphors using a ligand, an additive, and lanthanide doping. *Nanoscale*, v. 5, p. 4242–4251, 2013.

94 YE, X. et al. Morphologically controlled synthesis of colloidal upconversion nanophosphors and their shape-directed self-assembly. *Proceedings of the National Academy of Sciences*, v. 107, n. 52, p. 22430–22435, 2010.

95 RÜHL, P. et al. Notes on thermometric artefacts by Er^{3+} luminescence band interference. *Journal of Luminescence*, v. 232, p. 18–21, 2021.

96 JOSEPH, R. E. et al. A method for correcting the excitation power density dependence of upconversion emission due to laser-induced heating. *Optical Materials*, v. 82, p. 65–70, 2018.

97 TEITELBOIM, A. et al. Energy transfer networks within upconverting nanoparticles are complex systems with collective, robust, and history-dependent dynamics. *The Journal of Physical Chemistry C*, v. 123, n. 4, p. 2678–2689, 2019.

98 LIU, H. et al. Photon upconversion kinetic nanosystems and their optical response. *Laser & Photonics Reviews*, v. 12, n. 1, p. 1700144, 2018.

99 WANG, Z.; MEIJERINK, A. Concentration quenching in upconversion nanocrystals. *The Journal of Physical Chemistry C*, v. 122, n. 45, p. 26298–26306, 2018.

100 ZHAO, J. et al. Upconversion luminescence with tunable lifetime in $NaYF_4$:Yb,Er nanocrystals: role of nanocrystal size. *Nanoscale*, v. 5, p. 944–952, 2013.

101 CHEN, X. et al. Size-dependent downconversion near-infrared emission of $NaYF_4$:Yb^{3+},Er^{3+} nanoparticles. *Journal of Materials Chemistry C*, v. 5, p. 2451–2458, 2017.

102 ZHANG, X. et al. Effect of excitation mode on the upconversion luminescence of β-$NaYF_4$:Yb/Er nanocrystals. *Chemical Physics Letters*, v. 779, p. 138880, 2021.

103 SUN, L. et al. Concentration-regulated photon upconversion and quenching in $NaYF_4$:Yb^{3+},Er^{3+} nanocrystals: nonexponentiality revisited. *Nanoscale*, v. 11, p. 18150–18158, 2019.

104 HOSSAN, M. Y. et al. Explaining the nanoscale effect in the upconversion dynamics of β-$NaYF_4$:Yb^{3+},Er^{3+} core and core–shell nanocrystals. *The Journal of Physical Chemistry C*, v. 121, n. 30, p. 16592–16606, 2017.

105 FU, L. et al. Determination of radiative and multiphonon non-radiative relaxation rates of upconversion materials. *Physical Chemistry Chemical Physics*, v. 24, p. 9953–9963, 2022.

106 SÜLI, E.; MAYERS, D. F. *An Introduction to Numerical Analysis*. Cambridge: Cambridge University Press, 2003. ISBN 987-0-511-07810-1.

107 ZHU, H. et al. A modified energy transfer model for determination of upconversion emission of β-$NaYF_4$:Yb,Er: Role of self-quenching effect. *Journal of Luminescence*, v. 185, p. 292–297, 2017.

108 TU, L.; ZUO, J.; ZHANG, H. Revisit of energy transfer upconversion luminescence dynamics—the role of energy migration. *Science China Technological Sciences*, v. 61, p. 1301–1308, 2018.

109 van SWIETEN, T. P. et al. Mapping elevated temperatures with a micrometer resolution using the luminescence of chemically stable upconversion nanoparticles. *ACS Applied Nano Materials*, v. 4, p. 4208–4215, 2021. ISSN 25740970.

110 HUI, R. Chapter 4 - photodetectors. In: HUI, R. (Ed.). *Introduction to Fiber-Optic Communications*. London: Academic Press, 2020. p. 125–154. ISBN 978-0-128-05345-4.

111 MARTÍNEZ, E. D. et al. Hyperspectral imaging thermometry assisted by upconverting nanoparticles: Experimental artifacts and accuracy. *Physica B: Condensed Matter*, v. 629, p. 413639, 2022.

112 PANOV, N.; MARIN, R.; HEMMER, E. Microwave-assisted solvothermal synthesis of upconverting and downshifting rare-earth-doped $LiYF_4$ microparticles. *Inorganic Chemistry*, v. 57, n. 23, p. 14920–14929, 2018.

APPENDIX A – SOURCE CODE: POPULATION DYNAMICS SIMULATION FOR THERMOMETRY WITH LANTHANOID SYSTEMS

Listing A.1 – Runge-Kutta 4th order algorithm to solve a system of nonlinear rate equations simulating the dynamics in Yb^{3+}/Er^{3+} systems

```
## Physics Department - Federal University of Pernambuco, Brazil
## Nano-Optics Laboratory

## Rate Equations Model for Rare-earth-based thermometry
## Solving the decay dynamics for thermally coupled levels by Runge-Kutta 4th
    order algorithm

## By Allison Pessoa, June 2021

# Importing the nacessary libraries
import numpy as np
np.seterr('warn')

Kb = 0.695034 #cm^-1 / K  #Boltzmann's Constant
hc = 1.98644568e-25 # J.m  #Planck's Constant

#Parameters and functions related with the numerical method
class Simulation():
    def __init__(self, system, n_steps, n_eqs, h):
        self.n_steps = n_steps #number of steps
        self.n_eqs = n_eqs #number of equations
        self.n_rep = self.n_steps - 1
        self.h = h #step size (time) - The dimension depends on the model
        self.system = system #class containing the system's proprieties

    #System of rate equations
    def _F(self, t, T, I, n, n_0, i):
        n_ = np.copy(n)
        for j in range(self.n_eqs):
            n_[j][i] = n[j][i] + n_0[j]
        f = np.zeros(self.n_eqs)

        f[0] = - I*(n_[0][i])  + self.system.gamma_e*n_[1][i] + self.system.k_ET1
            *n_[1][i]*n_[2][i] + self.system.k_ET2*n_[1][i]*n_[3][i] #n_g
        f[1] = - f[0] #n_e
        f[3] = self.system.k_ET1*n_[1][i]*n_[2][i] - self.system.k_ET2*n_[1][i]*
            n_[3][i] - self.system.gamma_1*n_[3][i] #n_1
        f[5] = self.system.k_ET2*n_[1][i]*n_[3][i] - self.system.gamma_b*n_[5][i]
             + self.system.W_NR_ab(T)*n_[4][i] - self.system.W_NR_ba(T)*n_[5][i]
            #n_2b
```

```
        f[4] = self.system.W_NR_ba(T)*n_[5][i] - self.system.W_NR_ab(T)*n_[4][i]
            - self.system.W_NR_ac(T)*n_[4][i] - self.system.gamma_a*n_[4][i]#n_2a
        f[6] = self.system.W_NR_ac(T)*n_[4][i] - self.system.gamma_c*n_[6][i] #
            n_2c
        f[2] = - (f[3] + f[4] + f[5] + f[6]) #n_0

        return f

    def _update_n(self, n,k1,k2,k3,k4,i):
        for j in range(self.n_eqs):
            n[j][i+1] = n[j][i] + (k1[j] + 2*k2[j] + 2*k3[j] + k4[j])/6

    def _calculate(self, n, t, T, I):
        #population matrix; time array; temperature; intensity
        for i in range(self.n_rep):
            k1= self._F(t[i]           , T , I , n , np.zeros(self.n_eqs) , i)*
                self.h
            k2= self._F(t[i]+self.h/2  , T , I , n ,       k1/2           , i)*
                self.h
            k3= self._F(t[i]+self.h/2  , T , I , n ,       k2/2           , i)*
                self.h
            k4= self._F(t[i]+self.h    , T , I , n ,        k3            , i)*
                self.h

            self._update_n(n,k1,k2,k3,k4,i)
            t[i+1] = t[i] + self.h

        return t,n

    def run(self, init_cond, temperature, intensity):
        n = np.zeros((self.n_eqs,self.n_steps))
        t = np.zeros(self.n_steps)
        #Initial Conditions
        for i in range(len(n)):
            n[i][0] = init_cond[i]

        return self._calculate(n, t, temperature, intensity)

class System():
    def __init__(self):
        #Levels Degeneracy
        self.g_b = 2*(11/2) + 1
        self.g_a = 2*(3/2) + 1
        self.g_c = 2*(9/2) + 1
        #Energy Level's difference
        self.DeltaE_ab = 692 #[cm-1] Goncalves et al. [15]
        self.DeltaE_ac = 3214 #[cm-1] Goncalves et al. [15]
```

```
77          #Effective Phonon Energy
            self.hw = 230.67 #[cm-1] Estimated from Renero-Lecuna et al. [94]
79          #Transition Rates
            self.gamma_b = 0.002399 #[us-1] Yao et al. [55]
81          self.gamma_a = 0.000937  #[us-1] Yao et al. [55]
            self.gamma_c = 0.000531 #[us-1] Yao et al. [55]
83          self.gamma_1 = 0.000108 #[us-1] Yao et al. [55]
            self.gamma_e = 0.000625 #[us-1] Hossan et al. [104]
85
            self.k_ET1 = 0.002695 #[us-1] modified from Hossan et al. [104]
87          self.k_ET2 = 0.0061495 #[us-1] modified from Hossan et al. [104]

89          self.alpha = 3.74e-3 #[cm] - Energy-gap Law
            self.beta = 10 #[us-1] - Energy-gap Law
91
            #Calculations
93          self.p_ab = round(self.DeltaE_ab/self.hw)
            self.p_ac = round(self.DeltaE_ac/self.hw)
95
            self.W_NR_ab_T0 = self.beta*np.exp(-self.alpha*self.DeltaE_ab)
97          self.W_NR_ac_T0 = self.beta*np.exp(-self.alpha*self.DeltaE_ac)

99      #Non-radiative transition rates - functions
        def n_eff(self, T):
101         return ((np.exp(self.hw/(Kb*T))-1)**(-1))
        def W_NR_ba(self, T): #NR Decay
103         return (self.W_NR_ab_T0*self.g_a*(1 + self.n_eff(T))**(self.p_ab))
        def W_NR_ab(self, T): #NR Absorption
105         return (self.W_NR_ab_T0*self.g_b*(self.n_eff(T))**(self.p_ab))
        def W_NR_ac(self, T): #NR Decay
107         return (self.W_NR_ac_T0*self.g_c*(1 + self.n_eff(T))**(self.p_ac))

109 # SIMULATION
    YbEr = System()
111 Sim = Simulation(YbEr,30000,7,0.05)
    #1st round
113 t, n = Sim.run([1,0,1,0,0,0,0],297,1e-10) #Initial populations, temperature,
        excitaion rate
    #2nd round
115 t, n = Sim.run([ n[0][-1],n[1][-1],n[2][-1],n[3][-1],n[4][-1],n[5][-1],n[6][-1]
    ],297,0)
```

Source: The author (2022)